Imaging from Fourier Spectral Data:

Problems in Discontinuity Detection, Non-harmonic Fourier Reconstruction and Point-spread Function Estimation

by

Adityavikram Viswanathan

A Dissertation Presented in Partial Fulfillment
of the Requirements for the Degree
Doctor of Philosophy

ARIZONA STATE UNIVERSITY

August 2010

Imaging from Fourier Spectral Data:

Problems in Discontinuity Detection, Non-harmonic Fourier Reconstruction and Point-spread Function Estimation

by

Adityavikram Viswanathan

has been approved

July 2010

Graduate Supervisory Committee:

Anne Gelb, Co-Chair
Douglas Cochran, Co-Chair
Rosemary Renaut
David Frakes
Tolga Duman
Cihan Tepedelenlioglu

ACCEPTED BY THE GRADUATE COLLEGE

ABSTRACT

Certain applications such as magnetic resonance imaging (MRI) and synthetic aperture radar (SAR) imaging demand the processing of input data collected in the spectral domain. While spectral methods traditionally boast of superior accuracy and efficiency, the presence of jump discontinuities in the underlying function result in the familiar Gibbs phenomenon, with an immediate reduction in the accuracy of the method. This dissertation proposes methods and computational tools for the efficient and accurate processing of such data, with applications to imaging. The relationship between local features and Fourier measurements is exploited to address three specific problems – the detection of jump discontinuities from Fourier data, the reconstruction of functions from non-harmonic or non-uniform Fourier measurements, and the estimation of point-spread functions (PSFs) from blurred Fourier data.

Jump locations and values are among the most important local features of a piecewise-analytic function. Use of the *concentration edge detection method* is discussed, which uses Fourier partial sums and "filter" factors known as concentration factors to approximate this jump information. A flexible, iterative framework is proposed for the design of these factors, along with the formulation of a statistical detector to detect the presence of jumps from noisy Fourier data. Extensions of the method to multiple dimensions as well as non-harmonic Fourier measurements are also provided. Jump information from this method is shown to play an important role in obtaining accurate reconstructions of functions from non-harmonic Fourier data. This is a challenging problem, typically complicated by the acquisition of spectral samples with non-uniform sampling density. The use of *spectral re-projection* methods is proposed to reduce the error caused by non-harmonic acquisitions. These reconstructions are shown to offer great accuracy, while requiring fewer input measurements than conventional Fourier methods. Results of an indirect reconstruction method are also provided, which uses jump information to synthesize "new" high-frequency Fourier coefficients. Simulation results reveal this framework to yield highly accurate reconstructions of the underlying function. Finally, the presence of jump discontinuities in a function is exploited to construct an efficient scheme for the estimation of PSFs from blurred Fourier data. Representative results are provided, demonstrating the accurate estimation of Gaussian and out-of-focus PSFs from blurred and noisy Fourier coefficients.

TABLE OF CONTENTS

Chapter Page

LIST OF FIGURES

Figure Page

LIST OF TABLES

CHAPTER 1

INTRODUCTION

Spectral methods, and Fourier spectral methods in particular, enjoy widespread popularity in several areas of science and engineering. Besides constituting natural basis functions for modeling diverse natural phenomena, they also possess attractive numerical properties. For example, it is well known, [1], that the partial Fourier sum converges exponentially quickly to the underlying function, if the function is smooth and periodic. Unfortunately, the approximation of piecewise-analytic functions using spectral methods suffers from the Gibbs phenomenon, [1]. This manifests as non-physical oscillations at a local level and a reduced order of convergence at a global level. It is this piecewise-analyticity which presents a problem when processing input data from the spectral domain. This is the case in certain imaging modalities such as magnetic resonance imaging (MRI) and synthetic aperture radar (SAR) imaging. In these applications, the nature of the measurement process is such that the input measurements correspond to the Fourier coefficients of the specimen being imaged. The processing of such data therefore requires special attention.

This dissertation provides theoretical and computational tools that address three specific problems encountered when imaging from Fourier spectral data:

1. The identification of jump or edge information from Fourier measurements.
2. The reconstruction of piecewise-analytic functions from non-harmonic or non-uniform Fourier measurements.
3. The estimation of point-spread functions (psfs) in de-blurring problems from Fourier data.

A recurring theme in the ensuing chapters is the often intricate interplay between local features and global expansions. We restrict our attention in this dissertation to jump information and Fourier spectral data. By exploiting this relationship, we are able to devise algorithms for the accurate and efficient identification of jump locations and values from a few, and possibly noisy Fourier coefficients. Extensions to the case of missing and non-harmonic Fourier measurements are also provided. Moreover, we use this edge information as an integral component of reconstruction schemes for non-harmonic Fourier data. Non-harmonic Fourier reconstruction is a challenging problem, compounded by the acquisition of measurements with non-uniform sample density, and by the presence of discontinuities in the function. The availability of jump information, however, allows for the mitigation of effects caused by non-harmonic acquisition and accurate, cost-efficient

function reconstructions. The application of jump detection on blurred Fourier data also allows for the estimation of blurs using a simple and non-iterative framework.

An outline of the rest of the dissertation is as follows: The detection of jump discontinuities and their values is addressed in Chapter 2. The framework used for this is the concentration edge detection method, [2], which computes an approximation to the singular support of a function from its first few Fourier series coefficients. This framework uses a Fourier partial sum and "filter" factors known as concentration factors. Since the quality of the approximation is characterized by these factors, we present a flexible and iterative framework for the design of concentration factors. Sample problem formulations are provided and some of the traditional concentration factors are shown to be solutions to particular formulations. The design of factors for missing spectral data is also addressed.

The concentration method computes a Fourier partial sum to approximate the singular support of the function. Since we start with global measurements, obtaining a localized, accurate and well resolved approximation to jumps is challenging. Consequently, we discuss the design of an edge detector that uses a few evaluations of the concentration sum in a small neighborhood of the decision point to ascertain the presence or absence of a jump. This design is an extension and generalization of the method described in [3]. Finally, extensions of the concentration method to multiple dimensions and non-harmonic Fourier data are presented.

We remark that performance evaluation of these methods is a complicated task, since most existing edge detection schemes are constructed for physical space data. Base-lining against these methods (e.g., divided differences, the Sobel, Prewitt or Canny edge detectors) is to a certain extent unfair, since they were not designed to handle jump or edge detection from spectral data. Comparisons to results starting from physical, grid point data is also not fair, as this fails to address the implications of starting with global data. Consequently, comparisons to other post-processing methods developed specifically in conjunction with the concentration method are made, and our framework is show to perform well even in the presence of noise. Comparisons to some of the standard edge detectors such as the Canny edge detector are provided where appropriate, both as an illustrative reference and as an indication of the loss in accuracy resulting from the use of spectral data.

Representative results of these methods are shown in Figures 1.1 and 1.2, while a detailed discussion is deferred to Chapter 2. Figure 1.1 illustrates the concentration edge detection method in action. Figure 1.1 (a) plots the acquired measurements in this simulation, which are the first few (129) Fourier coefficients of an underlying test function, with two bands of missing data to simulate instrumentation errors. Figure 1.1 (b) plots the results of jump detection. These results use the concentration factor design framework to compute a custom factor for this missing data problem. The concentration jump approximation of the function is plotted as a solid line in Figure 1.1 (b), while the precise jump locations and values obtained after applying the edge detector are plotted as ○'s. The capabilities of the statistical edge detector are more ably illustrated by Figure 1.2 (a), which plots the accurate detection of jumps in a test function with significant noise. Finally, Figure 1.2 (b) illustrates the application of this method to images, with a plot of the edge map of the Shepp-Logan brain phantom, [4].

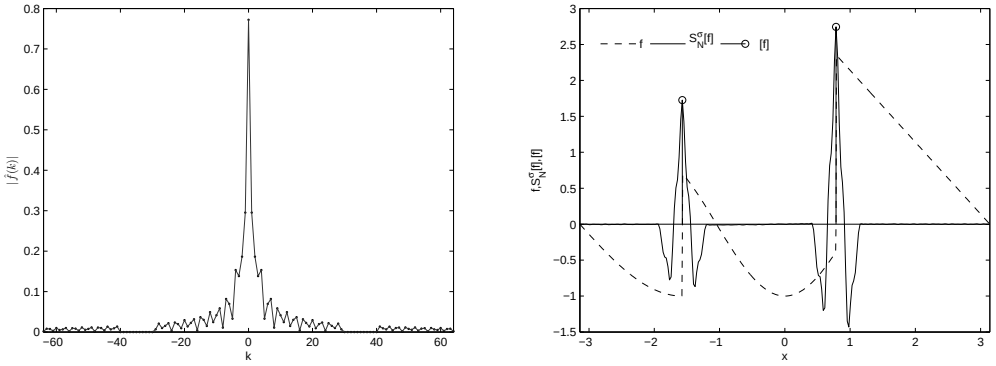

(a) Acquired measurements (with missing bands)

(b) Concentration jump detection

Fig. 1.1: Accurate identification of jump locations and values (from 129 Fourier coefficients)

Reconstruction of functions from non-harmonic Fourier measurements is discussed in Chapter 3. Non-harmonic acquisitions present an immediate problem because families of non-harmonic exponentials rarely constitute a basis for functions of practical interest. Insight into this phenomenon may also be attained by comparing the kernel described by the non-harmonic modes to the standard Dirichlet kernel. It is explained in Chapter 3 that the non-harmonic acquisition manifests as non-decaying oscillatory sidelobes in the kernel, while non-uniform sampling density manifests as

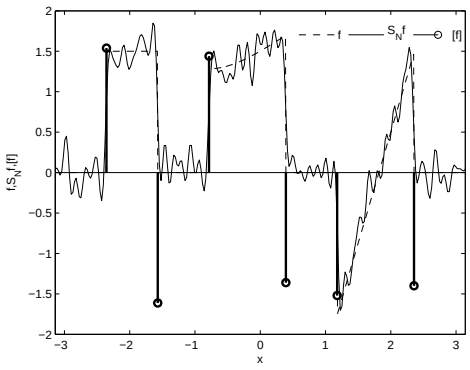

(a) Jump detection in noise

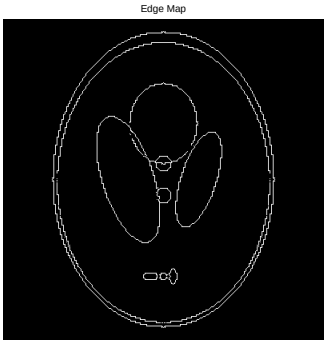

(b) Edge map of the 2D Shepp-Logan brain phantom

Fig. 1.2: Extensions of the concentration edge detection method

a loss of localization. Existing reconstruction procedures for non-harmonic data work by mapping the non-uniform measurements to equispaced modes, followed by standard Fourier reconstruction. Two such methods, convolutional gridding, [5], and uniform re-sampling, [6], are discussed, along with error analysis for gridding reconstructions. This analysis reveals that the primary impediment to accurate reconstruction is the non-uniform sampling density. Since it is customary to in many applications to undersample the high modes (which typically account for only a small fraction of the signal energy), this manifests as poor accuracy of the high mode Fourier coefficients.

This situation is similar to the familiar Gibbs phenomenon, where a slow decay of the Fourier coefficients leads to poor accuracy in partial Fourier sum reconstructions. Spectral re-projection schemes, [7], have been previously proposed and successfully applied to the resolution of the Gibbs phenomenon in spectral methods. We propose the use of re-projection methods to mitigate the effects of non-harmonic acquisition and non-uniform sampling density. Analysis of the reconstruction error for spectral re-projection shows that equivalent or better accuracy may be attained when compared to standard Fourier methods, while requiring the use of far fewer input measurements. The use of re-projection methods also allows for the elimination of Gibbs artifacts, which may be important in applications such as MR imaging. Illustrative results from such reconstructions are shown in Figure 1.3. Figure 1.3 (a) plots example non-harmonic sampling distributions, while Figure 1.3 (b) confirms that standard Fourier partial sums yield poor results for such data. Figure 1.3

(c) shows the result of the gridding method, post-processed by a low pass filter, while Figure 1.3 (d) plots the spectral re-projection reconstruction using Gegenbauer polynomials.

Re-projection methods work by using the location of jump discontinuities to reconstruct the function in smooth intervals, and subsequently piecing these intervals together. We also present preliminary results of a method where we employ not just the jump locations, but also the jump values to produce highly accurate reconstructions. This method directly exploits the relationship between local jump features and Fourier coefficients to estimate the values of the high frequency Fourier modes. This allows us to obtain far greater resolution than that supported by the acquired measurements.

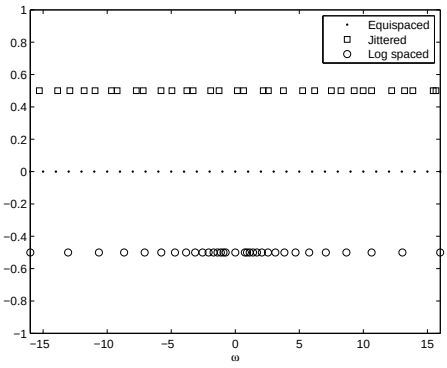

(a) Non-harmonic sampling modes

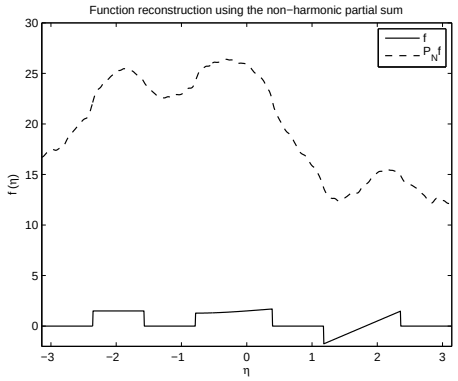

(b) Naive partial sum reconstruction from log spaced spectral samples

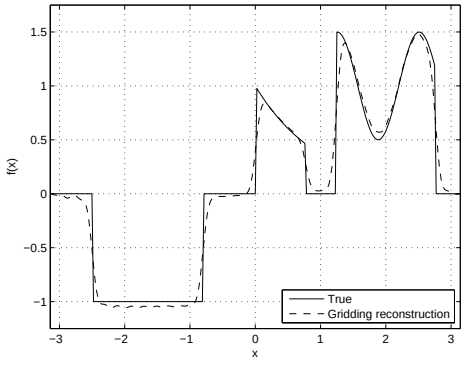

(c) Example gridding reconstruction, 256 coefficients

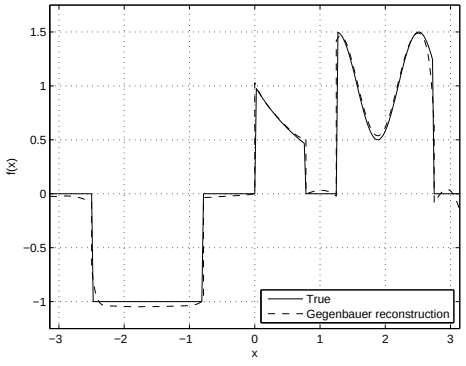

(d) Representative re-projection reconstruction, 85 coefficients

Fig. 1.3: Non-harmonic Fourier reconstruction

Chapter 4 summarizes the estimation of psfs in de-blurring problems from the blurred, and pos-

sibly noisy Fourier coefficients of piecewise-analytic functions. Blurring problems abound in the real world, where measurements are often corrupted by the transmission channel and instrumentation effects. A natural task under these circumstances is the recovery of the original function. An accurate estimate of the blur significantly aids in the successful inversion of blurring effects. To obtain such an estimate, we apply the concentration method on the blurred Fourier coefficients of the function. The resulting jump approximation yields shifted and scaled replicates of the psf, from which blur parameters may be obtained. This procedure is illustrated in Figure 1.4, where the estimation of Gaussian and motion blurs is plotted. The underlying function, in either case, is plotted using a dotted line, while the true blur is plotted for reference using a dashed line. The result of applying the concentration edge detection method to the blurred Fourier data is plotted using a solid line, and can be seen to manifest as replicates of the blur at each of the jump locations.

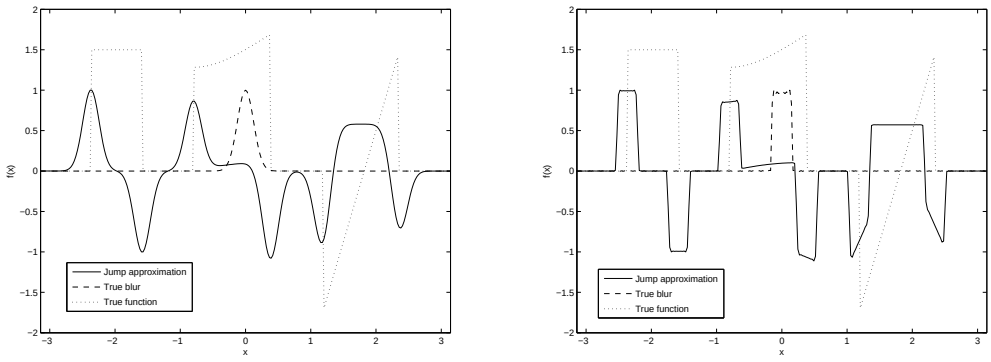

(a) Estimation of Gaussian blurs (b) Estimation of motion blurs

Fig. 1.4: Estimating psfs by applying the concentration method

Finally, Chapter 5 summarizes the findings of this dissertation and describes some avenues for future investigation.

CHAPTER 2

EDGE DETECTION FROM FOURIER DATA

The detection of jumps in piecewise-analytic functions is a common signal processing operation, which finds application in several branches of science and engineering. For example, edge detection is an important image processing operation. Besides being standalone entities of interest, edges often serve an important role in other tasks such as segmentation and pattern recognition. High-resolution reconstruction schemes, and the solution of partial differential equations (PDEs) are two other areas where edge detection finds importance. In general, piecewise-analyticity reduces the reconstruction accuracy, or the accuracy of the solution of PDEs involving such functions. The availability of edge information, however, can lead to significant improvements in the quality of the resulting solutions. The interested reader is referred to [8, Chapter 9] for a discussion of one such reconstruction scheme and its application in the solution of PDEs.

Certain applications demand the identification of edges from Fourier measurements. This is the case, for example, in magnetic resonance imaging (MRI) and synthetic aperture radar (SAR). In these applications, the underlying physical phenomenon entails the collection of data in the Fourier domain. The identification of edges from such data is particularly challenging, since it requires the accurate identification of a local feature from a global representation. Figure 2.1 illustrates this problem. In this figure, we plot the edge map of the Shepp-Logan brain phantom, [4]. Figure 2.1 (a) plots a 257 grid point phantom, while Figure 2.1 (b) plots the edge map of this phantom as obtained using Matlab's implementation of the Canny edge detector, [9]. Figure 2.1 (c) plots the Fourier reconstruction of the phantom on 257 grid points from its first 101 ($N = 50$) Fourier coefficients. Note the presence of Gibbs oscillations in the reconstruction. These non-physical oscillations, which are a consequence of starting from global data, make edge detection challenging. The resulting edge map, as generated by the Canny edge detector, is shown in Figure 2.1 (d) and can be seen to contain numerous false activations.

In this chapter, we present methods and algorithms to accurately estimate jump locations and values in piecewise-analytic functions from their first few Fourier series coefficients. We utilize the *concentration edge detection* method as the underlying framework for this purpose. This method computes an approximation to the *jump function* (to be defined in Section 2.1) using a Fourier partial sum and Fourier space "filter" factors known as *concentration factors*. The characteristic features

(a) The Shepp-Logan phantom

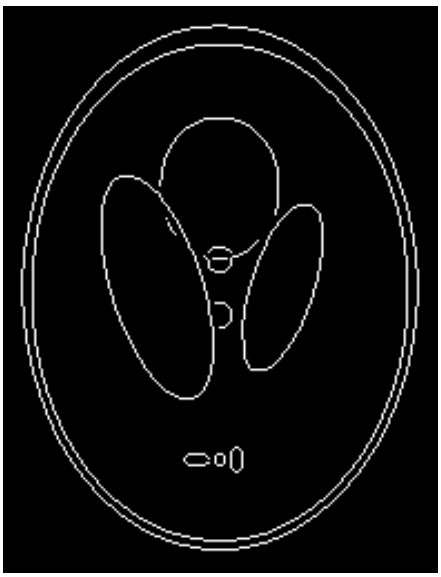

(b) Canny edge map

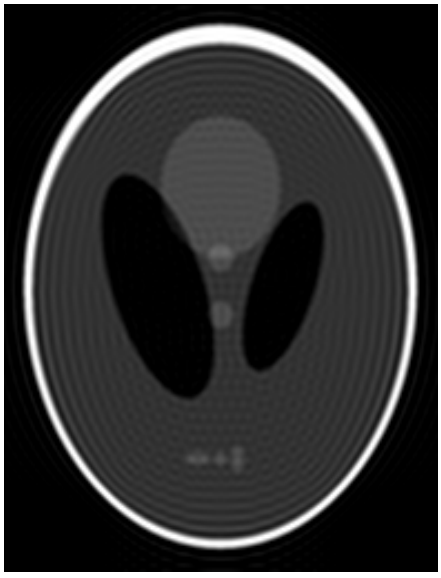

(c) Fourier reconstruction of the phantom, $N = 50$

(d) Canny edge map of the Fourier reconstruction

Fig. 2.1: Edge detection from Fourier data

of the resulting approximation depend on the design of these concentration factors. We therefore propose a flexible, iterative framework for the design of these factors, supporting a wide class of design criteria, including cases such as the design of factors for missing or banded spectral data. Several sample problem formulations are provided to illustrate the capabilities of the method. A recurring theme in the development of this material is the notion of a *jump response*. Although this will be more formally defined in Section 2.1.1, the jump response is essentially the concentration jump approximation of a unit amplitude jump. The jump response describes the unique oscillatory form of the jump function approximation both near and away from jumps. This becomes particularly important in the design of an effective edge detector, which takes the continuous jump function approximation and returns the discrete jump locations and values in the function. A statistical formulation is pursued and a variant of the generalized matched filter detector is designed. Several examples illustrating the performance of the detector are provided, along with comparisons to other standard methods of edge detection. A simple extension of this method to two dimensions is also described with examples. Finally, and as a special case, we are interested in the detection of jumps given non-harmonic Fourier data, i.e., Fourier coefficients sampled on non-uniform modes. A straightforward extension of the concentration edge detection method using non-harmonic exponentials is shown to fail in this case, with an iterative solution proposed to accurately identify jump values and locations.

The rest of this chapter is organized as follows: Section 2.1 contains a summary of the concentration edge detection method. The notion of concentration factors and admissibility conditions for the same are introduced, besides tabulation of some prototypical families of such factors. Example responses on test functions are also provided. The jump response is defined, and the distinction between low and high-order edge detectors explained. Section 2.2 briefly reviews previous and related work on this topic, while Section 2.3 provides an alternative formulation of the concentration method. Here, we relate local edge information to global Fourier measurements, in addition to expressing the concentration jump approximation in terms of the jump function and the jump response. This formulation provides a suitable framework for the discussion concentration factor design, with Section 2.4 providing the design framework and several illustrative sample problem formulations. The design of an edge detector using a detection theoretic formulation is pursued in

Section 2.5. This section includes expressions for the covariance structure of the noise component, besides the design of the detector as well as expressions for its performance. Several examples and comparisons to standard techniques are given. An extension of the concentration method to two-dimensional functions is provided in Section 2.6. Finally, we discuss the application of the concentration edge detection method to identifying jump information from non-harmonic Fourier data in Section 2.7.

2.1 The Concentration Edge Detection Method

Let f be a real-valued[1], 2π-periodic, piecewise-smooth function in $[-\pi, \pi)$. Given the first $2N+1$ Fourier series coefficients

$$\hat{f}(k) = \frac{1}{2\pi} \int_{-\pi}^{\pi} f(x) e^{-ikx} dx, \quad k = -N, ..., N \tag{2.1}$$

we are interested in identifying the locations and values of jump discontinuities in f. We start our discussion by defining the jump function.

Definition 1. *(Jump Function) Let $f : \mathbb{R} \to \mathbb{R}$, with $f(x^+)$ and $f(x^-)$ denoting the well-defined right and left-hand limits of f for every $x \in \mathbb{R}$. The jump function associated with f and denoted by $[f]$ is defined as the difference between the right and left hand limits of the function; i.e.,*

$$[f](x) := f(x^+) - f(x^-) \tag{2.2}$$

Note that the jump function is non-zero only at a jump discontinuity, where it takes the value of the jump.

The concentration edge detection method, [2, 10], computes an approximation to the jump function using a partial sum of the form

$$S_N^\sigma[f](x) = i \sum_{|k| \le N} \hat{f}(k) \text{sgn}(k) \sigma\left(\frac{|k|}{N}\right) e^{ikx} \tag{2.3}$$

[1]We restrict our attention to real-valued functions, since real-world applications typically require the estimation of real-valued jumps.

The choice of the factor $\sigma(\eta) = \sigma\left(\frac{|k|}{N}\right)$, known as the *concentration factor*, decides the convergence properties of the jump approximation. These factors are known to satisfy the following admissibility conditions[2]:

1. $\sum_{k=1}^{N} \sigma\left(\frac{k}{N}\right)\sin(kx)$ be odd
2. $\frac{\sigma(\eta)}{\eta} \in C^2(0,1)$
3. $\int_{\epsilon}^{1} \frac{\sigma(\eta)}{\eta} \to -\pi$, $\epsilon = \epsilon(N) > 0$ being small

We note that the concentration sum in (2.3) can be interpreted as the convolution of f with a *concentration kernel* C_N^σ defined as

$$C_N^\sigma(x) := i \sum_{|k|\le N} \text{sgn}(k)\sigma\left(\frac{|k|}{N}\right) e^{ikx} \tag{2.4}$$

Therefore (2.3) is equivalent to

$$S_N^\sigma[f](x) = (f * C_N^\sigma)(x) \tag{2.5}$$

The admissibility conditions essentially state that the concentration kernel is required to be odd, suitably normalized and satisfy a certain smoothness constraint in order to approximate the jump function. Table 2.1 lists a selection of concentration factors introduced in [2, 10], while Figure 2.2 plots these factors in the Fourier domain.

Table 2.1: Examples of concentration factors

Factor	**Expression**	**Remarks**
Trigonometric	$\sigma_G(\eta) = \frac{\pi \sin(\pi\eta)}{\text{Si}(\pi)}$	$\text{Si}(\pi) = \int_0^\pi \frac{\sin(x)}{x}\,dx$
Polynomial	$\sigma_P^p(\eta) = p\pi\eta^p$	p is the order of the factor
Exponential	$\sigma_E(\eta) = C \cdot \eta \cdot \exp\left(\frac{1}{\alpha\eta(\eta-1)}\right)$	α is the order C is a normalizing constant $C = \frac{\pi}{\int_{\frac{1}{N}}^{1-\frac{1}{N}} \exp\left(\frac{1}{\alpha\tau(\tau-1)}\right) d\tau}$

[2] A detailed development and discussion of these conditions can be found in [10].

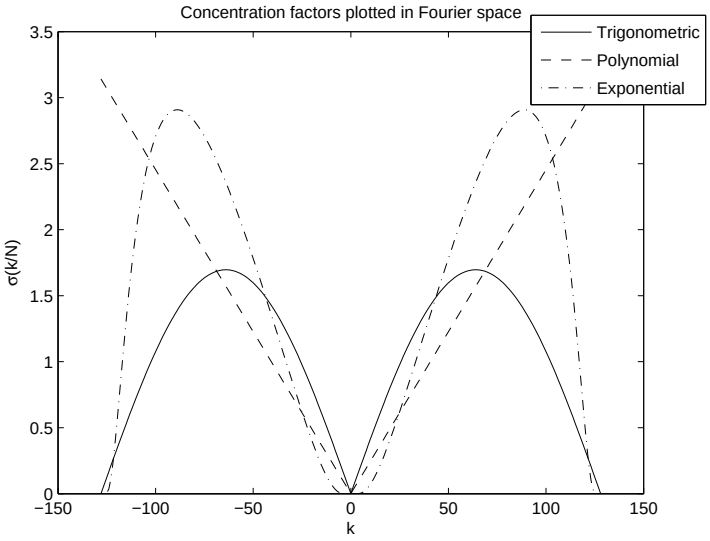

Fig. 2.2: Concentration factors plotted in Fourier space

If $\sigma(\cdot)$ is an admissible concentration factor, $S_N^\sigma[f]$ "concentrates" at the singular support of f and the jump approximation obeys the concentration property, [11, Theorem 2.3],

$$S_N^\sigma[f](x) = [f](x) + \begin{cases} \mathcal{O}\left(\frac{\log N}{N}\right) & d(x) \lesssim \frac{\log N}{N} \\ \mathcal{O}\left(\frac{\log N}{(Nd(x))^s}\right) & d(x) \gg \frac{1}{N} \end{cases} \tag{2.6}$$

Here, $d(x)$ denotes the distance between a point in the domain and the nearest discontinuity, while $s > 0$ is a parameter which depends on the concentration factor chosen. The value of s depends on the order[3] of the concentration factor, with a higher-order edge detector associated with a larger value of s as compared to a lower-order edge detector.

2.1.1 The Jump Response

As indicated in the previous discussion, the characteristic features of the concentration jump approximation depend on the choice of the concentration factor. Associated with each concentration factor is a unique oscillatory pattern in the immediate vicinity and away from jumps. We will refer to this as the *jump response* associated with a concentration factor. Let $\sigma(\eta)$ be an admissible concentration factor. Let $r(x)$ denote the unit ramp function, with a corresponding jump function

[3]The notion of low and high order edge detectors and their characteristic features will be discussed with illustrative examples below.

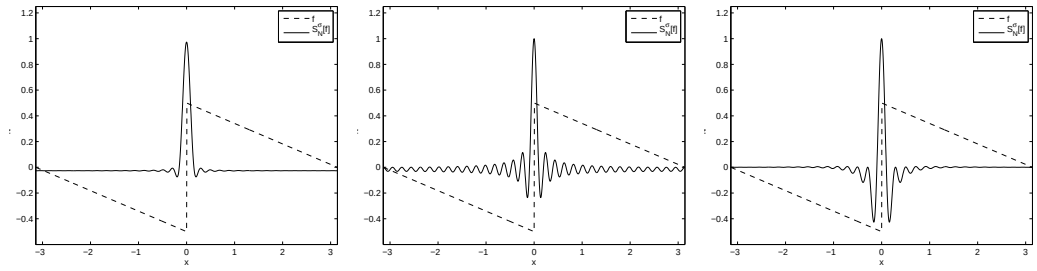

(a) Trigonometric (b) Polynomial (c) Exponential

Fig. 2.3: Jump responses of different concentration factors ($N = 32$)

$[r](x)$.

$$r(x) = \begin{cases} \frac{-x-\pi}{2\pi} & x < 0 \\ \frac{\pi-x}{2\pi} & x > 0 \end{cases}, \qquad [r](x) = \begin{cases} 1 & x = 0 \\ 0 & \text{else} \end{cases}$$

Definition 2. *(Jump Response) The jump response, denoted by $W_0^{\sigma,N}(x)$, is defined as the jump function approximation of the unit ramp as generated by the concentration sum (2.3). i.e.,*

$$\begin{aligned} W_0^{\sigma,N}(x) := S_N^\sigma[r](x) &= i \sum_{|k|\le N} \hat{r}(k)\, \mathit{sgn}(k)\, \sigma\left(\frac{|k|}{N}\right) e^{ikx} \\ &= \frac{1}{2\pi} \sum_{0<|k|\le N} \frac{\sigma\left(\frac{|k|}{N}\right)}{|k|} e^{ikx} \end{aligned} \tag{2.7}$$

The final equation is obtained by substituting the Fourier coefficients of the ramp function,

$$\hat{r}(k) = \begin{cases} \frac{1}{2\pi i k} & k \neq 0 \\ 0 & k = 0 \end{cases}$$

The jump responses of each of the concentration factors listed in Table 2.1 are plotted in Figure 2.3. The reader is encouraged to study these plots in association with (2.6). In particular, note the "concentration" of the jump approximation at the singular support of r. Further, note the non-uniform convergence to the true jump function; this is to be expected as we are computing a Fourier partial sum approximation of the piecewise-defined jump function. The different orders of convergence away from the jump for each of the concentration factors, parameterized by s in (2.6), is also evident from the plots. For example, the polynomial concentration factor shows slowly decaying

oscillations for $|x| > 0$, while the exponential factor shows a vanishing response away from the jump.

2.1.2 Sample Jump Function Approximations and Low/High-order Edge Detectors

To study the performance of the concentration edge detection method, we introduce the test functions $f_1(x)$ and $f_2(x)$, with associated jump functions given in (2.9) and (2.11) respectively.

$$f_1(x) = \begin{cases} \frac{3}{2} & -\frac{3\pi}{4} \le x < -\frac{\pi}{2} \\ \frac{7}{4} - \frac{x}{2} + \sin(x - \frac{1}{4}) & -\frac{\pi}{4} \le x < \frac{\pi}{8} \\ \frac{11}{4}x - 5 & \frac{3\pi}{8} \le x < -\frac{3\pi}{4} \\ 0 & \text{else} \end{cases} \tag{2.8}$$

$$[f_1](x) = \begin{cases} \frac{3}{2} & x = -\frac{3\pi}{4} \\ -\frac{3}{2} & x = -\frac{\pi}{2} \\ \frac{14+\pi}{8} - \sin\left(\frac{\pi+1}{4}\right) \approx 1.28 & x = -\frac{\pi}{4} \\ \sin\left(\frac{2-\pi}{8}\right) - \frac{28-\pi}{16} \approx -1.70 & x = \frac{\pi}{8} \\ \frac{33\pi}{32} - 5 \approx -1.76 & x = \frac{3\pi}{8} \\ 5 - \frac{33\pi}{16} \approx -1.48 & x = \frac{3\pi}{4} \\ 0 & \text{elsewhere} \end{cases} \tag{2.9}$$

$$f_2(x) = \begin{cases} \sin(6x) & -\frac{5\pi}{6} \le x < 0 \\ \frac{1}{\pi}e^{-2x}(\pi - x) & x \ge 0 \end{cases} \tag{2.10}$$

$$[f_2](x) = \begin{cases} 1 & x = 0 \\ 0 & \text{else} \end{cases} \tag{2.11}$$

The concentration jump function approximation of the two test functions are provided in Figures 2.4 (a) and (b) respectively. The jump function approximation of $f_1(x)$ was generated using the trigonometric factor while the trigonometric and exponential jump function approximations of $f_2(x)$ are plotted. We draw attention to the jump function approximation of $f_2(x)$ in Figure 2.4 (b). The trigonometric jump function approximation has a large non-zero value in the smooth interval $(-\pi, 0)$. This is characteristic of a *low-order* edge detector acting on a function with large

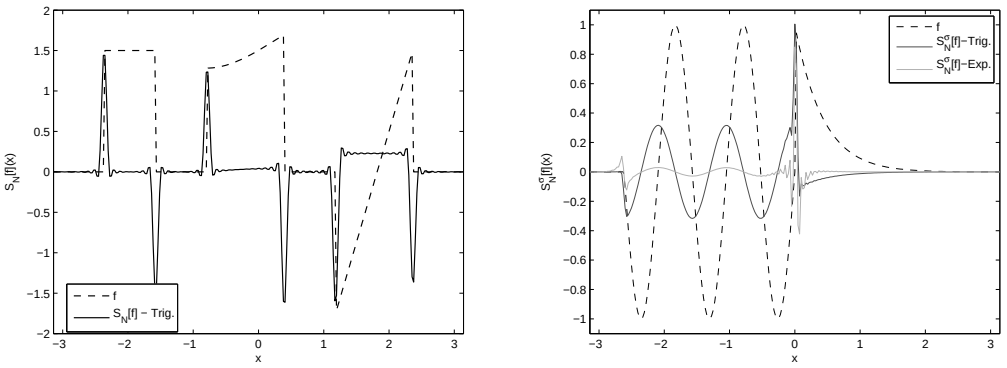

(a) Jump approximation of $f_1(x), N = 64$ (b) Jump approximation of $f_2(x), N = 100$

Fig. 2.4: Jump approximations of two test functions

variation. In contrast, the exponential (*high-order*) jump function approximation contains a vanishing response in smooth regions[4] at the expense of some additional oscillatory behavior in the immediate neighborhood of the jump.

2.2 Summary of Previous Work

The concentration edge detection method was first introduced in [2] and extended in [10], with the introduction of new families of concentration factors and use of the "enhancement of scales" procedure. This post-processing procedure essentially raises the concentration jump approximation to the p^{th} power, thereby improving the resolution of jumps and separating regions (or scales) of jump from smooth regions. Further efforts to improve jump resolution and reduce spurious oscillations were undertaken in [12], where the *minmod*[5] operator was used. This approach uses jump responses from multiple concentration factors in conjunction with the minmod operator to reduce oscillations in the smooth regions and in the immediate vicinity of jumps. Reduction of oscillatory behavior was also the motivation behind the design of a class of concentration factors known as matching waveform concentration factors, [13]. These factors are equivalent to computing correlations of

[4]The small non-zero oscillatory response in the vicinity of $x = -\frac{5\pi}{6}$ is due to a discontinuity in the derivative of $f_2(x)$.

[5]$\text{minmod}\,(a_1, ..., a_n) := \begin{cases} \text{sgn}(a_1) \cdot \min\left(|a_1|, ..., |a_n|\right) & \text{sgn}(a_1) = \text{sgn}(a_2) = ... = \text{sgn}(a_n) \\ 0 & \text{else} \end{cases}$

the jump function approximation with the jump response, Definition 2. The consequence is a peak at the jump location and vastly reduced oscillations in the smooth regions. Several works have also addressed the jump detection in the presence of noise. For example, [11] uses a framework of breaking the function into scales of smoothness, noise and jumps. An approach at reducing the variance of the jump function approximation, along with subsequent reconstruction of the function, is pursued in [14]. A detection theoretic formulation of the jump detection problem, with matched filter formulations are provided in [3] and [15]. Finally, iterative formulations of this jump detection method, drawing from recent developments and algorithms for compressive sensing, [16, 17], are developed in [18]. This framework allows for the identification of jump information from sparse and possibly randomly sampled Fourier data.

2.3 Analysis of the Concentration Sum

In this section, we provide an alternative formulation of the concentration method by relating the concentration sum (2.3) to the jump function. We start by studying the relation between Fourier coefficients and jump locations and values. Consider, without loss of generality, a periodic function on $[-\pi, \pi)$ with a single jump at $x = \zeta$. For $k \neq 0$, we have

$$\hat{f}(k) = \frac{1}{2\pi} \int_{-\pi}^{\zeta^-} f(x) e^{-ikx} dx + \frac{1}{2\pi} \int_{\zeta^+}^{\pi} f(x) e^{-ikx} dx \tag{2.12}$$

On integrating by parts, we obtain

$$\hat{f}(k) = \left(f(\zeta^+) - f(\zeta^-)\right) \frac{e^{-ik\zeta}}{2\pi ik} + \frac{1}{ik} \cdot \left(\frac{1}{2\pi} \int_{-\pi}^{\zeta^-} f'(x) e^{-ikx} + \frac{1}{2\pi} \int_{\zeta^+}^{\pi} f'(x) e^{-ikx} \right) \tag{2.13}$$

where we have used the periodicity of f. From (2.2), we obtain

$$\hat{f}(k) = [f](\zeta) \frac{e^{-ik\zeta}}{2\pi ik} + \frac{1}{ik} \cdot \left(\frac{1}{2\pi} \int_{-\pi}^{\zeta^-} f'(x) e^{-ikx} + \frac{1}{2\pi} \int_{\zeta^+}^{\pi} f'(x) e^{-ikx} \right)$$

Note that the term within parenthesis is the same as (2.12) for f'. Therefore, by repeated application of integration by parts, we obtain

$$\hat{f}(k) = \frac{1}{2\pi} \left(\frac{[f](\zeta)}{ik} + \frac{[f'](\zeta)}{(ik)^2} + \frac{[f''](\zeta)}{(ik)^3} + ... \right) e^{-ik\zeta}, \quad k \neq 0 \tag{2.14}$$

This expression is worth noting because it provides the link between the global Fourier measurements we are given and the local features (edges) we are interested in approximating. Substituting

this expression in (2.3), we get

$$\begin{aligned} S_N^\sigma[f](x) &= \sum_{0<|k|\leq N} \hat{f}(k) i\sigma\left(\frac{|k|}{N}\right) \text{sgn}(k) e^{ikx} \\ &= \sum_{0<|k|\leq N} \left[\frac{1}{2\pi}\left(\frac{[f](\zeta)}{ik} + \frac{[f'](\zeta)}{(ik)^2} + \frac{[f''](\zeta)}{(ik)^3} + ...\right) e^{-ik\zeta}\right] i\sigma\left(\frac{|k|}{N}\right) \text{sgn}(k) e^{ikx} \\ &= \frac{[f](\zeta)}{2\pi} \sum_{0<|k|\leq N} \frac{\sigma\left(\frac{|k|}{N}\right)\text{sgn}(k)}{k} e^{ik(x-\zeta)} + \frac{[f'](\zeta)}{2\pi} \sum_{0<|k|\leq N} \frac{\sigma\left(\frac{|k|}{N}\right)\text{sgn}(k)}{ik^2} e^{ik(x-\zeta)} \\ &\qquad + \frac{[f''](\zeta)}{2\pi} \sum_{0<|k|\leq N} \frac{\sigma\left(\frac{|k|}{N}\right)\text{sgn}(k)}{i^2k^3} e^{ik(x-\zeta)} + ... \end{aligned} \tag{2.15}$$

Recall that the first term in the above equation is a shifted and scaled jump response, $W_0^{\sigma,N}$, (Definition 2). Similarly we may define

$$\frac{1}{2\pi} \sum_{0<|k|\leq N} \frac{\sigma\left(\frac{|k|}{N}\right)\text{sgn}(k)}{ik^2} e^{ikx} := W_1^{\sigma,N}(x) \tag{2.16}$$

and, in general,

$$\frac{1}{2\pi} \sum_{0<|k|\leq N} \frac{\sigma\left(\frac{|k|}{N}\right)\text{sgn}(k)}{i^q k^{q+1}} e^{ikx} := W_q^{\sigma,N}(x) \tag{2.17}$$

Substituting in (2.15), we obtain

$$S_N^\sigma[f](x) = [f](\zeta)W_0^{\sigma,N}(x-\zeta) + [f'](\zeta)W_1^{\sigma,N}(x-\zeta) + [f''](\zeta)W_2^{\sigma,N}(x-\zeta) + ... \tag{2.18}$$

There arises a technical difficulty in using the above formulation for analysis, since the jump "function" is zero everywhere, except at a finite set of points. Therefore, convolutions involving this quantity would evaluate to zero. However, this is easily overcome using a regularized equivalent of the jump function (motivated by the development in [11]), which we denote by $[f]_\epsilon(x)$, and define as

$$[f]_\epsilon(x) = \begin{cases} [f](\zeta) & |x-\zeta| \leq \epsilon,\ \epsilon > 0, \epsilon \sim \mathcal{O}\left(\frac{2\pi}{2N+1}\right) \\ 0 & \text{else} \end{cases} \tag{2.19}$$

Thus, (2.18) becomes

$$\begin{aligned} S_N^\sigma[f](x) &\approx [f]_\epsilon(\zeta)W_0^{\sigma,N}(x-\zeta) + [f']_\epsilon(\zeta)W_1^{\sigma,N}(x-\zeta) + [f'']_\epsilon(\zeta)W_2^{\sigma,N}(x-\zeta) + ... \\ &\approx \int_{-\pi}^{\pi} [f]_\epsilon(\zeta)W_0^{\sigma,N}(x-\zeta)d\zeta + \int_{-\pi}^{\pi} [f']_\epsilon(\zeta)W_1^{\sigma,N}(x-\zeta)d\zeta + \int_{-\pi}^{\pi} [f'']_\epsilon(\zeta)W_2^{\sigma,N}(x-\zeta)d\zeta + ... \\ &= ([f]_\epsilon * W_0^{\sigma,N})(x) + ([f']_\epsilon * W_1^{\sigma,N})(x) + ([f'']_\epsilon * W_2^{\sigma,N})(x) + ... \end{aligned} \tag{2.20}$$

We note that $W_i^{\sigma,N}(x) = (\tilde{B}_i * C_N^{\sigma})(x)$, where $\tilde{B}_i(x)$ are normalized Bernoulli polynomials, [19], and $C_N^{\sigma}(x)$ is the concentration kernel (2.4). Since the i^{th} Bernoulli polynomial has a discontinuity in its i^{th} derivative at $x = 0$, each of these kernels denotes the response of the concentration sum to jumps in the i^{th} derivative of the function. Our attention, however, will be restricted to the identification of jumps and $W_0^{\sigma,N}$, the jump response. The jump response and the first three higher-order kernels associated with the polynomial concentration factor are plotted for illustrative purposes in Figure 2.5. Note the alternating even-odd nature of the kernels and the reduced scale of the higher order kernel plots.

2.4 Concentration Factor Design

Expression (2.20) provides us with a convenient starting point to discuss concentration factor design. As previously discussed, the design of a concentration factor is important since it determines the qualities of the resulting jump function approximation. To accurately approximate the jump function, it is obvious from (2.20) that $W_0^{\sigma,N}(x)$ has to be emphasized, while simultaneously suppressing $W_i^{\sigma,N}(x), i > 0$. Moreover, for a well resolved jump approximation, we require that $W_0^{\sigma,N}(x)$ have properties similar to the indicator function

$$\delta(x) = \begin{cases} 1 & x = 0 \\ 0 & \text{else} \end{cases} \tag{2.21}$$

The design framework therefore consists of solving an iterative program which computes a concentration factor σ for (2.3) such that the above conditions are satisfied. A typical problem formulation takes the form

$$\begin{aligned} \min_{\sigma} \quad & \phi_0(\sigma) \\ \text{subject to} \quad & \phi_m(\sigma) = c_m, \quad m = 1, ..., M \\ & \psi_n(\sigma) \leq c_n, \quad n = 1, ...N \end{aligned} \tag{2.22}$$

The objective function ϕ_0 is typically a norm measure of $W_0^{\sigma,N}(x)$. c_m, c_n are constants or functions independent of σ while the constraints, $\phi_m(\sigma), \psi_n(\sigma)$, are typically functions of $W_i^{\sigma,N}(x)$ or σ. Note that σ is an even function (this follows from the admissibility condition requiring the

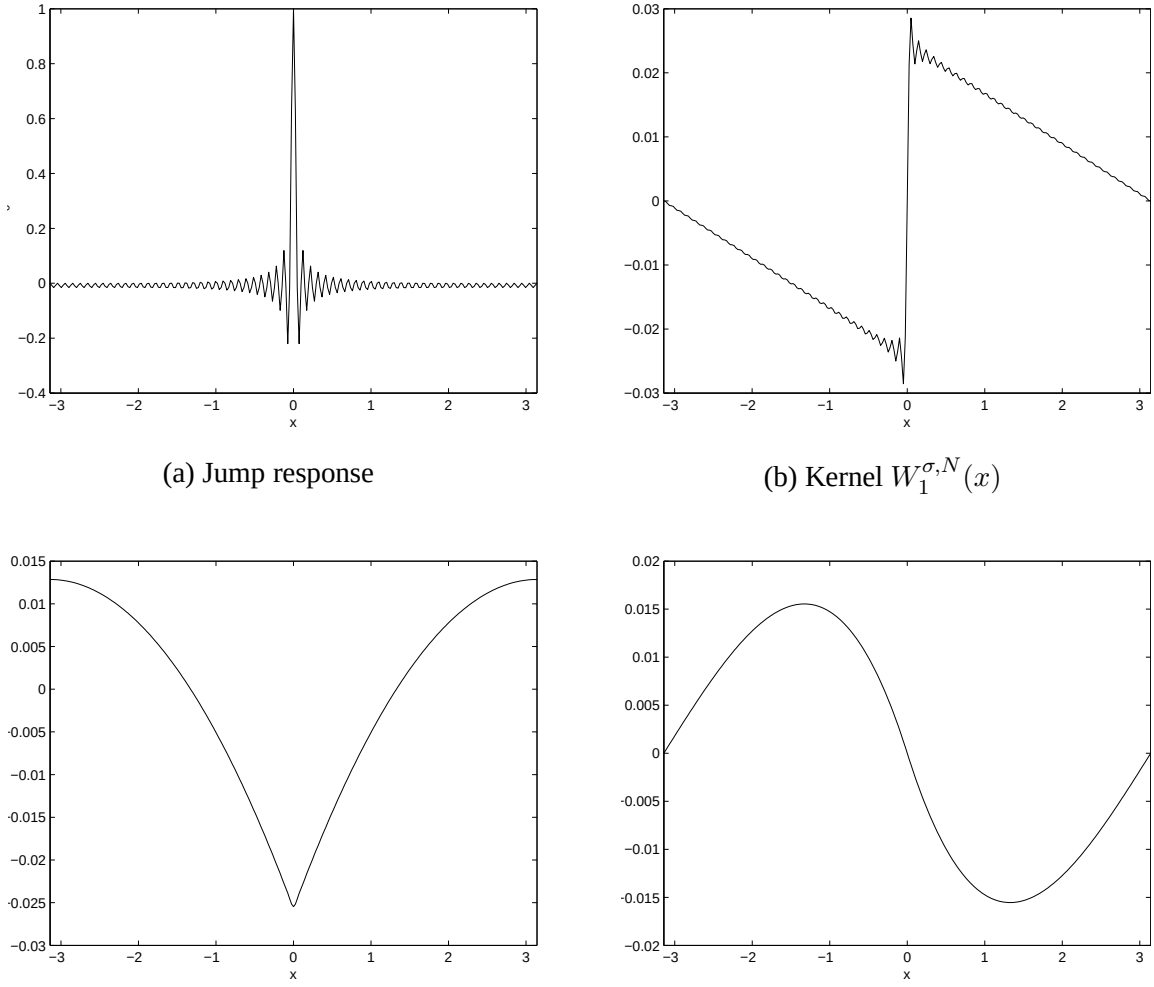

(a) Jump response

(b) Kernel $W_1^{\sigma,N}(x)$

(c) Kernel $W_2^{\sigma,N}(x)$

(d) Kernel $W_3^{\sigma,N}(x)$

Fig. 2.5: The jump response and first three higher order kernels associated with the polynomial concentration factor ($N = 64$)

concentration kernel (2.4) to be odd). Consequently, the design problem is an iterative program of size N.

2.4.1 Sample Problem Formulations

In the following discussion, we provide several sample problem formulations. All problem formulations discussed below are convex programs, with most being linear programs or quadratic programs with linear equalities and inequalities. In broad brush, they can all be formulated as second order cone programs (SOCPs), which can be solved using a variety of methods, [20]. The simulation

results in this section were computed using CVX, a package for specifying and solving convex programs [21, 22]. Programs were implemented in Matlab (version 7.7) with CVX version 1.2 (build 711).

1. Problem Formulation 1 - *The (first-order) polynomial concentration factor*

   We start with a problem formulation minimizing the 2-norm of the jump waveform $W_0^{\sigma,N}(x)$, while ensuring its proper normalization.

$$\begin{aligned} \min_{\sigma} \quad & \| W_0^{\sigma,N} \|_2 \\ \text{subject to} \quad & W_0^{\sigma,N}\Big|_{x=0} = 1 \end{aligned} \tag{2.23}$$

   This results in a concentration factor and jump response as plotted in Figure 2.6.

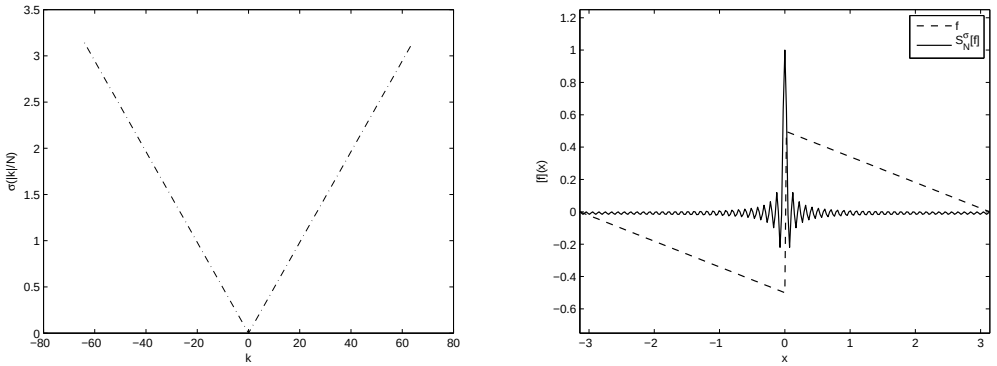

(a) Concentration Factor (b) Jump Response

Fig. 2.6: Problem formulation 1, $N = 64$

By comparing Figure 2.6 with Figures 2.2 and 2.3, it is clear that this problem formulation results in the first-order polynomial concentration factor. This observation may be formalized in the following theorem:

Theorem 2.4.1. *Let $W_0^{\sigma,N}$ be the jump response. The concentration factor $\sigma(\eta) = \sigma\left(\frac{|k|}{N}\right)$ which solves the problem*

$$\begin{aligned} \min_{\sigma} \quad & \| W_0^{\sigma,N} \|_2 \\ \textit{subject to} \quad & W_0^{\sigma,N}\Big|_{x=0} = 1 \end{aligned} \tag{2.24}$$

is the first-order polynomial concentration factor, $\sigma_P^1(\eta) = \pi\eta$.

Proof. By Parseval's relation, we have

$$\begin{aligned}\left\|W_0^{\sigma,N}\right\|_2 &= \left(\sum_{0<|k|\leq N}\left|\frac{\sigma\left(\frac{|k|}{N}\right)\operatorname{sgn}(k)}{k}\right|^2\right)^{\frac{1}{2}} \\ &= \left(\sum_{0<|k|\leq N}\left|\frac{\sigma\left(\frac{|k|}{N}\right)}{|k|}\right|^2\right)^{\frac{1}{2}}\end{aligned} \tag{2.25}$$

By defining $\eta = \frac{|k|}{N}$, the above expression becomes

$$\left\|W_0^{\sigma,N}\right\|_2 = \frac{1}{N}\left(\sum_{0<\eta\leq 1}\left|\frac{\sigma(\eta)}{\eta}\right|^2\right)^{\frac{1}{2}} \tag{2.26}$$

The error is minimized when each term in the sum is minimized. Setting $\dfrac{d}{d\eta}\left(\dfrac{\sigma(\eta)}{\eta}\right)^2$ to zero, we obtain

$$2\left(\frac{\sigma(\eta)}{\eta}\right)\cdot\left(\frac{\eta\sigma'(\eta)-\sigma(\eta)}{\eta^2}\right) = 0$$

Since $\eta \neq 0$, we have

$$\eta\sigma'(\eta) = \sigma(\eta)$$

The solution of this equation takes the form

$$\sigma(\eta) = C\cdot\eta \tag{2.27}$$

where C is some constant. We determine C using the equality constraint, $W_0^{\sigma,N}\Big|_{x=0} = 1$.

$$\begin{aligned}\frac{1}{2\pi}\sum_{0<|k|\leq N}\frac{\sigma\left(\frac{|k|}{N}\right)\operatorname{sgn}(k)}{k} &= 1 \\ \frac{1}{\pi N}\sum_{\eta=1/N}^{1}\frac{\sigma(\eta)}{\eta} &= 1 \\ \frac{C}{\pi N}\cdot N &= 1 \\ C &= \pi\end{aligned} \tag{2.28}$$

The result follows. □

2. Problem Formulation 2 - *Sparse jump response*

   A quick study of the jump response of the polynomial concentration factor reveals strong oscillations in the smooth regions. Therefore, we consider a problem formulation where we minimize the 1-norm of the jump waveform $W_0^{\sigma,N}(x)$, subject to the usual normalization constraint.

$$\begin{aligned} \min_{\sigma} \quad & \| W_0^{\sigma,N} \|_1 \\ \text{subject to} \quad & W_0^{\sigma,N}\Big|_{x=0} = 1 \end{aligned} \tag{2.29}$$

   This results in a concentration factor and jump response as plotted in Figure 2.7.

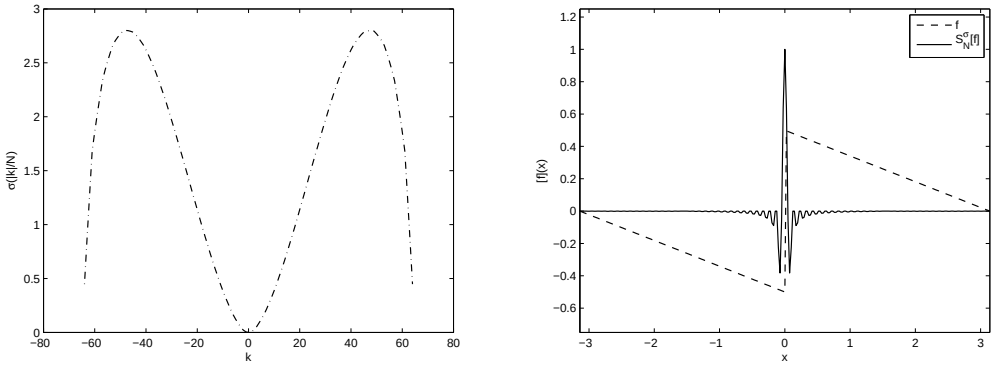

(a) Concentration Factor (b) Jump Response

Fig. 2.7: Problem formulation 2, $N = 64$

As expected, the response in smooth regions is much smaller at the expense of decreased resolution of the actual jump and strong oscillatory sidelobes in the immediate vicinity of the jump. These characteristics are in evidence in the plots of Figure 2.8. This figure plots the absolute logarithmic error between the true jump function and the concentration jump response. The error plots for different values of N are provided to infer convergence behavior. The almost flat error profile away from the jump in Figure 2.8 (a) is a result of the slowly decaying oscillations. In comparison, the concentration factor from problem formulation 2 shows a vanishing response in the same region in Figure 2.8 (b).

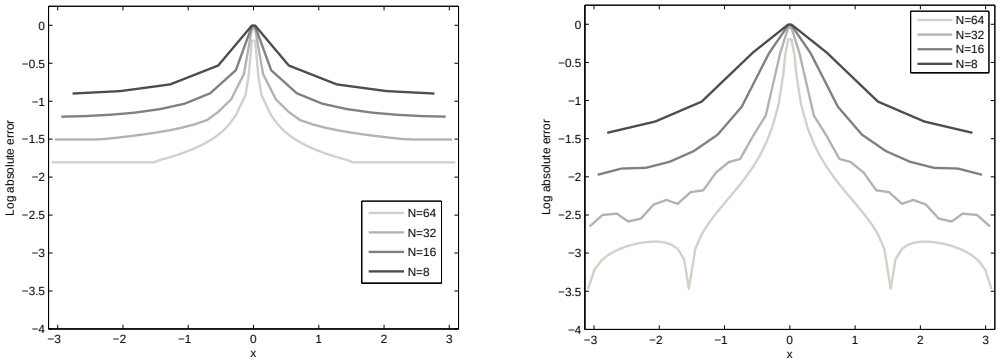

(a) Problem formulation 1 (b) Problem formulation 2

Fig. 2.8: Log absolute error between the true jump function and the concentration jump approximation, $N = 64$

3. Problem Formulation 3 - *Higher order concentration factors*

The previous problem formulations imposed no constraints on the magnitude of the higher

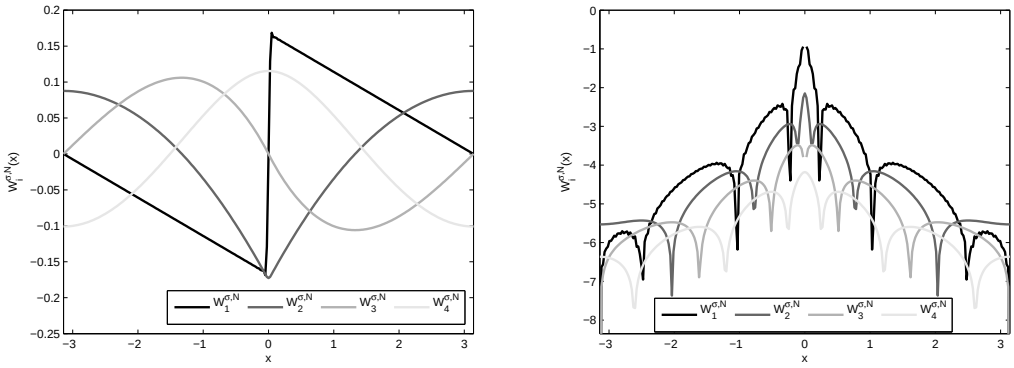

(a) Trigonometric concentration factor (b) Exponential concentration factor

Fig. 2.9: Plot of the higher-order kernels, $W_i^{\sigma,N}, i = 1, .., 4$, ($N = 64$)

order kernels. This can present a problem when computing jump approximations for functions with significant variation. Figure 2.4 (b) provides an example, where the jump function approximations of $f_2(x)$ using the (low-order) trigonometric and (high-order) exponential concentration factors are plotted. For reference, Figure 2.9 plots the first four higher-order kernels, $W_i^{\sigma,N}, i = 1, .., 4$, for the trigonometric and exponential concentration factors re-

spectively. Note the logarithmic scale and the significantly reduced values of the kernels for the exponential concentration factor.

Clearly, there is a lot to gain in this context by imposing constraints on the higher-order kernels[6]. Therefore, consider the problem formulation,

$$\begin{aligned} \min_{\sigma} \quad & \| W_0^{\sigma,N} \|_1 \\ \text{subject to} \quad & W_0^{\sigma,N}\Big|_{x=0} = 1 \\ & \left\| W_1^{\sigma,N} \right\|_\infty \leq 10^{-1} \\ & \left\| W_2^{\sigma,N} \right\|_\infty \leq 10^{-3} \\ & \sigma \geq 0,\, \sigma(1) = 0 \end{aligned} \tag{2.30}$$

This results in a concentration factor and jump response as plotted in Figure 2.10.

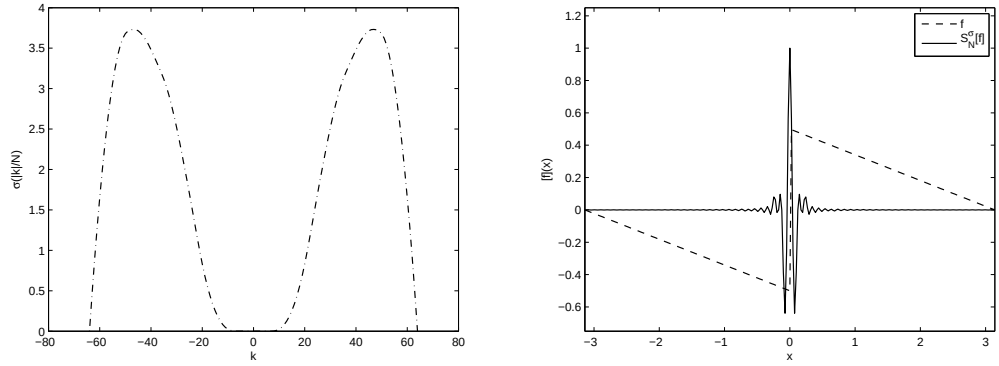

(a) Concentration Factor (b) Jump Response

Fig. 2.10: Problem formulation 3, $N = 64$

Figure 2.11 plots the response of the factors from problem formulations 2 and 3 respectively to the test function $f_2(x)$, (2.10). Note the significantly improved performance using problem formulation 3 with respect to canceling out oscillatory signals. Problem formulation 2 had no constraints on the higher order kernels; consequently, the jump response in Figure 2.11 (a) shows a significant

[6]Ideally, the higher-order kernels should be vanishingly small. Programming constraints, however, make it difficult to do so.

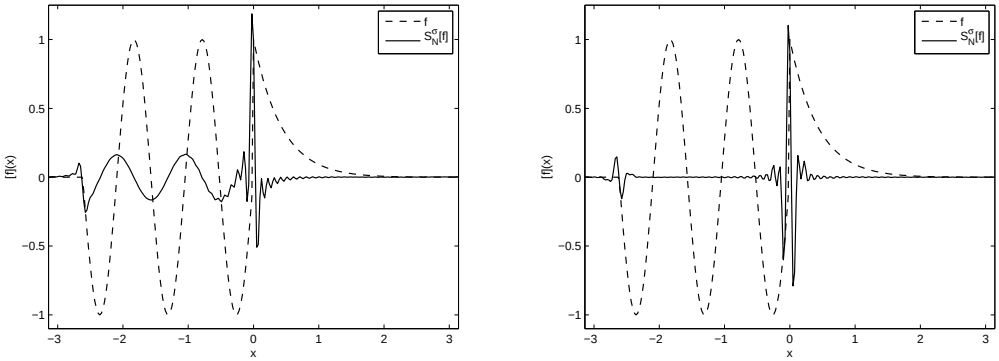

(a) Prob. formulation 2 (Low order factor) (b) Prob. formulation 3 (High order factor)

Fig. 2.11: Comparison of low and high-order concentration jump approximations, $N = 64$

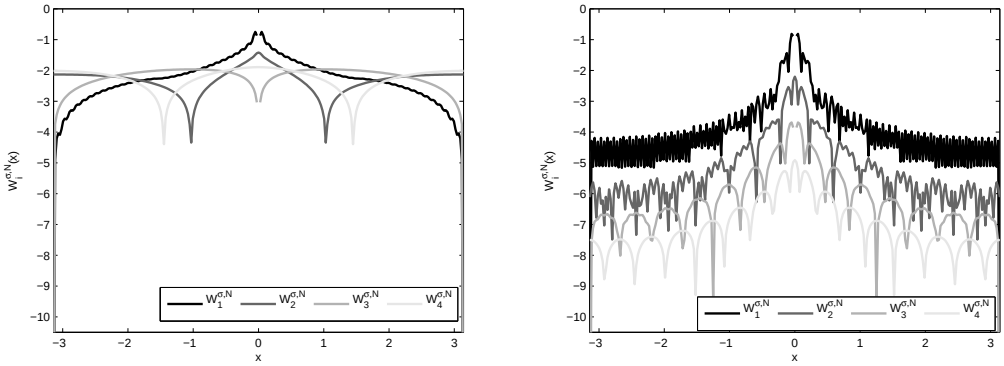

(a) Problem formulation 2 (b) Problem formulation 3

Fig. 2.12: Logarithmic plot of the higher-order kernels, $W_i^{\sigma,N}, i = 1, .., 4$, ($N = 64$)

non-zero value in the sinusoidal region. The corresponding response in Figure 2.11 (b) is near zero[7]. Plots of the first four higher-order kernels corresponding to the two concentration factors are given in Figure 2.12. Note the significantly smaller values for problem formulation 3. Note that the exponential factor was designed to cancel out as many moments as the order of the factor, [10]. Problem formulation 3 serves the same purpose by canceling out several higher-order kernels. The interested reader is also encouraged to compare the performance of the factor from problem

[7] As before, the small oscillatory response in the vicinity of $x = -\frac{5\pi}{6}$ is due to the discontinuities in the derivative and higher-order derivatives of $f_2(x)$.

formulation 3 to the exponential concentration factor. The jump function approximations using the two factors are plotted in Figure 2.4 (b) and Figure 2.11 (b) respectively, while the plots of the higher-order kernels are provided in Figure 2.9 (b) and Figure 2.12 (b) respectively. It is observed that the concentration factor from the iterative formulation is more effective in canceling out the oscillatory response in the sinusoidal region. However, it is entirely possible that a set of similar constraints in the iterative program exist, which will yield a solution numerically equivalent to the exponential concentration factor.

It is envisaged that such a concentration factor may be useful in applications where functions with large variation are encountered, such as the solution of PDEs by spectral methods involving highly oscillatory solutions.

4. Problem Formulation 4 - *Missing or Banded Spectral Data*

   Consider the problem of identifying jump information from spectral data missing certain coefficients, perhaps due to instrumentation errors or noise. The use of standard concentration factors in such cases results in additional spurious oscillations throughout the reconstruction interval, as illustrated in Figure 2.13. This figure plots the jump response to a unit ramp using the polynomial factor and the concentration factor designed in problem formulation 2. Fourier modes $\mathbb{K} \in \{-40, -39, ..., -30, 30, 31, ..., 40\}$ are assumed missing.

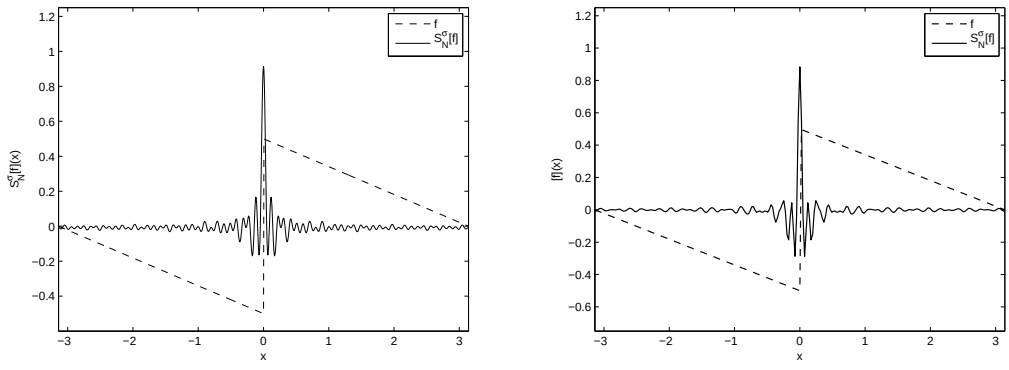

(a) Polynomial factor

(b) Concentration factor from problem formulation 2

Fig. 2.13: Use of standard concentration factors with missing data, $N = 64$

These additional spurious responses can lead to false jump detects, especially in the pres-

ence of noise. However, explicitly specifying the missing data as a constraint in the problem formulation allows us to produce much cleaner jump responses. For example, consider:

$$\begin{aligned} \min_{\sigma} \quad & \| W_0^{\sigma,N} \|_1 \\ \text{subject to} \quad & W_0^{\sigma,N}\Big|_{x=0} = 1 \\ & \sigma(\mathbb{K}) = 0 \\ & \Big| W_0^{\sigma,N} \Big|_{|x|\geq 0.35} \leq 10^{-3} \end{aligned} \tag{2.31}$$

This results in a concentration factor and jump response as plotted in Figure 2.14. Note the significantly reduced spurious oscillations away from the jump. The one consequence of the missing data, however, is the slightly reduced resolution of the jump itself. Also, note that the envelope of the concentration factor in Fourier space contains no sharp discontinuities. This implicit smoothness plays a significant role in minimizing spurious oscillations.

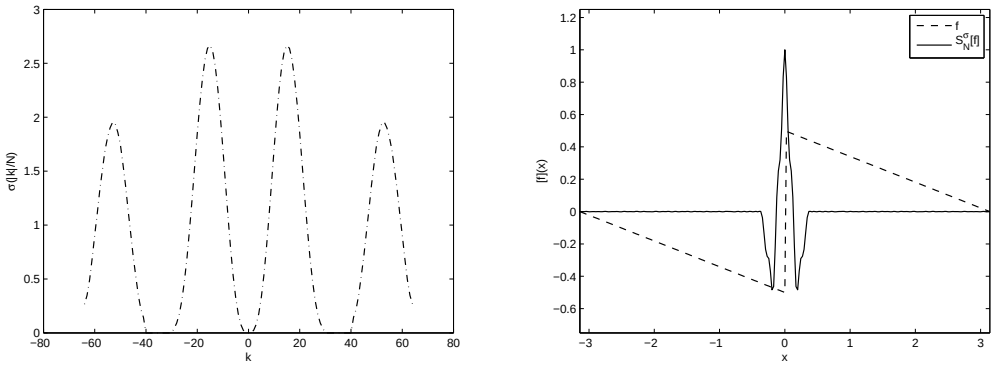

(a) Concentration Factor (b) Jump Response

Fig. 2.14: Concentration factor design for missing data, $N = 64$, modes $\pm(30 - 40)$ missing.

Figure 2.15 plots the performance of the factor on the following test function.

$$f_3(x) = \begin{cases} \sin(x) & -\pi \leq x < -\frac{\pi}{2} \\ -\cos\left(\frac{3x}{2}\right) & -\frac{\pi}{2} < x < \frac{\pi}{4} \\ \pi - x & \frac{\pi}{4} < x \leq \pi \end{cases} \tag{2.32}$$

$$[f]_3(x) = \begin{cases} \frac{\sqrt{2}+1}{\sqrt{2}} \approx 1.707 & x = -\frac{\pi}{2} \\ \frac{3\pi}{4} + \frac{1}{2}\sqrt{2-\sqrt{2}} \approx 2.734 & x = \frac{\pi}{4} \\ 0 & \text{else} \end{cases} \tag{2.33}$$

The associated jump function is provided for reference in (2.33). As before, we note that the jump approximation is much cleaner. Moreover, with the standard concentration factors, the jump heights are not identified correctly. Recall (Section 2.1, admissibility conditions) that the concentration factors are required to satisfy a normalization constraint. This constraint is violated in the case of missing data, i.e., for the standard concentration factors

$$\sum_{\substack{k=1 \\ k\notin\mathbb{K}}}^{N} \frac{\sigma\left(\frac{|k|}{N}\right)}{k} < \sum_{k=1}^{N} \frac{\sigma\left(\frac{|k|}{N}\right)}{k} = 1$$

Consequently, the jump response has the property that $W_0^{\sigma,N}(0) < 1$. This results in the jump height being incorrectly identified. It is only when the missing modes are explicitly modeled in the design process that the resulting concentration factor is suitably normalized, with

$$\sum_{\substack{k=1 \\ k\notin\mathbb{K}}}^{N} \frac{\sigma_{\text{mis}}\left(\frac{|k|}{N}\right)}{k} = 1$$

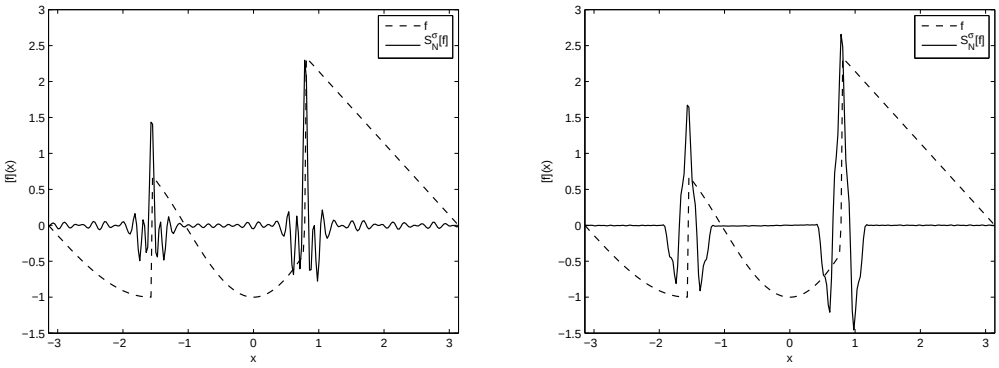

(a) Concentration factor from problem formulation 2

(b) Concentration factor from solving (2.31)

Fig. 2.15: Jump approximation of $f_3(x)$ from its Fourier modes, $N = 64$, modes $\pm(30-40)$ missing.

2.5 Obtaining Sparse Jump Function Approximations

The concentration edge detection method computes a Fourier partial sum approximation to the jump function, $[f]$. Since $[f]$ is piecewise-defined, its approximation suffers from the Gibbs phenomenon, and its associated slow and non-uniform convergence issues. A binary decision on the presence or absence of an edge is taken by thresholding this approximation, with optional post-processing operations. The slow convergence, however, ensures that the final result suffers from poor resolution of jumps, with several false alarms in the immediate vicinity of a true jump, and spurious activations in smooth regions. The presence of noise only accentuates the problem, making accurate identification of jump locations challenging.

In this section, we summarize the design of an edge detector based on the relation in (2.18), and consider the case when the Fourier data is corrupted by noise. This detector was first introduced in [3] and extended in [15]. These designs essentially identified unit sized jumps in the data, while the formulation below accounts for jumps of unknown, but deterministic sizes in the data. The resulting detector retains the same form of [15], but with modified performance bounds.

For functions with minimal variation, or when using high-order concentration factors, we have from (2.18),

$$S_N^\sigma[f](x) \approx [f](\zeta) W_0^{\sigma,N}(x-\zeta) \tag{2.34}$$

where ζ denotes the jump location. We will assume that the Fourier modes are corrupted with additive white complex Gaussian noise[8] of variance ρ^2, i.e.,

$$\hat{\mathbf{g}}(k) = \hat{f}(k) + \hat{\mathbf{v}}(k) \quad k \in [-N, N],\ \hat{\mathbf{v}}(k) \sim \mathcal{CN}[0, \rho^2] \tag{2.35}$$

We start by characterizing the statistical properties of the jump function approximation. Since the concentration method is linear, we have

$$\mathrm{E}\left[S_N^\sigma[\mathbf{g}](x)\right] = \mathrm{E}\left[S_N^\sigma[f](x) + S_N^\sigma[\mathbf{v}](x)\right] = S_N^\sigma[f](x) \tag{2.36}$$

Moreover, the noise component $S_N^\sigma[v](x)$ acquires a covariance structure on account of the action of the concentration factors on the i.i.d. noise coefficients. This covariance structure is given by the

[8] In this section, we use bold script to denote statistically random quantities.

following lemma:

Lemma 2.5.1. *Let $S_N^{\sigma_p}[\mathbf{g}](x_a)$ denote the jump function approximation computed at location x_a using the concentration factor σ_p, and $S_N^{\sigma_q}[\mathbf{g}](x_b)$ denote the jump function approximation computed at location x_b using the concentration factor σ_q. Then,*

$$(C_{\mathbf{v}})_{p,q}^{x_a,x_b} = \rho^2 \sum_{l=-N}^{N} \sigma_p\left(\frac{|l|}{N}\right) \sigma_q\left(\frac{|l|}{N}\right) e^{il(x_a-x_b)}$$

Proof. By definition,

$$\begin{aligned}
(C_{\mathbf{v}})_{p,q}^{x_a,x_b} &= \mathrm{E}\left[\left(S_N^{\sigma_p}[\mathbf{g}](x_a) - \mathrm{E}\left[S_N^{\sigma_p}[\mathbf{g}](x_a)\right]\right)\left(S_N^{\sigma_q}[\mathbf{g}](x_b) - \mathrm{E}\left[S_N^{\sigma_q}[\mathbf{g}](x_b)\right]\right)^*\right] \\
&= \mathrm{E}\left[\left(S_N^{\sigma_p}[\mathbf{v}](x_a)\right)\left(S_N^{\sigma_q}[\mathbf{v}](x_b)\right)^*\right] \\
&= \mathrm{E}\left[\left(i\sum_{l=-N}^{N} \hat{\mathbf{v}}(l)\,\mathrm{sgn}(l)\,\sigma_p(\frac{|l|}{N})\,e^{ilx_a}\right)\left(-i\sum_{m=-N}^{N} \hat{\mathbf{v}}(m)^*\,\mathrm{sgn}(m)\,\sigma_q(\frac{|m|}{N})\,e^{-imx_b}\right)\right] \\
&= \mathrm{E}\left[\sum_{l=-N}^{N} |\hat{\mathbf{v}}(l)|^2 \sigma_p(\frac{|l|}{N})\sigma_q(\frac{|l|}{N})\,e^{il(x_a-x_b)}\right] \\
&\quad + \mathrm{E}\left[\sum_{m=-N}^{N}\sum_{\substack{l=-N \\ m\neq l}}^{N} \hat{\mathbf{v}}(m)^*\,\hat{\mathbf{v}}(l)\,\mathrm{sgn}(m)\,\mathrm{sgn}(l)\,\sigma_q(\frac{|m|}{N})\,\sigma_p(\frac{|l|}{N})\,e^{-imx_b}e^{ilx_a}\right]
\end{aligned}$$

$$\begin{aligned}
(C_{\mathbf{v}})_{p,q}^{x_a,x_b} &= \sum_{l=-N}^{N} \mathrm{E}\left[|\hat{\mathbf{v}}(l)|^2\right] \sigma_p(\frac{|l|}{N})\,\sigma_q(\frac{|l|}{N})\,e^{il(x_a-x_b)} \\
&\quad + \sum_{m=-N}^{N}\sum_{\substack{l=-N \\ m\neq l}}^{N} \mathrm{E}\left[\hat{\mathbf{v}}(m)^*\,\hat{\mathbf{v}}(l)\right]\mathrm{sgn}(m)\,\mathrm{sgn}(l)\,\sigma_q(\frac{|m|}{N})\,\sigma_p(\frac{|l|}{N})\,e^{-imx_b}e^{ilx_a}
\end{aligned}$$

where the second equation results from using (2.36). Since $\mathbf{v}(l),\ l \in [-N, N]$, are independent and zero mean variates, $\mathrm{E}\left[\hat{\mathbf{v}}(m)^*\,\hat{\mathbf{v}}(l)\right] = \mathrm{E}\left[\hat{\mathbf{v}}(m)^*\right]\mathrm{E}\left[\hat{\mathbf{v}}(l)\right] = 0$ for $m \neq l$. Hence the second term in the above expression vanishes. Using $\mathrm{E}\left[|\hat{\mathbf{v}}(l)|^2\right] = \rho^2$, we have

$$(C_{\mathbf{v}})_{p,q}^{x_a,x_b} = \rho^2 \sum_{l=-N}^{N} \sigma_p(\frac{|l|}{N})\sigma_q(\frac{|l|}{N})e^{il(x_a-x_b)}$$

□

2.5.1 Detector Design

We consider the design of a detector which takes P evaluations of $S_N^\sigma[\mathbf{g}](x)$ in a neighborhood $\mathcal{P}$ of a point, and returns one of the following hypotheses: $\mathcal{H}_1$ – edge present, or $\mathcal{H}_0$ – edge absent. Let W denote a P-point discretization of the jump response, $W_0^{\sigma,N}(x)$, and $\mathbf{Y} = \{S_N^\sigma[\mathbf{g}](x_p)\}_{p\in\mathcal{P}}$. If $\mathbf{V}$ denotes a length P noise vector, we have

$$\begin{aligned} \mathcal{H}_0: \quad \mathbf{Y} &= \mathbf{V} && \sim \mathcal{CN}[0, C_\mathbf{V}] \\ \mathcal{H}_1: \quad \mathbf{Y} &= \alpha W + \mathbf{V} && \sim \mathcal{CN}[\alpha W, C_\mathbf{V}] \end{aligned}$$

Here, $\alpha = [f](\zeta)$ is the unknown jump height, while $\mathcal{CN}[A, C]$ represents a multivariate Gaussian distribution with mean A and covariance matrix C. To maximize the probability of detection, P_D, for a given false alarm level, P_{FA}, we employ the Neyman-Pearson (NP) formulation, [23], which requires

$$\rightarrow \mathcal{H}_1: \quad \frac{p(\mathbf{Y};\alpha,\mathcal{H}_1)}{p(\mathbf{Y};\mathcal{H}_0)} > \gamma \tag{2.37}$$

The notation $\rightarrow \mathcal{H}_1$ means "choose $\mathcal{H}_1$ if", and γ denotes a threshold. The ratio in the above relation is often referred to as the likelihood ratio, $\mathcal{L}$. In our problem formulation, the likelihood ratio is the ratio of two jointly normal vectors, with

$$\begin{aligned} \mathcal{L} &= \frac{\mathcal{N}[\alpha W, C_\mathbf{V}]}{\mathcal{N}[0, C_\mathbf{V}]} \\ &= \frac{\frac{1}{(2\pi C_\mathbf{V})^{P/2}} \exp\left[-\frac{1}{2}(\mathbf{Y}-\alpha W)^T C_\mathbf{V}^{-1}(\mathbf{Y}-\alpha W)\right]}{\frac{1}{(2\pi C_\mathbf{V})^{P/2}} \exp\left[-\frac{1}{2}\mathbf{Y}^T C_\mathbf{V}^{-1}\mathbf{Y}\right]} \\ &= \exp\left[\alpha W^T C_\mathbf{V}^{-1}\mathbf{Y} - \frac{\alpha^2}{2} W^T C_\mathbf{V}^{-1} W\right] \end{aligned} \tag{2.38}$$

Taking the logarithm of the likelihood ratio and substituting in (2.37), we obtain

$$\rightarrow \mathcal{H}_1: \quad \alpha W^T C_\mathbf{V}^{-1}\mathbf{Y} - \frac{\alpha^2}{2} W^T C_\mathbf{V}^{-1} W > \log_e \gamma \tag{2.39}$$

For $\alpha > 0$, we obtain

$$\rightarrow \mathcal{H}_1: \quad W^T C_\mathbf{V}^{-1}\mathbf{Y} > \frac{\log_e \gamma}{\alpha} + \frac{\alpha}{2} W^T C_\mathbf{V}^{-1} W = \gamma' \tag{2.40}$$

We refer to the quantity $W^T C_\mathbf{V}^{-1}\mathbf{Y}$ as the test statistic and denote it as $T(\mathbf{Y})$. A detector of this form is commonly known as a generalized matched filter, [23]. Straightforward substitution reveals

that,

$$\mathcal{H}_0 : \quad T(\mathbf{Y}) \sim \mathcal{N}[0, d^2]$$

$$\mathcal{H}_1 : \quad T(\mathbf{Y}) \sim \mathcal{N}[\alpha d^2, d^2]$$

where $d^2 := W^T C_{\mathbf{V}}^{-1} W$ is known as the "signal to noise" ratio. Further, we have

$$P_{FA} = \int_{\gamma'}^{\infty} p(T|\mathcal{H}_0)(\eta) d\eta = Q\left(\frac{\gamma'}{d}\right) \tag{2.41}$$

$$P_D = \int_{\gamma'}^{\infty} p(T|\mathcal{H}_1)(\eta) d\eta = Q\left(\frac{\gamma' - \alpha d^2}{d}\right) \tag{2.42}$$

where $Q(\cdot)$ is the complementary (Gaussian) cumulative distribution function, [23], available in tabular form. Expression (2.41) is particularly useful in setting the threshold value for a given false alarm level. Moreover, the performance of the detector can be described by the following relation:

$$P_D = Q\left(Q^{-1}(P_{FA}) - \alpha\sqrt{d^2}\right) \tag{2.43}$$

The reader is also referred to [15] for a discussion on the choice of concentration factors, σ_p, σ_q, and evaluation point set $\mathcal{P}$, and their effect on detector performance.

One of the drawbacks of such a detector, however is that the above analysis applies only for $\alpha > 0$ (or $\alpha < 0$). For general α, a uniformly most powerful (UMP) test does not exist. In the simulations below, we use two separate tests for positive and negative α and combine the results. Moreover, the concentration jump function approximation is $\mathcal{O}\left(\frac{\log N}{N}\right)$ in the immediate neighborhood of a jump, (2.6). Consequently, the $\mathcal{H}_0$ hypothesis is invalid in this region. As a result, there is a strong possibility of the detector producing false activations in the immediate vicinity of a true jump. In our simulation results, we use sidelobe mitigation to avoid these false positives, with jump locations identified as the grid points which correspond to the local maximum of the test statistic $T(\mathbf{Y})$.

We remark that the design of a detector based on the Generalized Likelihood Ratio Test (GLRT), [23], is indeed possible. The design is briefly summarized below.

The GLRT test requires us to declare a jump if

$$\mathcal{L}_{\mathcal{G}} = \frac{p(\mathbf{Y}; \hat{\alpha}, \mathcal{H}_1)}{p(\mathbf{Y}; \mathcal{H}_0)} > \gamma \tag{2.44}$$

where $\hat{\alpha}$ is the maximum likelihood estimate (MLE), [24], of the jump height and γ is a threshold. Recall that $p(\mathbf{Y};\alpha) \sim \mathcal{N}[\alpha W, C_{\mathbf{V}}]$. The MLE of α is obtained by taking the likelihood of this multivariate normal distribution and setting the derivative with respect to α to zero. Direct evaluation results in

$$\hat{\alpha} = \frac{W^T C_{\mathbf{V}}^{-1} \mathbf{Y}}{W^T C_{\mathbf{V}}^{-1} W} \tag{2.45}$$

The likelihood ratio in (2.44) can be written as

$$\begin{aligned}
\mathcal{L}_{\mathcal{G}} &= \frac{p(\mathbf{Y};\hat{\alpha},\mathcal{H}_1)}{p(\mathbf{Y};\mathcal{H}_0)} \\
&= \frac{\frac{1}{(2\pi C_{\mathbf{V}})^{P/2}} \exp\left[-\frac{1}{2}(\mathbf{Y}-\hat{\alpha}W)^T C_{\mathbf{V}}^{-1}(\mathbf{Y}-\hat{\alpha}W)\right]}{\frac{1}{(2\pi C_{\mathbf{V}})^{P/2}} \exp\left[-\frac{1}{2}\mathbf{Y}^T C_{\mathbf{V}}^{-1}\mathbf{Y}\right]} \\
&= \exp\left[\hat{\alpha} W^T C_{\mathbf{V}}^{-1}\mathbf{Y} - \frac{\hat{\alpha}^2}{2} W^T C_{\mathbf{V}}^{-1} W\right] \\
&= \exp\left[\hat{\alpha}\frac{W^T C_{\mathbf{V}}^{-1}\mathbf{Y}}{W^T C_{\mathbf{V}}^{-1} W} \cdot W^T C_{\mathbf{V}}^{-1} W - \frac{\hat{\alpha}^2}{2} W^T C_{\mathbf{V}}^{-1} W\right] \\
&= \exp\left[\hat{\alpha}^2 W^T C_{\mathbf{V}}^{-1} W - \frac{\hat{\alpha}^2}{2} W^T C_{\mathbf{V}}^{-1} W\right] \\
&= \exp\left[\frac{\hat{\alpha}^2}{2} W^T C_{\mathbf{V}}^{-1} W\right]
\end{aligned} \tag{2.46}$$

where we have used (2.45) in going from step three to step four. The GLRT then requires

$$\rightarrow \mathcal{H}_1 : \exp\left[\frac{\hat{\alpha}^2}{2} W^T C_{\mathbf{V}}^{-1} W\right] > \gamma$$

Taking logs and absorbing the SNR metric $W^T C_{\mathbf{V}}^{-1} W$ into the threshold, we obtain

$$\rightarrow \mathcal{H}_1 : \hat{\alpha}^2 > \gamma'$$

$$\text{or,} \qquad \rightarrow \mathcal{H}_1 : |\hat{\alpha}| > \sqrt{\gamma'} \tag{2.47}$$

While this formulation does provide an elegant and simple form for the detector, experimental simulations reveal reduced accuracy in jump detection when compared to the NP tests described previously. In particular, the GLRT identifies strong sidelobes of the jump waveform as jumps, which are difficult to remove through post-processing. Consequently, we present results using the NP formulation in the simulations below.

Figure 2.16 illustrates the performance of such a detector. This figure considers the case with no added noise (i.e., $C_{\mathbf{V}} = I$, the identity matrix). Figure 2.16(a) plots the jump detection of test function $f_4(x)$ given in (2.48), using $101(N = 50)$ Fourier modes on a 257 point equispaced grid.

$$f_4(x) = \begin{cases} -1 & -2.5 \le x < -\frac{\pi}{4} \\ e^{-x} & 0 \le x < \frac{\pi}{4} \\ 1 + \frac{\cos(5x)}{2} & 1.25 \le x < 2.75 \\ 0 & \text{else} \end{cases} \tag{2.48}$$

$$[f]_4(x) = \begin{cases} -1 & x = -2.5 \\ 1 & x = -\frac{\pi}{4} \\ 1 & x = 0 \\ e^{-\frac{\pi}{4}} \approx 0.4559 & x = \frac{\pi}{4} \\ 1.4997 & x = 1.25 \\ 1.1888 & x = 2.75 \\ 0 & \text{else} \end{cases} \tag{2.49}$$

The trigonometric factor was used along with a detector size of $P = 5$. The jumps are identified as $\circ$'s and can be seen to correspond closely with the true jumps. A threshold[9] value of 1 was used in generating this plot. Figure 2.16(b) plots the jump detection of $f_3(x)$ using concentration factor from the missing data iterative formulation, (2.31). A value of $N = 64$ was used, with Fourier modes $30 - 40$ missing. A length 10 detector with a threshold value of 1.25 was used to generate the plot.

We next provide results for edge detection in the presence of noise. We consider the detection of jumps in test function $f_1(x)$ using the trigonometric factor, a detector size of $P = 5$ and additive noise of standard deviations $0.01, 0.02$ and 0.03. The Fourier reconstruction of the function with $101(N = 50)$ modes is plotted in Figures 2.17 (a), (c) and (e) respectively to provide a visual indication of the noise levels. The corresponding jump function approximations are plotted in Figures

[9]Ideally, thresholds are to be computed using the desired false alarm level (P_{FA}) and (2.41). Since this example contains no noise, the threshold is selected to be $0.1\, W^T C_{\mathbf{V}}^{-1} W$, i.e., to detect jumps of amplitude 0.1.

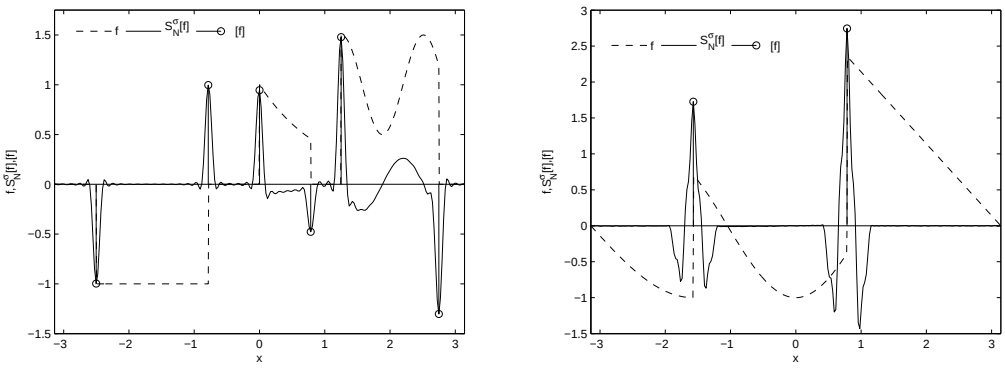

(a) Jump detection of $f_4(x)$ ($N = 50$)

(b) Jump detection of $f_3(x)$ ($N = 64$, modes $30 - 40$ missing)

Fig. 2.16: Jump detection using the matched filter detector (no noise)

Table 2.2: SNR values for the matched filter detector, $P = 5, \rho = 0.01$

	Trigonometric factor	1^{st}**-order polynomial factor**	6^{th}**-order exponential factor**
SNR (dB)	21.1245	19.6650	17.4602

2.17 (b), (d) and (f) respectively. Thresholds of $100, 40$ and 15 were used for each of the three cases. Correct identification of the jump locations (to the nearest grid point) and good accuracy of the jump values are seen in the first two cases, while a few false alarms are present in the case of high noise.

For completeness, we also plot the jump detection results using the exponential and polynomial concentration factors for the case $\rho = 0.01$ in Figure 2.18. A detector size of $P = 5$ was used with threshold values of 75 and 100 respectively. The associated signal to noise values for these concentration factors are provided in Table 2.2. The trigonometric factor is seen to perform best among the conventional families of concentration factors. This is not surprising, given that the two other factors weight the high modes in varying amounts, thereby accentuating noise in the jump function approximation.

Finally, we compare the performance of this detector with other detection schemes used in conjunction with the concentration edge detection method. Most popular among these include the

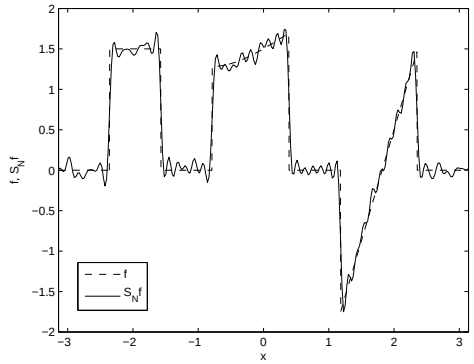

(a) Noisy Fourier reconstruction, $\rho = 0.01$

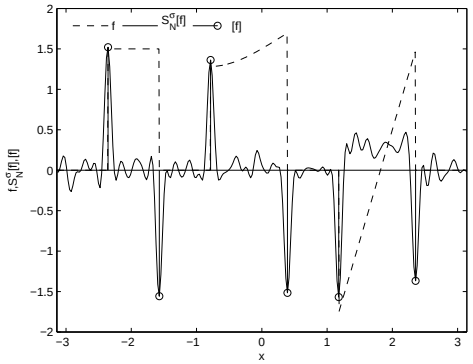

(b) Jump detection, $\rho = 0.01$

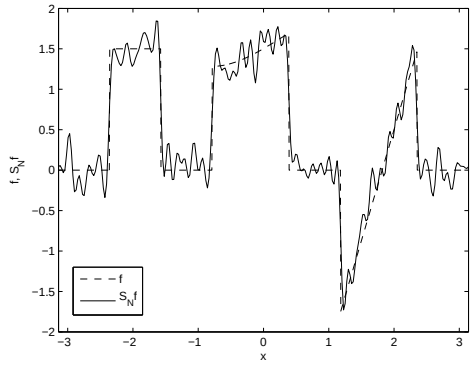

(c) Noisy Fourier reconstruction, $\rho = 0.02$

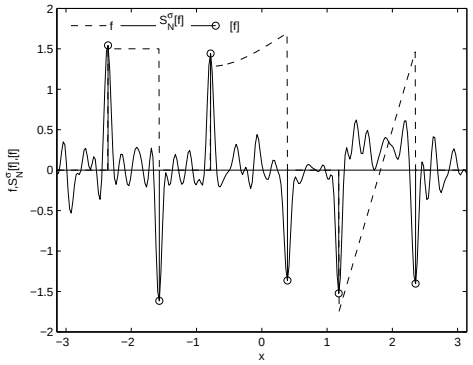

(d) Jump detection, $\rho = 0.02$

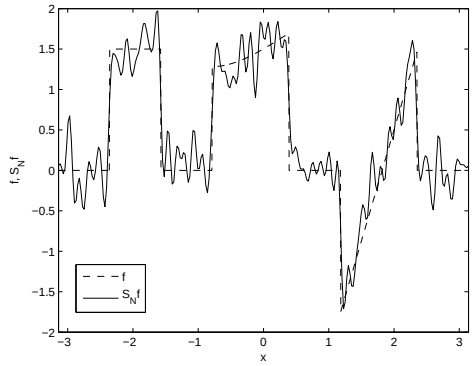

(e) Noisy Fourier reconstruction, $\rho = 0.03$

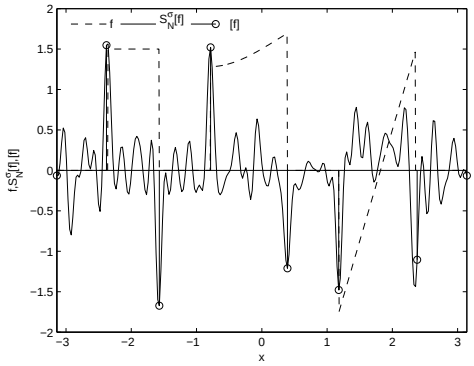

(f) Jump detection, $\rho = 0.03$

Fig. 2.17: Jump detection using the matched filter detector ($f_1(x), N = 50$)

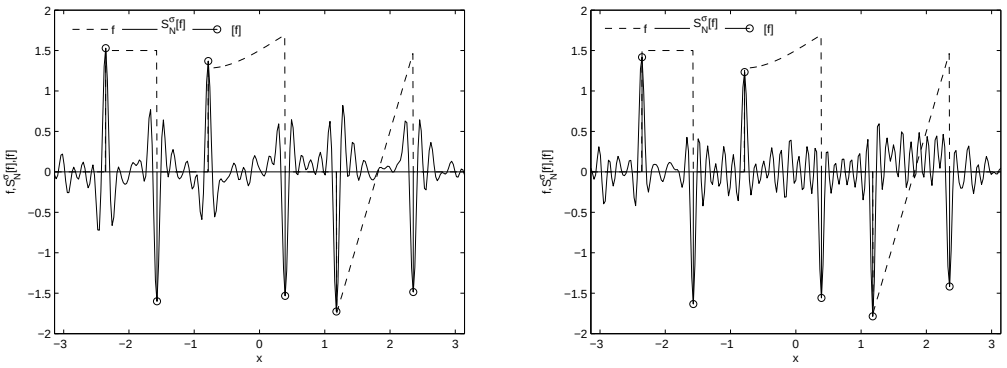

(a) Exponential factor (b) First order polynomial factor

Fig. 2.18: Jump detection using the matched filter detector ($f_1(x), N = 50, \rho = 0.01$)

method of enhancement of scales, [10], and minmod post-processing, [12]. For the purposes of this comparison, we introduce the following test function

$$f_5(x) = \begin{cases} \sin(3x) & -\pi \leq x < -\frac{\pi}{3} \\ \tanh(x) & -\frac{\pi}{3} \leq x < \frac{\pi}{2} \\ 3 - \frac{3x}{\pi} & \frac{\pi}{2} \leq x < \pi \\ 0 & \text{else} \end{cases} \tag{2.50}$$

with a jump function

$$[f]_5(x) = \begin{cases} -\tanh(-\frac{\pi}{3}) \approx -0.7807 & x = -\frac{\pi}{3} \\ 1.5 - \tanh(\frac{\pi}{2}) \approx 0.5828 & x = \frac{\pi}{2} \\ 0 & \text{else} \end{cases} \tag{2.51}$$

Figure 2.19 plots the jump detection of $f_5(x)$ using $129(N = 64)$ modes on a 257 point reconstruction grid. Additive noise of standard deviation $\rho = 0.01$ was added. Figure 2.19 (a) plots the results using the enhancement of scales post processing procedure and the trigonometric concentration factor. The jump function approximation was raised to a power of $e_p = 2$, while a uniform absolute threshold of 13 was utilized. The (scaled) enhanced jump approximation and the jump locations obtained after thresholding are plotted in the figure. False responses at $x = \frac{-\pi}{3}$ (a result of finite resolution) and a spurious activation in the sinusoidal region (due to use of a low order factor) are observed. Figure 2.19 (b) plots the minmod response, obtained by using the three concentration

factors of Table 2.1 and a threshold of 0.35. Once again, we observe several false activations. The presence of a small sized jump does not help the robustness of the method or the selection of the threshold level. Finally, Figure 2.19 (c) plots the response of the matched filter detector. A $P = 5$ point detector was employed with the central measurement computed using the polynomial factor and the rest computed using the exponential factor. A threshold value of 80 was employed to generate the plot. The responses of the two factors are also plotted for illustration. In contrast to the plots in Figures 2.19 (a) and (b), the jumps are identified correctly. In particular, the spurious response in the sinusoidal region is avoided by using a composite detector of high and low order concentration factors. Moreover, experimental simulations reveal greater robustness and leeway in the selection of the threshold.

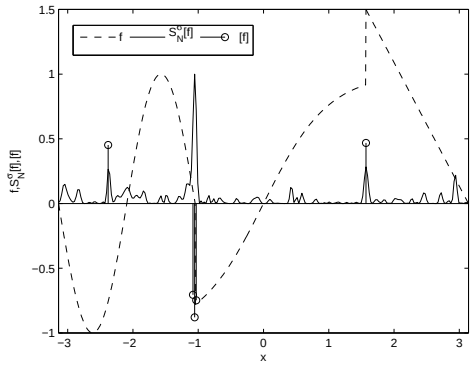

(a) Enhancement of scales, $e_p = 2$

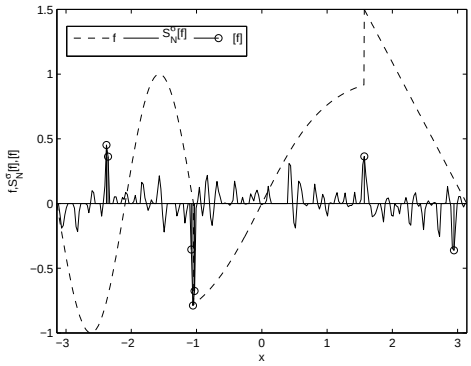

(b) Minmod detector

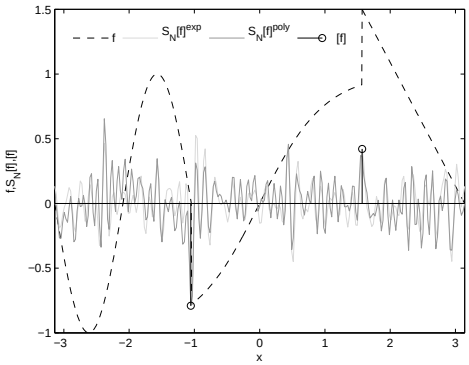

(c) Matched filter detector, $P = 5$

Fig. 2.19: Comparison of the matched filter detector with other post-processing methods ($N = 64, \rho = 0.01$)

2.6 Extension to Multiple Dimensions

This section discusses the application of the concentration method to the identification of edges in multidimensional functions. We provide examples for two-dimensional functions, although the method holds for functions of any general dimension.

From Section 2.1, it is clear that the concentration method is a partial Fourier sum approximation of the jump function, (Definition **??**). A multidimensional equivalent of the jump function, however, does not exist. Part of the difficulty in defining such a function is the lack of directionality of an edge in multiple dimensions. Nevertheless, satisfactory results may be obtained by applying the concentration method dimension by dimension, i.e.,

$$S^{\sigma}_{N,M}[f](x,\bar{y}) = i \sum_{|l|\leq N} \text{sgn}(l)\, \sigma\left(\frac{|l|}{N}\right) \sum_{|k|\leq M} \hat{f}(k,l)\, e^{i(kx+l\bar{y})} \tag{2.52}$$

The overbar represents the dimension(s) held constant, with the concentration method acting on the other dimension. Figure 2.20 illustrates the results of such an operation. The edge map of the Shepp Logan phantom is plotted on a grid of size 513 points using $N^2 = 300^2$ Fourier modes and the trigonometric factor. Figures 2.20 (a) and (b) plot the concentration jump approximations (absolute value) along each of the dimensions. Note that the two edge maps are distinct, especially in areas with horizontal and vertical edges. Figure 2.21 plots a cross-section of the horizontal edge map (absolute value) and shows properties similar to the one-dimensional concentration jump function approximation. This indicates that the edge locations may be obtained by simple thresholding, or a detector of the form discussed in Section 2.5.

The two-dimensional edge detection procedure is enumerated in the form of an algorithm below. It is an extension of the method discussed in Section 2.5. The algorithm generates edge maps in each of the directions independently by applying the concentration method to each row (column) of the image, followed by matched filter detection. The final edge map is obtained by combining the results from the horizontal and vertical directions. For example, a pixel in the final edge map may be declared an edge if either of the directional edge maps contain an edge in the same pixel. Optionally, we may choose to enforce multidimensional structure at this stage. If we assume edges to be continuous curves, disconnected responses are likely to be false positives. These may be

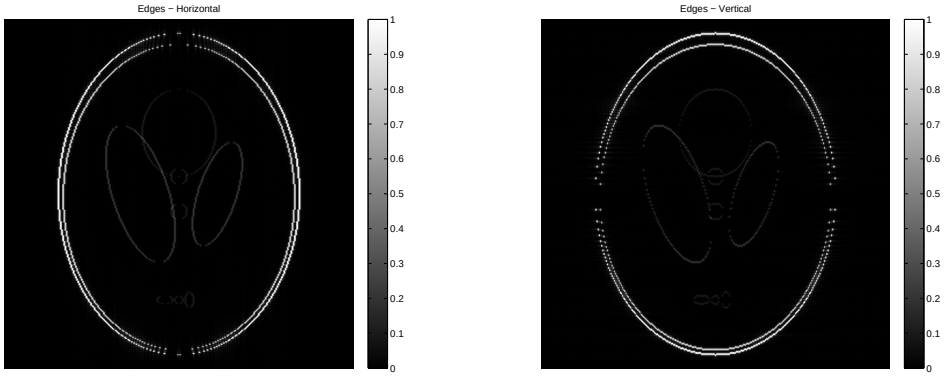

(a) Edge Map along the horizontal direction (b) Edge Map along the vertical direction

Fig. 2.20: Concentration method applied dimension by dimension ($N = 300$)

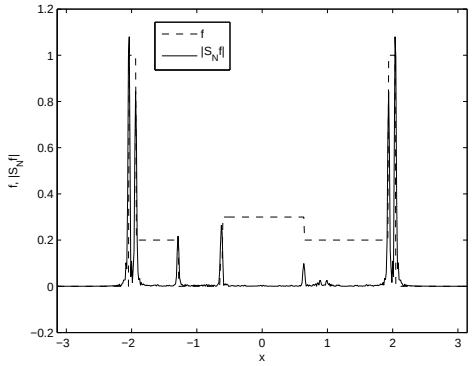

Fig. 2.21: Cross section of 2D concentration response ($N = 300$)

easily identified using masks[10], and corrected using morphological operators such as erosion[11] and dilation. It is conceivable that a more sophisticated scheme of fusing the individual edge maps may lead to improvements in the quality of the final result.

Results generated using this algorithm are plotted in Figure 2.22. The concentration jump approximation of the Shepp Logan phantom using $M = N = 200$ coefficients is plotted on a grid of

[10] A simple 3×3 mask to identify disconnected responses is as follows $\begin{bmatrix} 1 & 1 & 1 \\ 1 & 0 & 1 \\ 1 & 1 & 1 \end{bmatrix}$.

[11] Erosion and dilation, [25], are region-wise max/min operators which allow for the "filling-in" or "thinning out" of features in an image.

Algorithm 1 Multidimensional edge detection using the concentration method

Given: $\hat{f}(k,l),\ |k| \leq M, |l| \leq N$

1. Generate horizontal ($\mathcal{E}_h$) and vertical ($\mathcal{E}_v$) edge maps by applying the 1D concentration method to each row and column of f respectively, i.e.,
   - Compute the concentration jump approximations $S^{\sigma}_{N,M}[f](x,\bar{y}), S^{\sigma}_{N,M}[f](\bar{x},y)$.
   - Apply the matched filter detector of Section 2.5 to each row of $S^{\sigma}_{N,M}[f](x,\bar{y})$ and each column of $S^{\sigma}_{N,M}[f](\bar{x},y)$ to obtain the individual edge maps.
2. Obtain a composite edge map $\mathcal{E}$. A pixel in $\mathcal{E}$ is declared an edge if the corresponding pixel in either $\mathcal{E}_h$ or $\mathcal{E}_v$ is an edge.
3. (*Optional*) Enforce multidimensional structure on the edge map by removing disconnected responses and enforcing edges to be continuous curves.

size 401 points. The edge map generated using Algorithm 1 with the trigonometric concentration factor, a matched filter detector of size $P = 11$ and a detector threshold of 0.1 is plotted in Figure 2.22 (a). Comparison plots of the edge maps generated using Matlab's implementation of the Prewitt and Canny edge detectors are plotted in Figures 2.22 (b) and (c) respectively. We note that the conventional image processing edge detectors identify some of the Gibbs oscillations as edges, while the method of Algorithm 1 does not suffer from these false activations. The quality of the edge map is good with very few errors, except for a very small number of false activations in the regions of horizontal and vertical edges.

Representative results in the presence of noise are provided in Figure 2.23. We plot the edge detection of the Shepp-Logan phantom with additive white complex Gaussian noise of standard deviation $\rho = 2 \times 10^{-4}$. A visual illustration of the level of noise is provided in Figure 2.23 (a), where the Fourier reconstruction of the phantom using $N = M = 200$ coefficients is plotted. The edge map from the application of Algorithm 1 is plotted in Figure 2.23 (b). These results were generated using the trigonometric concentration factor, a matched filter detector of size $P = 5$ and a detector threshold of 8×10^3.

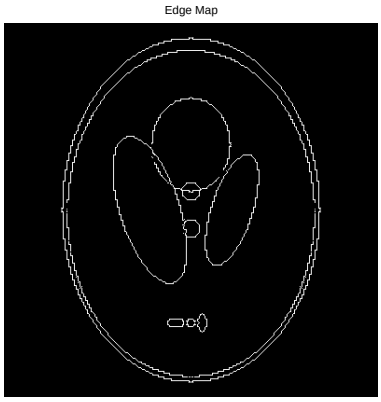

(a) Edge Map using Algorithm 1

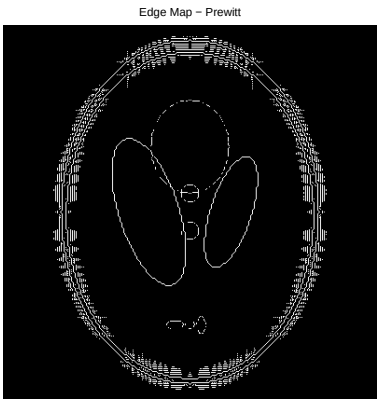

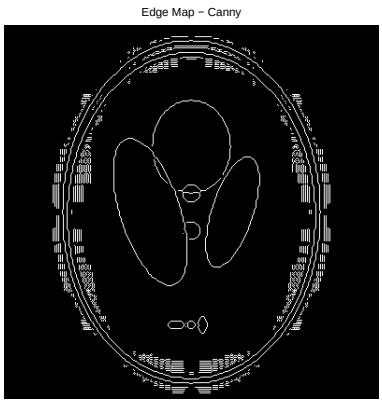

(b) Prewitt Edge detector (c) Canny Edge detector

Fig. 2.22: Edge detection – Shepp Logan phantom ($N = 300$)

2.7 IDENTIFYING JUMPS FROM NON-HARMONIC FOURIER DATA

In this section , we are interested in the problem of identifying the jumps in a function given non-harmonic or non-uniform Fourier data. This problem finds application in imaging modalities such as MRI. The underlying physics in such problems dictates that input data is collected in the Fourier domain, while instrumentation and other constraints may necessitate the collection of data along non-uniform modes.

Definition 3. *(Non-harmonic Fourier Data) Let $f \in L^2(\mathbb{R})$ be a piecewise-analytic function supported in $(-\pi, \pi)$ and zero elsewhere on the real line. We define non-harmonic Fourier data, $\hat{f}(\omega_k)$,*

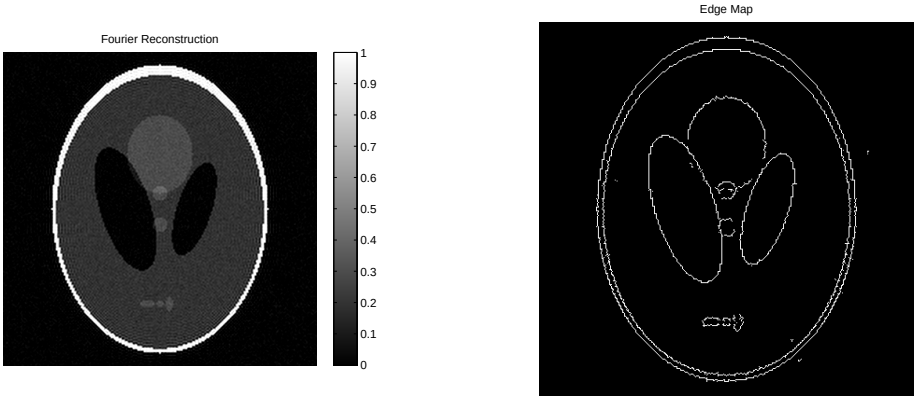

(a) Noisy Fourier reconstruction (b) Edge Map using Algorithm 1

Fig. 2.23: Edge detection in the presence of noise – Shepp Logan phantom ($N = 200, \rho = 2\times10^{-4}$)

to be the inner-products of f with the non-harmonic exponentials $\{e^{i\omega_k x}\}, \omega_k \notin \mathbb{Z}$, i.e.,

$$\hat{f}(\omega_k) := \frac{1}{2\pi}\int_{-\pi}^{\pi} f(x)e^{-i\omega_k x}, \omega_k \notin \mathbb{Z} \tag{2.53}$$

The formulation of the concentration method for non-harmonic Fourier data proceeds in a similar fashion to the standard case. Consider a compactly supported function f. For ease of analysis, let us assume that there are no jumps near the ends of the domain. We arrive at jump function approximations by convolving f with suitable convolutional kernels[12], i.e.,

$$\tilde{S}_N^\sigma[f](x) = (f * \tilde{C}_N^\sigma)(x) \tag{2.54}$$

with

$$\tilde{C}_N^\sigma(x) = \begin{cases} C_N^\sigma(x) = i\displaystyle\sum_{0<|k|\leq N} \text{sgn}(k)\sigma\left(\frac{|k|}{N}\right)e^{ikx} & |x| \leq \pi \\ 0 & \text{else} \end{cases} \tag{2.55}$$

Note that $\tilde{S}_N^\sigma[f]$ has a Fourier transform representation in lieu of a point spectrum since it is a compactly supported function. Its Fourier transform, from elementary Fourier properties, is given

[12]We will use the $\sim$ sign in the superscript to denote entities computed using non-harmonic data. For example, if $S_N^\sigma[f]$ denotes the jump function approximation obtained from equispaced Fourier data, the corresponding approximation obtained from non-harmonic Fourier data will be denoted as $\tilde{S}_N^\sigma[f]$.

by

$$\widehat{\tilde{S}_N^\sigma[f]}(\omega) = \hat{f}(\omega) \cdot \widehat{\tilde{C}_N^\sigma}(\omega) \tag{2.56}$$

where the Fourier coefficients of $\tilde{C}_N^\sigma(x)$ are given by

$$\begin{aligned}\widehat{\tilde{C}_N^\sigma}(\omega) &= \mathcal{F}\left\{C_N^\sigma(x) \cdot \Pi\left(\frac{x}{2\pi}\right)\right\}\Big|_\omega \\ &= (\hat{C}_N^\sigma * \text{sinc})(\omega) \\ &= \sum_{|k|\leq N} \hat{C}_N^\sigma(k)\text{sinc}(\omega - k)\end{aligned} \tag{2.57}$$

This relation is particularly useful in computing the Fourier coefficients of the concentration factors designed using the iterative framework of Section 2.4. For the prototypical factors of Table 2.1, however, we may use the more direct relation,

$$\widehat{\tilde{C}_N^\sigma}(\omega) = i \cdot \text{sgn}(\omega) \cdot \sigma\left(\frac{|\omega|}{N}\right) \tag{2.58}$$

Given a set of non-harmonic measurements, $\hat{f}(\omega_k), k = -N, ..., N$, we may use (2.56) to compute the coefficients of its jump function approximation. We are then left with the task of recovering $\tilde{S}_N^\sigma[f]$ from its non-harmonic coefficients. A more exhaustive discussion of the non-harmonic Fourier reconstruction problem is deferred to Chapter 3, while it suffices for the purposes of our current discussion to note that this is a challenging problem. This is because the family of exponentials $\{e^{i\omega_k x}\}, \omega_k \notin \mathbb{Z}$ does not form a basis for functions of practical interest, except under very stringent (and practically unrealistic) circumstances[13]. The quality of the reconstruction also depends on the sampling pattern used. The best results are obtained when the deviation of the acquired samples from equispaced modes is small. As an example, consider the jump function approximation of test function $f_1(x)$, (2.8), using the trigonometric concentration factor and the non-harmonic Fourier modes of Figure 2.24 (a) and Figure 2.24 (b) respectively. We refer to the first sampling scheme as *jittered sampling*, since the non-harmonic modes are obtained by a uniform random jitter of the equispaced modes. The sampling scheme in Figure 2.24 (b) will be referred to as *log sampling* since the spacing between successive samples increases logarithmically. A detailed description of

[13]Kadec's "one-quarter" theorem, [26], allows for reconstruction in the special case that $\sup_k |\omega_k - k| < \frac{1}{4}$.

these sampling schemes is provided in Section 3.1. The jump function approximations of $f_1(x)$ corresponding to these two sampling schemes is plotted in Figure 2.25. A simple variant of the concentration sum (2.3) involving non-harmonic complex exponentials was used to compute these plots. We draw attention to the spurious oscillations present throughout the interval in either plot and the poor localization of the reconstruction in Figure 2.25 (b). It is to be noted that computing edges from the log sampling pattern is particularly challenging due to the sparse sampling of the high frequencies, which are particularly important for edge detection.

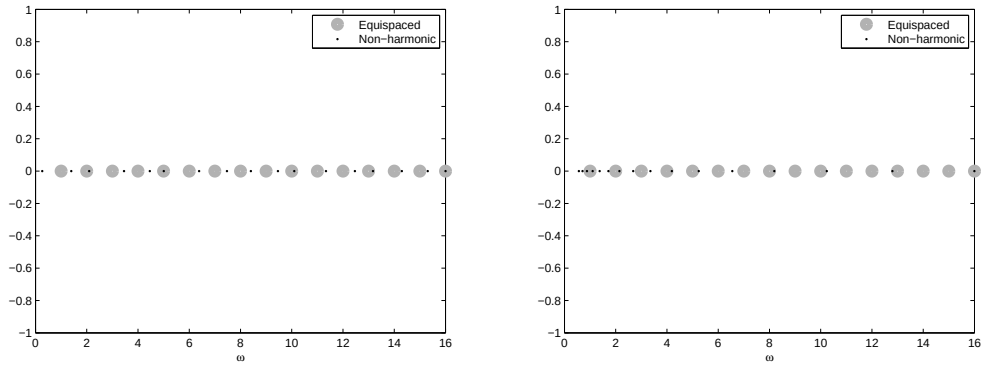

(a) Jittered sampling (b) Log sampling

Fig. 2.24: Non-harmonic sampling distributions in the right half plane, $N = 16$

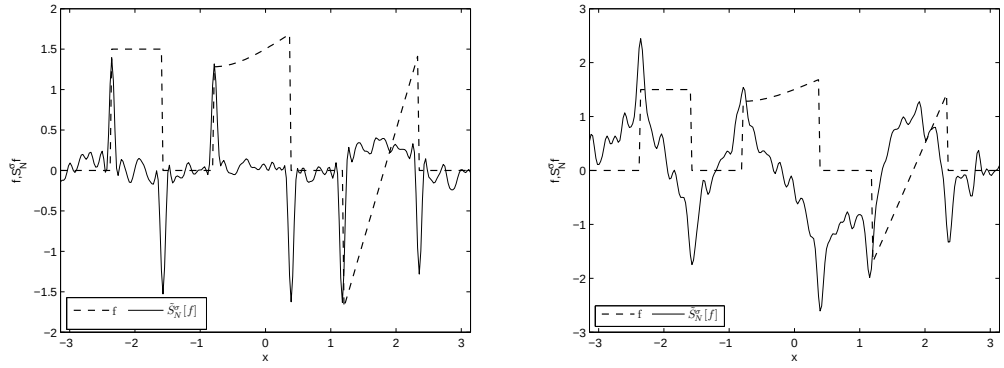

(a) Jittered sampling modes (b) Log sampling modes

Fig. 2.25: Jump approximations from non-harmonic Fourier data, (trigonometric factor, $N = 64$)

2.7.1 Iterative Solutions for Non-harmonic Data

The underlying challenge with non-harmonic expansions is the lack of a basis for accurately reconstructing the jump approximation. Iterative frameworks can be extremely powerful in these circumstances since their formulation only requires an accurate forward model. Casting the concentration method in an iterative framework was initially pursued in [18] with very good results. In this section, we investigate the use of a similar framework for non-harmonic Fourier data. In addition, we incorporate the jump waveform, (Definition 2), in the model formulation, which results in a more accurate representation of the underlying problem. We start with (2.20) and make the assumption that the contribution of the higher-order terms is negligible, i.e.,

$$S_N^\sigma[f](x) \approx ([f] * W_0^{\sigma,N})(x) \tag{2.59}$$

This is an acceptable assumption for functions with small oscillatory content, or when using high-order concentration factors. The concentration method essentially computes a least-squares solution to the above equation. Since jumps are typically sparse in number, we may instead choose to regularize the solution by penalizing its 1-norm[14]. Further, since we are given data in the Fourier domain, we solve the following problem

$$\mathbf{y} = \arg\min_{\mathbf{u}} \|\mathbf{u}\|_1 \quad \text{subject to} \quad \left\| \widehat{\tilde{S}_N^\sigma[f]}(\omega_k) - \mathcal{F}\left\{ \mathbf{u} * W_0^{\sigma,N} \right\}\Big|_{\omega_k} \right\|_2^2 \leq \rho^2 \tag{2.60}$$

where $\{\omega_k\}_{k=-N}^N$ are the non-harmonic measurement modes, ρ^2 is a data-fidelity parameter chosen in accordance with the noise level, and $\mathbf{y} \in \mathbb{R}^M$ is a discrete approximation of the jump function on the M-point equispaced grid

$$x_p = -\pi + \frac{2\pi p}{M}, \quad p = 0, ..., M-1 \tag{2.61}$$

Let $\eta_k, k \in \mathcal{K}$ denote the set of jump locations. We have

$$y_p = \begin{cases} [f](\eta_k) & |\eta_k - x_p| < \frac{2\pi}{M},\ k \in \mathcal{K}, p = 0, ..., M \\ 0 & \text{else} \end{cases} \tag{2.62}$$

[14]Of course, this is a computationally feasible alternative to solving for sparse zero pseudonorm solutions.

Using matrix notation, we may rewrite (2.60) in a form more amenable to computation. Let $\mathbb{F} \in \mathbb{C}^{(2N+1)\times M}$ denote the non-harmonic DFT matrix with entries $\mathbb{F}_{jk} = \frac{1}{M}\exp(-i\omega_j x_k)$, and $\mathbb{W} \in \mathbb{R}^{M\times M}$ denote a Toeplitz matrix containing shifted replicates of the jump waveform, $W_0^{\sigma,N}\left(x - \frac{2\pi p}{M}\right), p = 0, ..., M$, in each of its rows. Let the coefficients of the jump function approximation $\widehat{\tilde{S}_N^{\sigma}[f]}$ be denoted by the vector $\tilde{\mathbf{f}} \in \mathbb{C}^{2N+1}$, with $\tilde{\mathbf{f}} = \hat{f}(\omega_k)\cdot\widehat{\tilde{C}_N^{\sigma}}(\omega_k), k = -N, ..., N$. We may then write

$$\mathbf{y} = \arg\min_{\mathbf{u}} \|\mathbf{u}\|_1 \quad \text{subject to} \quad \left\| \tilde{\mathbf{f}} - \mathbb{F}\cdot\mathbb{W}\cdot\mathbf{u} \right\|_2^2 \leq \rho^2 \tag{2.63}$$

Alternatively, using Lagrange multipliers, we may write

$$\mathbf{y} = \arg\min_{\mathbf{u}} \|\mathbf{u}\|_1 + \lambda\cdot\left\| \tilde{\mathbf{f}} - \mathbb{F}\cdot\mathbb{W}\cdot\mathbf{u} \right\|_2^2 \tag{2.64}$$

where $\lambda > 0$ is a regularization parameter. It is well known that the above problem can be formulated as an SOCP and can be solved using a variety of methods, including barrier methods and interior point methods, [20]. We also note that computational efficiency can be improved by using non-uniform FFT methods, [27, 28], to compute matrix-vector products involving the non-harmonic DFT matrix.

The performance of this method is illustrated in Figure 2.26, where the jump function approximation of $f_1(x)$ obtained by solving the iterative formulation (2.64) is plotted. Results using all three concentration factors from Table 2.1 are plotted on a grid of 257 points and using $101\,(N = 50)$ non-harmonic Fourier modes. Results for the jittered sampling modes are presented in Figure 2.26 (a), while the results for the log sampling modes are presented in Figure 2.26 (c). The corresponding pointwise errors to the true jump function are plotted in a logarithmic scale in Figure 2.26 (b) and Figure 2.26 (d) respectively. The reader is encouraged to compare these plots with those of Figure 2.25. The significantly greater accuracy of the iterative solution is immediately obvious. The pointwise errors reveal vanishing responses in the smooth regions and the correct identification of jump locations. The jump values, however, are incorrectly identified. We believe that this is related to the selection of the regularization parameter and is earmarked for future investigations. This is ultimately inconsequential, since jump values may be accurately estimated by the evaluation of the concentration sum (2.3) at these jump locations. As with Figure 2.25, the relative

Table 2.3: Regularization parameter values for the jump function approximation of $f_1(x)$

	Trigonometric factor	1^{st}**-order polynomial factor**	6^{th}**-order exponential factor**
Jittered sampling modes	45	100	100
Log sampling modes	32.5	70	100

quality of the plot for the log sampling modes is poorer, with false activations in the linear region and a few false positives in the vicinity of true jumps. A table of regularization values used in the generation of these plots is provided for reference in Table 2.3.

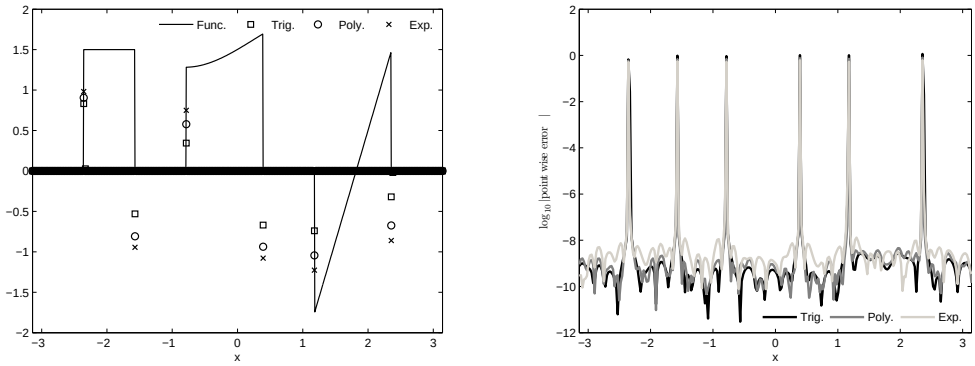

(a) Jump function approximation, Jittered sampling

(b) Log pointwise error, Jittered sampling

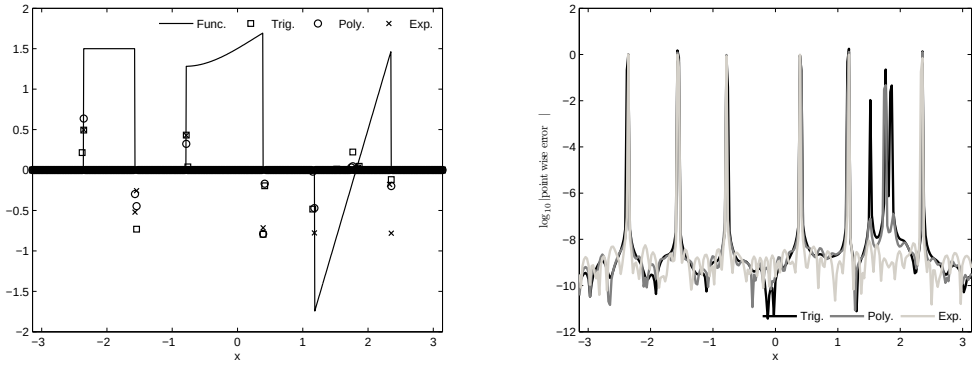

(c) Jump function approximation, Log sampling

(d) Log pointwise error, Log sampling

Fig. 2.26: Jump function approximations from non-harmonic Fourier data using the iterative formulation, ($N = 50$)

CHAPTER 3

RECONSTRUCTION FROM NON-HARMONIC FOURIER DATA

The reconstruction of functions from Fourier spectral data is a well studied problem in mathematical literature. In particular, given the first $2N+1$ Fourier series coefficients of a periodic function f, it is well known that the partial Fourier sum

$$S_N f(x) := \sum_{|k|\leq N} f(x)e^{ikx}, \quad \hat{f}(k) := \frac{1}{2\pi}\int_{-\pi}^{\pi} f(x)e^{-ikx}dx$$

converges exponentially quickly to f. This rate of convergence, however, only holds for smooth functions, and piecewise analyticity results in the familiar Gibbs phenomenon, [8]. Additional post-processing may optionally be performed to recover spectral accuracy in such reconstructions. Nevertheless, reconstruction from *harmonic* spectral data is well known and widely utilized in several areas of science and engineering.

The reconstruction of functions from non-harmonic spectral data has attracted relatively lesser attention. This is a problem of some significance, since it finds application in fields such as MR imaging and SAR imaging. For example, in MR imaging, the MR scanner acquires samples of the Fourier transform of the specimen being imaged, and we are faced with the task of recovering the underlying image. Certain practical constraints such as scanning hardware limitations, and the necessity to acquire data with decreased susceptibility to motion and aliasing artifacts have resulted in the introduction of non-harmonic scan trajectories, i.e., the acquisition of Fourier samples along non-Cartesian trajectories. The reconstruction of functions from non-harmonic Fourier data is a challenging problem because the non-harmonic exponentials which correspond to the acquired data points rarely constitute a basis for functions in $L^2(-\pi,\pi)$. Additional complications result when reconstructing piecewise-analytic functions, and with the acquisition of data samples with non-uniform sampling density.

This chapter addresses the reconstruction of compactly supported functions from non-uniform samples of their Fourier transform. We start by looking at the consequences of acquiring non-harmonic data. In particular, the properties of the kernel described by non-uniform modes is investigated in Section 3.2. Section 3.4 briefly summarizes existing reconstruction methods, including the convolutional gridding algorithm. Error bounds for regridded coefficients and the resulting reconstruction are derived. The relation between reconstruction error and sampling density is also

investigated. To mitigate the effects of non-harmonic acquisition, Section3.6 investigates the use of spectral re-projection methods. Results and error bounds for such reconstructions are provided, with simulations showing greater reconstruction accuracy and/or reduced points per wave requirements when compared to traditional reconstruction procedures. Finally, some preliminary results from incorporating edge locations and values in the reconstruction scheme are summarized in Section 3.7.

3.1 Notation and Sampling Schemes

Let $f \in L^2(\mathbb{R})$ be supported in $[-\pi, \pi)$. It is common for f to be piecewise-defined since real-world functions often contain jump discontinuities. Given a finite number of non-harmonic[1] Fourier coefficients,

$$\hat{f}(\omega_k) := \frac{1}{2\pi} \int_{-\pi}^{\pi} f(x) e^{-i\omega_k x} dx, \quad k = -N, ..., N, \quad \omega_k \text{ not necessarily in } \mathbb{Z} \tag{3.1}$$

our objective will be to recover f. For the purposes of this discussion, we will consider reconstruction from the following sampling schemes

1. Jittered Sampling:

$$\omega_k = k \pm \tau_k, \quad \tau_k \sim U[0, \theta],\ k = -M, -(M-1), ..., M \tag{3.2}$$

   Here $U[a, b]$ denotes a uniform distribution on the interval $[a, b]$. The τ_k's are independent, identically distributed (i.i.d.) random variables, and represent a uniform jitter about the equispaced nodes with a maximal jitter of θ. Further, both positive and negative jitters are equiprobable, with the sign of jitter at each node being independent of the sign of jitter at any other node. Figure 3.1 (a) illustrates the jittered sampling scheme.

2. Log Sampling: Samples in Fourier space are acquired at logarithmic intervals, with more samples acquired in lower frequencies. If ω_k are the nodes at which measurements are acquired, $|\omega_k|$ is (deterministically) logarithmically distributed between 10^{-v} and N, with $v > 0$ and $2N + 1$ being the total number of samples. Motivation for this sampling scheme

[1] The terms non-harmonic and non-uniform will be used interchangeably in this discussion.

can be found in MRI, where typical data acquisition schemes oversample the low frequencies of k-space while undersampling the high frequencies. Figure 3.1 (b) illustrates the log sampling scheme.

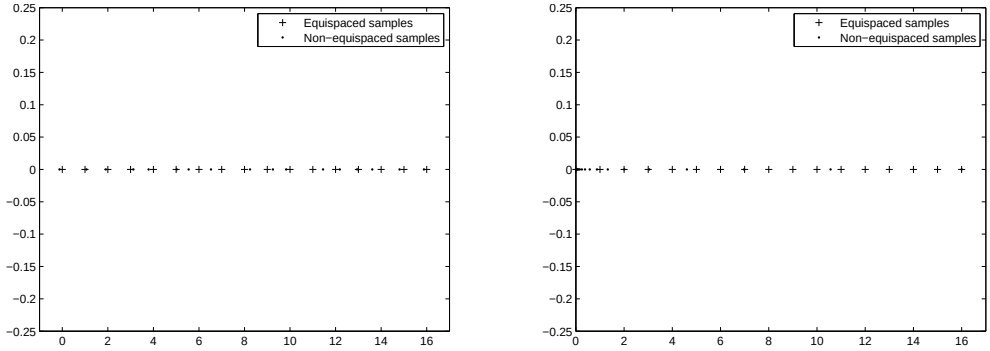

(a) Jittered sampling, $M = 16, \theta = 0.5$ (b) Log sampling, $M = 16, v = 1.5$

Fig. 3.1: Sampling schemes plotted in the right half plane

3.2 Consequences of Acquiring Non-uniform Spectral Data

The reconstruction challenge with non-harmonic spectral data can be understood by looking at the properties of the kernel described by these non-harmonic modes. As a first attempt, consider the reconstruction using the non-harmonic Fourier partial sum

$$P_N f(x) = \sum_{|k| \leq N} \hat{f}(\omega_k) e^{i\omega_k x} \tag{3.3}$$

It is trivial to show that this reconstruction can be written as

$$P_N f(x) = (f * A_N)(x), \quad A_N(\eta) = \sum_{|k| \leq N} e^{i\omega_k \eta} \tag{3.4}$$

where $A_N(\eta)$ defines the non-harmonic kernel. Insight into the reconstruction problem may be obtained by comparing this kernel to the Dirichlet kernel from harmonic Fourier reconstruction. The non-harmonic kernel is plotted in Figure 3.2 for the two sampling schemes and different values of N. One observes the significant deviation from the usual Dirichlet kernel, with distinctive features including non-diminishing sidelobes and/or a large mainlobe. These features contribute to artifacts and/or poor localization in the resulting reconstruction, as illustrated in Figure 3.3 where the reconstruction of test functions $f_1(x)$ and $f_2(x)$ are plotted.

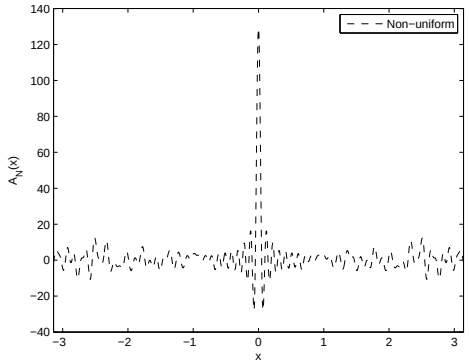

(a) Jittered sampling, $N = 64$

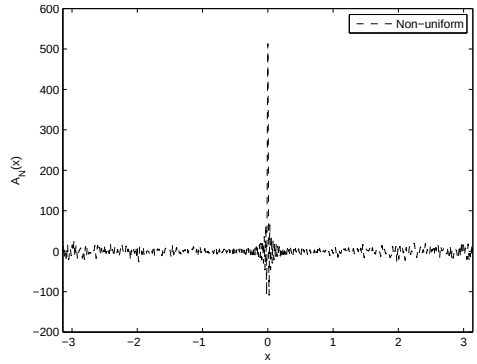

(b) Jittered sampling, $N = 256$

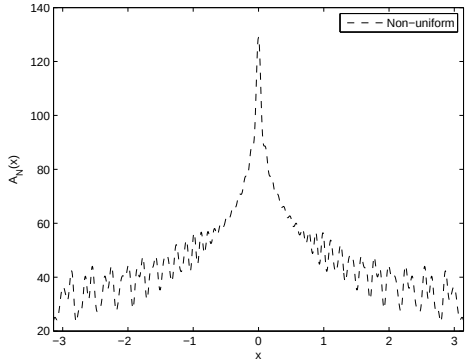

(c) Log sampling, $N = 64$

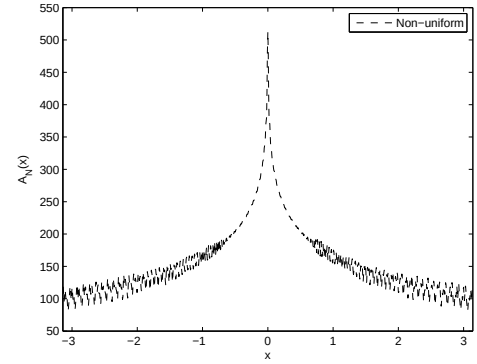

(d) Log sampling, $N = 256$

Fig. 3.2: Comparison of the non-harmonic kernel and the Dirichlet kernel using jittered sampling and log sampling

$$f_1(x) = \cos(6x) \tag{3.5}$$

$$f_2(x) = \begin{cases} \frac{3}{2} & -\frac{3\pi}{4} \le x < -\frac{\pi}{2} \\ \frac{7}{4} - \frac{x}{2} + \sin(x - \frac{1}{4}) & -\frac{\pi}{4} \le x < \frac{\pi}{8} \\ \frac{11}{4}x - 5 & \frac{3\pi}{8} \le x < -\frac{3\pi}{4} \\ 0 & \text{else} \end{cases} \tag{3.6}$$

The reconstruction challenges are independent of the degree of smoothness of the function; however, presence of jumps can accentuate artifacts in the reconstruction. The poor accuracy is also not caused by lack of resolution. Both Figure 3.2 and Figure 3.4 illustrate that the underlying cause is the non-harmonic acquisition of spectral data. For example, Figure 3.4 plots the 2-norm and infinity-norm errors for the reconstruction of $f_2(x)$ from jittered Fourier samples ($\theta = 2.5$).

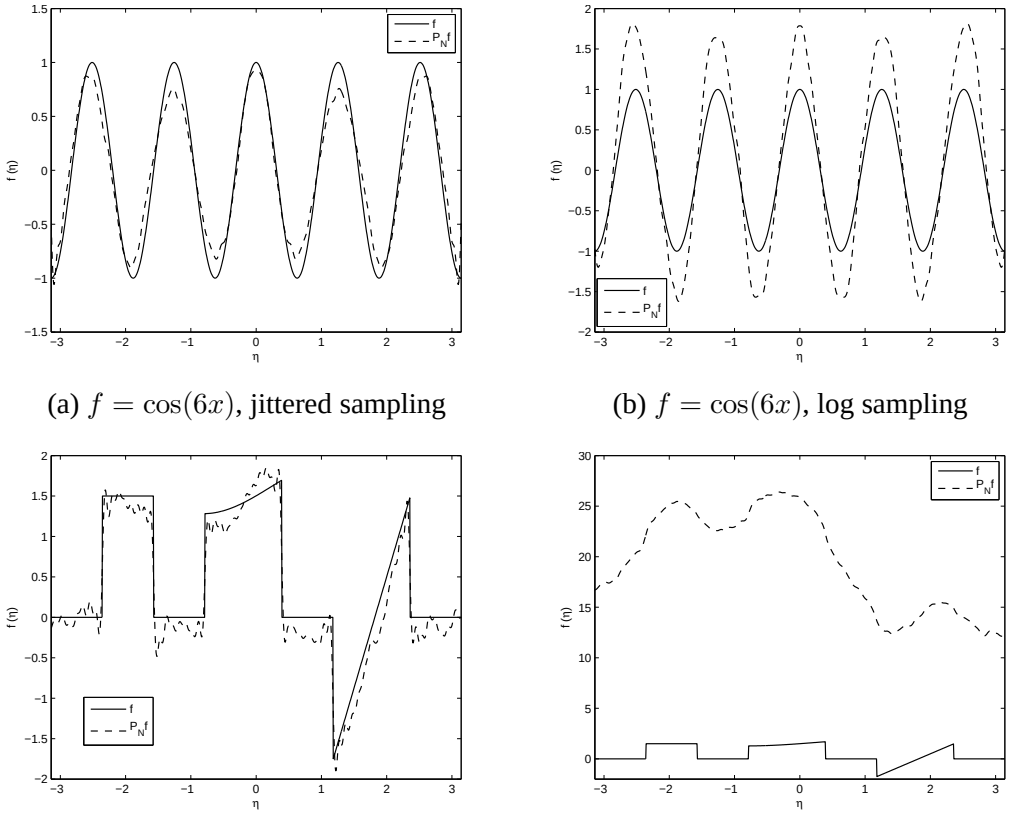

(a) $f = \cos(6x)$, jittered sampling

(b) $f = \cos(6x)$, log sampling

(c) Test function $f_2(x)$, jittered sampling

(d) Test function $f_2(x)$, log sampling

Fig. 3.3: Reconstruction using the non-harmonic partial sum, $N = 64$

The reconstruction grid in each case is of size 2049. Note the random variations in the error curves (for sufficiently large N) which manifest from the sampling pattern.

3.3 Summary of Related Work

Literature on the non-harmonic Fourier reconstruction problem can be traced back to the works of Paley, Wiener and Levinson, [29], on non-harmonic Fourier series. These results were refined over the years with the most notable work being the "$1/4$"-theorem of Kadec, [26]. The interested reader is referred to [30] for a comprehensive overview and discussion of the subject. Frame theoretic approaches to non-harmonic reconstruction have also been pursued. A notable collection of related literature with applications to medical imaging can be found in [31]. Two methods deserve special mention for their popularity in medical imaging – convolutional gridding, [5], and uniform re-sampling, [6]. Gridding is an extremely popular reconstruction procedure for non-harmonic data,

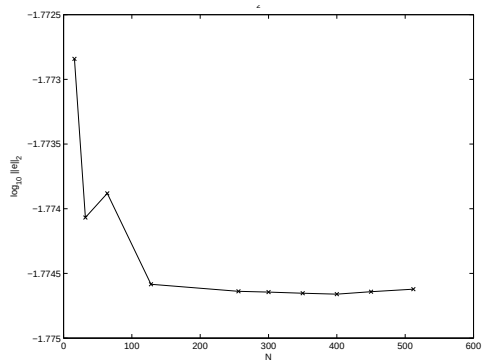

(a) $\log_{10} \|f - P_N f\|_2$

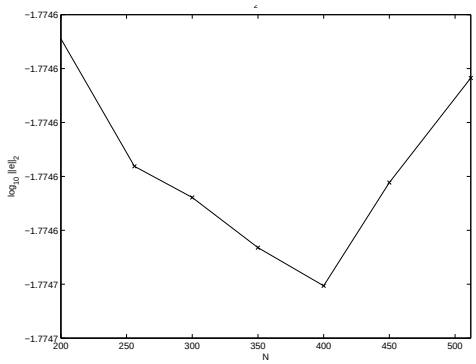

(b) $\log_{10} \|f - P_N f\|_2$ – Expanded view

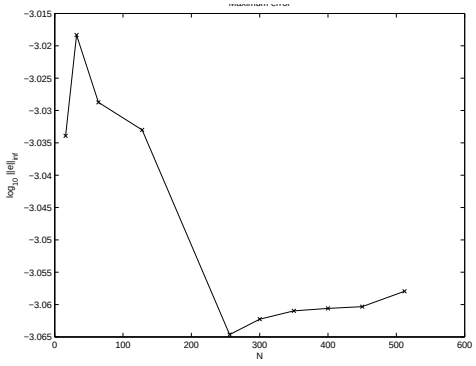

(c) $\log_{10} \|f - P_N f\|_\infty$

Fig. 3.4: Reconstruction error $\|f - P_N f\|$, for test function $f_2(x)$ as a function of N using jittered sampling

with applications spanning radio astronomy and image processing among several others. Both gridding and uniform re-sampling work by mapping the non-harmonic measurements to uniform modes and subsequent processing using standard Fourier methods. There are also a large class of iterative methods, which find successful application in a variety of problem settings. Each work differs in the type of regularization imposed, such as total variation or l_1-type methods. A representative reference for this class of methods can be found in [32]. Recent developments in the theory of compressive sensing have also resulted in problem formulations and applications to MR imaging. The reader is referred to [33] for an overview of the theory and computational tools of the same.

3.4 CONVOLUTIONAL GRIDDING

Most conventional reconstruction procedures for non-harmonic Fourier data involve mapping the non-harmonic modes to harmonic coefficients, followed by standard Fourier reconstruction. We describe below the most popular of such methods, convolutional gridding, [5].

Gridding refers to the process of moving from the non-uniform modes to a uniform grid. When this process is accomplished by evaluating a convolution integral (or an approximation of the convolutional integral), the method is called convolutional gridding. Let $\hat{f}$ denote the Fourier transform of f. For compactly-supported functions, this is a smooth function of unbounded support. Let us denote by $\hat{\phi}$ a smooth function whose properties are chosen to minimize reconstruction error and cost. It is common to refer to this function as a window function; its choice will be discussed shortly. The convolution of these two functions, $\hat{g}(\omega) = (\hat{f} * \hat{\phi})(\omega)$ remains smooth and may evaluated at equispaced grid points. The gridding process involves computing a discrete approximation to this convolution integral

$$\hat{\tilde{g}}(k) = \sum_{p \in \mathcal{P}} \alpha_p \hat{f}(\omega_p) \hat{\phi}(k - \omega_p) \tag{3.7}$$

Here, α_k are known as density compensation factors (DCFs) and may be thought of weights necessary to evaluate a non-uniform trapezoidal quadrature rule. Several methods of computing these DCFs exist such as [34], but for ease of analysis, we restrict our immediate attention to the simple weights

$$\alpha_k = \omega_{k+1} - \omega_k \tag{3.8}$$

The measurement set $\mathcal{P}$ necessary to evaluate the sum depends on the properties of $\hat{\phi}$ and will be discussed shortly. Nevertheless, once we obtain the coefficients $\hat{\tilde{g}}(k)$, we may compute a Fourier approximation $S_N \tilde{g}(x)$ from which we divide out the window function ϕ to obtain our approximation to f. These steps are formally enumerated in Algorithm 2.

3.4.1 The Window Function ϕ

The requirements on the gridding or window function ϕ are:

1. The choice of ϕ should minimize the computational cost of evaluating (3.7).
2. The choice of ϕ should reduce artifacts due to aliasing in the reconstruction.
3. $\phi \neq 0$ in the reconstruction interval $[-\pi, \pi)$.

Algorithm 2 The convolutional gridding algorithm

Given: $\hat{f}$ at the Non-equispaced measurement nodes ω_k

Choose: Truncation parameter q

Interpolating function ϕ

1. Interpolation to equispaced nodes:
   $$\hat{\tilde{g}}(k) = \sum_{m \text{ st. } |k-\omega_m| \leq q} \alpha_m \hat{f}(\omega_m)\hat{\phi}(k-\omega_m), \quad k = -N, ..., N$$
2. Standard FFT computation:
   $$S_N\tilde{g}(x) = \sum_{k=-N}^{N} \hat{\tilde{g}}(\omega_k)e^{ikx}$$
3. Compensation for use of the interpolating function:
   $$\tilde{f}(x) = \frac{\tilde{g}(x)}{\phi(x)}$$

One way to ensure computational efficiency is by constraining $\hat{\phi}$ to be of finite support. Similarly, aliasing may be prevented by requiring ϕ to be supported in $[-\pi, \pi)$. However, these are contradictory requirements since a function cannot be compactly supported in both physical and spectral domains. Practical window functions therefore attempt to be *essentially bandlimited*; i.e.,

$$\begin{aligned} \hat{\phi}(\omega) &\approx 0 \qquad |\omega| > q,\ q \in \mathbb{R}, \text{small} \\ \phi(x) &\approx 0 \qquad |x| > \pi \\ \text{with } \phi(x) &\neq 0 \quad x \in [-\pi, \pi] \end{aligned} \tag{3.9}$$

Popular window functions include the Gaussian and Kaiser Bessel functions. The window function is in addition to and independent of filtering, which is always applied since the underlying functions are generally piecewise-smooth and can contain noise.

The gridding process can be computed using one of several non-uniform FFT (NUFFT) software packages, [27, 28]. These packages implement all steps of convolutional gridding except for density compensation. Hence, by pre-multiplying the non-harmonic Fourier measurements by appropriate DCFs and then computing the NUFFT, we may obtain fast function reconstructions. Representative examples of convolutional gridding reconstructions from log-sampled spectral data are provided in

Figure 3.5.

$$f_3(x) = \begin{cases} \sin(3x) & x < 0 \\ e^{-2x} & x \geq 0 \end{cases} \tag{3.10}$$

Figure 3.5(a) shows the gridding reconstruction of test function $f_3(x)$ given by (3.10). Figure 3.5(b) shows the reconstruction of a cross-section of a brain scan obtained from the McGill BrainWeb database, [35, 36, 37, 38, 39]. The brain scan was a T1 scan of a normal brain of 1mm slice thickness with no noise and RF field non-uniformities. These reconstructions were post-processed using a fourth-order exponential filter. We notice the significantly improved quality over the plots in Figure 3.3. The filtering operation, however, introduces some smearing artifacts and the non-harmonic acquisition manifests as some ringing artifacts near the ends of the domain.

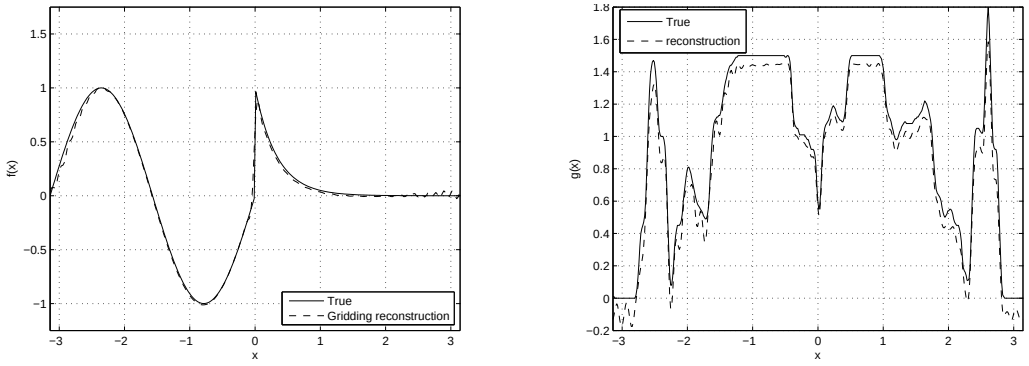

(a) Reconstruction of test function $f_3(x)$, $N = 128$, jittered sampling

(b) Reconstruction of a brain cross-section from log spectral samples

Fig. 3.5: Reconstruction using convolutional gridding, processed using a fourth-order exponential filter

3.4.2 Error in Convolutional Gridding Reconstruction

We now provide error bounds for the gridding process and the resulting reconstruction.

Definition 4. (Minimum sampling density d_k) *Let the* q-vicinity *of* k *(*$q > 0$*) be the set*

$$\{\mathcal{P} = \omega \text{ st. } |k - \omega| \leq q,\ k \in \mathbb{Z}, \omega, q \in \mathbb{R}\}$$

The q-vicinity *refers to the region around any equispaced coefficient. Let* Δ_k *be the maximum distance between sampling points in the* q*-vicinity of* k*; i.e.,* $\Delta_k = \max_{p \in \mathcal{P}} |\omega_{p+1} - \omega_p|$*. In this* q-

vicinity, we define the minimum sample "density" d_k *to be the number of sample points per unit interval; i.e.,* $d_k = \frac{1}{\Delta_k}$.

Theorem 3.4.1. (Convolutional gridding error) *Let* ω_k *denote the non-uniformly sampled modes and* $\hat{f}(\omega_k)$ *the Fourier transform measurements at these modes. Let* $\hat{\phi}$ *denote the gridding window function and* $\hat{g} = \hat{f} * \hat{\phi}$ *denote the true gridding coefficients. Let* $\hat{\tilde{g}}$ *denote the approximate gridding coefficients obtained by using a finite sum and the DCFs in (3.8). Let* q *be the window function truncation parameter; i.e.,* $\hat{\phi}(\omega) = 0$ *for* $|\omega| > q$. *Let* d_k *be the minimum sample density in the* q*-vicinity of* k. *Then, the gridding error, defined as* $e(k) = \hat{g}(k) - \hat{\tilde{g}}(k)$ *at mode* k *is bounded by* $|e(k)| \leq C\frac{1}{d_k^2}$, $k = -N, ..., N$, *for some positive constant* C.

Proof. The error in each of the equispaced Fourier coefficients after gridding is given by

$$\hat{g}(k) - \hat{\tilde{g}}(k) = \int_{-\infty}^{\infty} \hat{f}(\omega)\hat{\phi}(k-\omega)d\omega - \sum_{p \text{ st. } |k-\omega_p| \leq q} \alpha_p \hat{f}(\omega_p)\hat{\phi}(k-\omega_p) \tag{3.11}$$

Let us evaluate the error e_p in approximating the integral in the interval (ω_p, ω_{p+1}). Substituting (3.8) for the density compensation factors α_p and using the trapezoidal quadrature rule, we have

$$e_p = \int_{\omega_p}^{\omega_{p+1}} \hat{f}(\omega)\hat{\phi}(k-\omega)d\omega - \frac{|\omega_{p+1} - \omega_p|}{2}\left(\hat{f}(\omega_p)\hat{\phi}(k-\omega_p) + \hat{f}(\omega_{p+1})\hat{\phi}(k-\omega_{p+1})\right)$$

The trapezoidal quadrature rule, [40], yields

$$e_p \leq \frac{|\omega_{p+1} - \omega_p|^3 v_p}{12} \tag{3.12}$$

where

$$\begin{aligned} v_p &= \left.\frac{d^2\left(\hat{f}(\omega)\hat{\phi}(k-\omega)\right)}{d\omega^2}\right|_{\omega=\zeta}, \quad \zeta \in [\omega_p, \omega_{p+1}] \\ &= \left.\hat{f}(\omega)\hat{\phi}^{(2)}(k-\omega)\right|_{\omega=\zeta} - 2\left.\hat{f}^{(1)}(\omega)\hat{\phi}^{(1)}(k-\omega)\right|_{\omega=\zeta} + \left.\hat{f}^{(2)}(\omega)\hat{\phi}(k-\omega)\right|_{\omega=\zeta} \end{aligned}$$

We note that $\hat{f}, \hat{\phi}$ and their derivatives are finite in the interval (ω_p, ω_{p+1}); hence v_p is bounded. In particular, we may set $\max_{p \in \mathcal{P}} |v_p|$ to some positive constant A.

The total gridding error is the error over all intervals of integration; i.e.,

$$e(k) = \sum_p e_p \approx \sum_{p \text{ st. } |k-\omega_p| \leq q} e_p$$

$$
\begin{aligned}
|e(k)| = \left|\hat{g}(k) - \hat{\tilde{g}}(k)\right| &\leq \sum_{p \text{ st. } |k-\omega_p| \leq q} \frac{|\omega_{p+1} - \omega_p|^3 \ |v_p|}{12} \\
&\leq \frac{A}{12} \sum_{p \text{ st. } |k-\omega_p| \leq q} |\omega_{p+1} - \omega_p|^3 \\
&= \frac{A}{12} \sum_{p \text{ st. } |k-\omega_p| \leq q} |\omega_{p+1} - \omega_p| \cdot |\omega_{p+1} - \omega_p|^2 \\
&\leq \frac{A}{12} \Delta_k^2 \sum_{p \text{ st. } |k-\omega_p| \leq q} |\omega_{p+1} - \omega_p| \\
&\lesssim 2q \frac{A}{12} \frac{1}{d_k^2} \\
&= C \frac{1}{d_k^2}, \quad C = 2q \frac{A}{12}
\end{aligned} \tag{3.13}
$$

□

This error bound is plotted in Figure 3.6. Figure 3.6(a) plots the true[2] error[3] and the error bound for reconstructing $f_2(x)$ from jittered samples while Figure 3.6(b) plots the error and the error bound for reconstructing $f_3(x)$ from log samples. In each case, a value of $N = 128$ was used along with a Gaussian window function with truncation parameter $q = 12$ to satisfy (3.9).

The physical-space reconstruction error can now be written as

$$
\begin{aligned}
e(x) = f(x) - \frac{S_N \tilde{g}(x)}{\phi(x)} \approx g(x) - S_N \tilde{g}(x) &= g(x) - S_N g(x) + S_N g(x) - S_N \tilde{g}(x) \\
&= \sum_{|k|>N} \hat{g}(k) e^{ikx} + \sum_{|k| \leq N} \left(\hat{g}(k) - \hat{\tilde{g}}(k)\right) e^{ikx}
\end{aligned} \tag{3.14}
$$

The first component is the standard Fourier truncation error. Since we are primarily interested in piecewise-smooth functions, $S_N g$ suffers from the Gibbs phenomenon. The maximum error occurs in the vicinity of a jump and is approximately 1.09 of the jump value. There is also a reduced order

[2]The "true" coefficients were computed by approximating the convolution using an equispaced sum on a fine grid (> 2000 points).

[3]There is numerical evidence to suggest that the constant C scales as the magnitude of $\hat{g}(k)$. This behaviour will be investigated in future work. The true error plots in Figure 3.6 are plotted normalized by $|\hat{g}(k)|$.

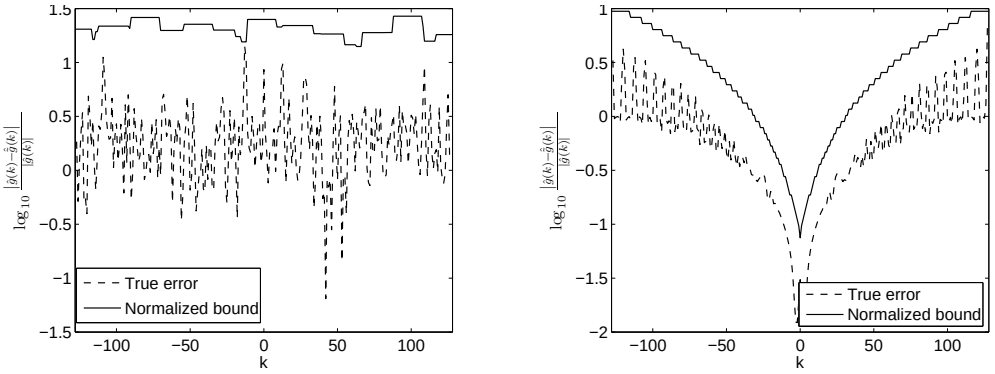

(a) Jittered sampling, bound for $f_2(x)$ (b) Log sampling, bound for $f_3(x)$

Fig. 3.6: Gridding error and the associated error bound

of convergence with $\|g - S_N g\|_2 = \mathcal{O}\left(N^{-1/2}\right)$. The second term in (3.14) is the gridding error.

$$\begin{aligned} |S_N g(x) - S_N \tilde{g}(x)| &= \left| \sum_{|k|\leq N} \left(\hat{g}(k) - \hat{\tilde{g}}(k) \right) e^{ikx} \right| \\ &\leq \sum_{|k|\leq N} \left| \hat{g}(k) - \hat{\tilde{g}}(k) \right| \\ &\leq C \sum_{|k|\leq N} \frac{1}{d_k^2} \end{aligned} \tag{3.15}$$

Let $H(d_k, N) := \sum_{|k|\leq N} \frac{1}{d_k^2}$. This term is plotted as a function of N for the log sampling pattern in Figure 3.7. We observe that it increases rapidly with N, indicating that the error in the reconstruction would increase at a similar rate.

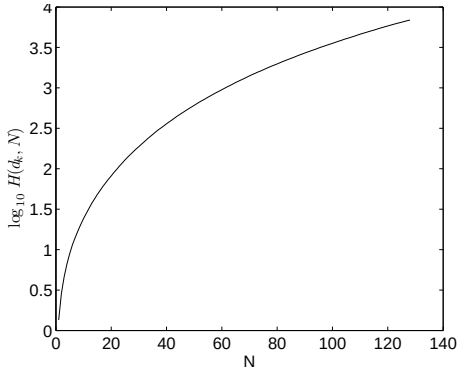

Fig. 3.7: Plot of $H(d_k, N)$ as a function of N for log sampling

It is important to note that the two error components in (3.15) have differing characteristics,

with the gridding error increasing with N and the Fourier truncation error decreasing with N. In sampling schemes such as log sampling, where the sampling density decreases significantly at the high modes, the gridding error dominates to the point where it is no longer advantageous to use all the regridded coefficients in the reconstruction.

3.5 An Alternate Reconstruction Procedure – Uniform Re-sampling

A more intuitive understanding of the reconstruction problem may be attained by studying the uniform re-sampling algorithm. This algorithm, introduced in [6, 41], provides a least-squares solution to the reconstruction problem. It is a two-step reconstruction method involving

1. Recovery of Fourier coefficients at equispaced nodes.
2. Partial Fourier sum reconstruction using the recovered equispaced modes.

Of course, the final step may be accelerated by application of the FFT algorithm. The algorithm has its roots in the application of the Whittaker-Kotelnikov-Shannon sampling theorem. For $f \in L^2(-\pi, \pi)$, application of the sampling theorem in Fourier space allows us to relate the harmonic Fourier modes to the non-harmonic measurements. In particular, we have

$$\hat{f}(\omega) = \sum_{k=-\infty}^{\infty} \hat{f}(k)\text{sinc}(\omega - k), \quad \omega \in \mathbb{R} \tag{3.16}$$

Since this is essentially a convolution with shifted sinc interpolants, we may write a truncated version of the above relation as a linear system of equations. Let $y = \hat{f}(m)$, $m = -N, ..., N$, denote the equispaced Fourier coefficients we seek. If $b = \hat{f}(\omega_k)$, $k = 0, ..., M-1$, are the set of measurements and A is the matrix with elements $a_{ij} = \text{sinc}(\omega_i - j), i = 0, ..., M-1$, $j = -N, ..., N$, we may write

$$Ay \approx b \tag{3.17}$$

We compute a least-squares minimum norm solution $\tilde{y}$ of the form

$$\tilde{y} = A^{+} b, \tag{3.18}$$

where A^{+} is the Moore-Penrose pseudoinverse computed using the singular value decomposition (SVD). Invariably, A has a high condition number, necessitating use of regularization in computing the solution. Results in this dissertation use the truncated SVD, implemented using Matlab's pinv

command. The regularization threshold for the pinv command was chosen as per the discrete Picard condition, [42, Chapter 4]. The final approximation of f is obtained by using a Fourier partial sum.

Reconstruction of test function $f_2(x)$ (3.6) using this method from its log spectral samples is illustrated in Figure 3.8. Figure 3.8a plots the high-mode recovered equispaced Fourier coefficients, while Figure 3.8b plots the corresponding error in recovering these coefficients. The function reconstruction is shown in Figure 3.8c. The recovered equispaced coefficients are observed to show a similar error trend as that of convolutional gridding. Similar arguments as in Section 3.4 may be made with regard to the number of "good" or accurate coefficients and their use in function reconstruction. For completeness, we plot the recovery of $f_3(x)$ from its jittered Fourier coefficients in

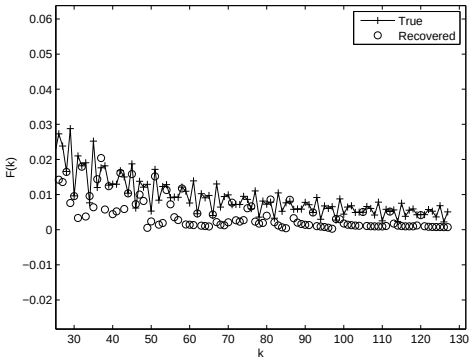

(a) Recovered high-mode equispaced Fourier coefficients

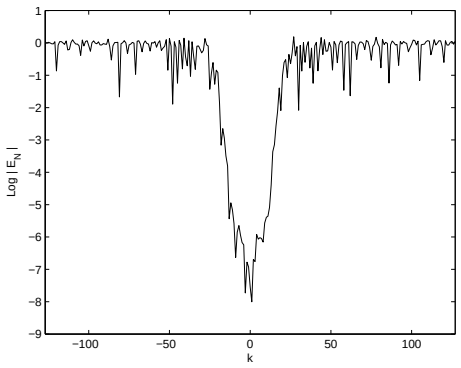

(b) Error in the interpolated coefficients

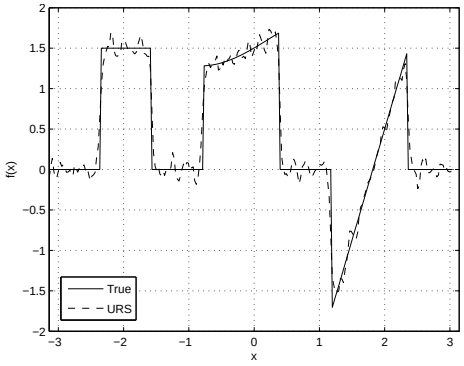

(c) Reconstructed function

Fig. 3.8: Reconstruction using URS, $N = 128$

Figure 3.9. Here, we find that the reconstruction accuracy is much better than the previous example.

Table 3.1: Dependence of the sinc matrix condition number on the sampling pattern (Jittered sampling, $N = 128$)

Maximal jitter, θ	0.1	0.5	1	5	10
Condition number	1.371	27.806	1.690×10^3	1.137×10^8	1.875×10^9

The Gibbs artifact remains and filtering or other techniques are required to mitigate this problem, but the error due to non-uniform spectral sampling is small.

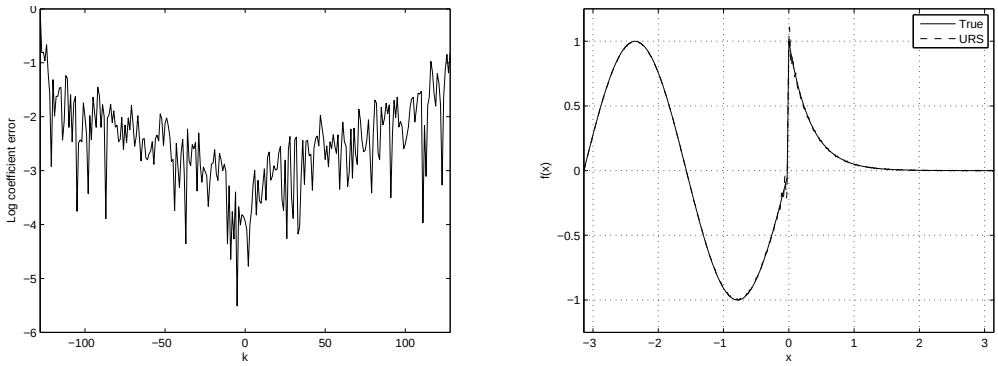

(a) Error in the interpolated coefficients (b) Function reconstruction

Fig. 3.9: Reconstruction of $f_3(x)$ using URS, $N = 128$

It is obvious from the two examples that the quality of reconstruction depends on the sampling pattern. The sampling density of the acquired coefficients is reflected in the condition number of the sinc matrix. Jittered sampling results in a well conditioned matrix which can be inverted easily. Log sampling, however, results in a large condition number ($\mathcal{O}(10^{17})$), with the result being that the system of equations cannot be solved accurately. The artifacts seen in Figure 3.8 are a direct consequence of this. The singular values of the system matrices for the two sampling schemes are shown in Figure 3.10. Further corroboration of this dependence of the condition number on sampling density is provided in Table 3.1, where the condition number of the sinc matrix for jittered sampling is tabulated for different values of the jitter (parameter θ (in 3.2)). It can be seen that as the jitter increases, i.e., the samples get more irregular, the condition number increases.

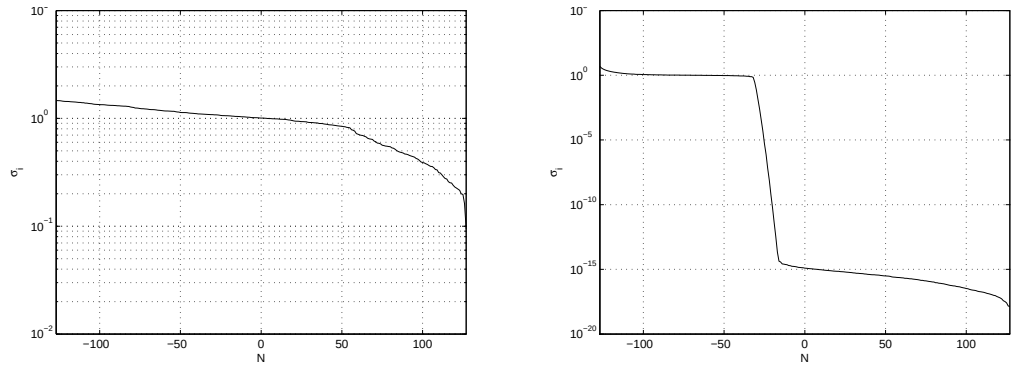

(a) Jittered sampling (b) Log sampling

Fig. 3.10: Plot of singular values of the sinc system matrix, $N = 128$

3.6 SPECTRAL RE-PROJECTION

It is well known that spectral approximations of piecewise-smooth functions, such as the brain scan cross-section of Figure 3.5(b) suffer from the Gibbs phenomenon. This manifests as non-uniform convergence at a local level and reduced order of convergence at a global level. The non-uniform convergence leads to oscillations in the vicinity of discontinuities (or smearing in filtered reconstructions), which can cause loss of detail in MR scans. In addition to affecting the diagnostic quality of the scan, these artifacts also affect the accuracy of subsequent image processing tasks such as segmentation, edge detection and feature recognition. The reduced order of convergence in the reconstruction necessitates acquiring a large number of k-space samples, resulting in increased scan time. Other consequences include increased patient discomfort and motion artifacts in the scan. Spectral re-projection has previously been applied (for example, [43]) in the context of post-processing MR scans to improve resolution and segmentation performance. Here, we discuss the utility of spectral re-projection in the non-harmonic reconstruction problem.

A detailed explanation of spectral re-projection is beyond the scope of this dissertation. Instead, we restrict ourselves to a brief summary, while pointing the interested reader to [8] for a more comprehensive treatment of the topic. The cause of the Gibbs phenomenon can be traced to using global data in the reconstruction. Fourier coefficients are representative of the function values over the entire domain. Consequently, the reconstruction of a discontinuous function at any point in the

domain uses information from either side of a discontinuity, leading to loss of localization and non-physical oscillations. Spectral re-projection schemes, by contrast, require reconstruction in each smooth interval. While the task of identifying intervals of smoothness is a challenging problem, we have found the concentration method of edge detection (Chapter 2) to be adequate in identifying jump information.

The key to spectral re-projection is to reconstruct using an alternate, specifically chosen basis known as a *Gibbs complementary* basis. This basis is orthonormal, supports exponential reconstruction accuracy, and has the property that high modes of the Fourier basis have exponentially small projections on low modes of the reconstruction basis. Let $\{\psi_l\}$, $l = 0, 1, ...$ be such an orthonormal basis with respect to the weight w. The m-term approximation of a function f using $\{\psi_l\}$ is given by

$$P_m f(x) = \sum_{l=0}^{m} c_l \psi_l(x), \quad c_l = \frac{\langle f, \psi_l \rangle_w}{\|\psi_l\|_w^2} \tag{3.19}$$

The method obtains its name from the fact that f can be replaced by its $(2N + 1)$-term Fourier expansion f_N in the inner product; i.e., the reconstruction is computed by projecting the Fourier data to the Gibbs-complementary basis. The significance of this scheme is that a poorly converging $(2N + 1)$-term Fourier expansion contains sufficient information to recover exponentially convergent reconstructions in the new basis. It is shown in [8] that the Gegenbauer polynomials form a Gibbs-complementary basis for Fourier data.

In reconstructing functions from non-harmonic spectral samples such as the log sampling scheme, we require similar properties in the reconstruction scheme. In Theorem 3.4.1, it was shown that the regridded coefficients at a particular mode have an error inversely proportional to the square of the sampling density. Therefore, sampling schemes such as log sampling, where the sampling density decreases at the high frequencies, result in large errors in the high-mode coefficients. The spectral re-projection of these high-mode Fourier coefficients onto a Gibbs-complementary basis allows us to exponentially damp the error in the spectral re-projection reconstruction. Moreover, the rapid convergence of the reconstruction allows us to start with a much smaller set of coefficients.

Let us assume that we use Gegenbauer polynomials $C_l^{\lambda}(x)$ for reconstruction[4]. We will assume

[4]See [8] for basic properties of $C_l^{\lambda}(x)$ and admissibility requirements for λ and m in (3.19).

that smooth intervals in the function can be identified without error. The reconstruction process is summarized in Algorithm 3.

Algorithm 3 Spectral re-projection for non-uniform Fourier data

---

Given: $\hat{f}$ at the non-equispaced measurement nodes ω_k

Choose: Gegenbuer reconstruction parameters m, λ

1. Perform convolutional gridding (Algorithm 2) to obtain coefficients on the equispaced grid ($\hat{\tilde{g}}$).
2. Identify smooth regions in g using methods such as the concentration method of edge detection (Chapter 2).
3. In each smooth interval:
   a) Compute Gegenbauer expansion coefficients z_l.

$$z_l = \langle S_N \tilde{g}, C_l^\lambda \rangle_w = \frac{1}{h_l^\lambda} \int_{-1}^{1} (1-\eta^2)^{\lambda-1/2} C_l^\lambda(\eta) \sum_{|k|\le N} \hat{\tilde{g}}(k) e^{i\pi k\eta} d\eta$$

   b) Function reconstruction using the Gegenbauer partial sum $P_m S_N \tilde{g}$.

$$P_m S_N \tilde{g}(x) = \sum_{l=0}^{m} z_l C_l^\lambda(x)$$

3.6.1 Error Analysis for Spectral Re-projection Reconstructions

If we assume that the compensation step where we divide out the window function in (3.9) can be performed without error; i.e., $\|f - P_m S_N \tilde{f}\| \approx \|g - P_m S_N \tilde{g}\|$, we have:

$$\|g - P_m S_N \tilde{g}\| \le \|g - P_m g\| + \|P_m g - P_m S_N g\| + \|P_m S_N g - P_m S_N \tilde{g}\| \tag{3.20}$$

The first term is known as the *regularization error*. The classical result, [8], is that for $\lambda = \gamma m$, $\gamma > 0$, constant,

$$\|g - P_m g\|_\infty \le A \zeta_R^m \tag{3.21}$$

where A is some positive constant and

$$\zeta_R = \frac{(1+2\gamma)^{1+2\gamma}}{2^{1+2\gamma}\, \rho\, \gamma^\gamma\, (1+\gamma)^{1+\gamma}}$$

For $\rho \geq 1$, ζ_R can be shown to be less than one. The second term in (3.20) is the *truncation error* and classical results (e.g., [8]) show that for $\lambda = \alpha N, m = \beta N$, α, β constants, this error can be bounded as

$$\|P_m g - P_m S_N g\|_\infty = \|P_m \left(g - S_N g\right)\|_\infty \leq A \zeta_T^N \tag{3.22}$$

where A grows at most as a fixed degree polynomial of N and

$$\zeta_T = \frac{(\beta + 2\alpha)^{\beta+2\alpha}}{(2\pi)^\alpha \, \alpha^\alpha \, \beta^\beta}$$

For carefully chosen λ, m ($\alpha = \beta \leq \frac{2\pi}{27}$), we have $\zeta_T < 1$. The third term in (3.20) is due to gridding. For ease of analysis, we shall assume we are given a Fourier partial expansion in the interval $[-1, 1]$. This result can, however, be generalized to any other interval by suitable scaling. Solving for the gridding error, we have,

$$\|P_m S_N g - P_m S_N \tilde{g}\|_\infty = \|P_m \left(S_N g - S_N \tilde{g}\right)\|_\infty$$

We note that $S_N g(x) - S_N \tilde{g}(x) = \sum_{|k| \leq N} \left(\hat{g}(k) - \hat{\tilde{g}}(k)\right) e^{i\pi k \eta}$. Substituting this in (3.19) and using Gegenbauer polynomials for the Gibbs complementary basis, we obtain

$$\begin{aligned}
&\|P_m S_N g - P_m S_N \tilde{g}\|_\infty = \\
&\qquad \left\| \sum_{l=0}^{m} \frac{C_l^\lambda(x)}{h_l^\lambda} \int_{-1}^{1} (1-\eta^2)^{\lambda - 1/2} C_l^\lambda(\eta) \sum_{|k| \leq N} \left(\hat{g}(k) - \hat{\tilde{g}}(k)\right) e^{i\pi k \eta} d\eta \right\|_\infty \\
&\qquad \leq \max_{-1 \leq x \leq 1} \left| \sum_{l=0}^{m} \frac{C_l^\lambda(x)}{h_l^\lambda} \int_{-1}^{1} (1-\eta^2)^{\lambda - 1/2} C_l^\lambda(\eta) \sum_{|k| \leq N} \left(\hat{g}(k) - \hat{\tilde{g}}(k)\right) e^{i\pi k \eta} d\eta \right| \\
&\qquad \leq \sum_{l=0}^{m} \sum_{|k| \leq N} \left| \frac{C_l^\lambda(1)}{h_l^\lambda} \int_{-1}^{1} (1-\eta^2)^{\lambda - 1/2} C_l^\lambda(\eta) \left(\hat{g}(k) - \hat{\tilde{g}}(k)\right) e^{i\pi k \eta} d\eta \right| \\
&\qquad \leq C \sum_{l=0}^{m} \sum_{|k| \leq N} \frac{1}{d_k^2} \left| \frac{C_l^\lambda(1)}{h_l^\lambda} \int_{-1}^{1} (1-\eta^2)^{\lambda - 1/2} C_l^\lambda(\eta) e^{i\pi k \eta} d\eta \right|
\end{aligned} \tag{3.23}$$

where C is some positive constant. Note that we have used $\max_{x \in [-1,1]} C_l^\lambda(x) = C_l^\lambda(\pm 1)$ in the penultimate step. The integral in the above expression has been evaluated in closed form in [44]. This result states that

$$\frac{1}{h_l^\lambda} \int_{-1}^{1} (1-\eta^2)^{\lambda - 1/2} C_l^\lambda(\eta) e^{i\pi k \eta} d\eta = \begin{cases} \Gamma(\lambda) \left(\frac{2}{\pi k}\right)^\lambda i^l (l + \lambda) J_{l+\lambda}(\pi k) & k \neq 0 \\ \delta_{0l} & k = 0 \end{cases} \tag{3.24}$$

where $\Gamma(\cdot)$ is the gamma function and $J_v(x)$ is the v^{th}-order Bessel function of the first kind. Since $|J_v(x)| \leq 1, \forall x, v > 0$, we have for $k \neq 0$

$$\left|\frac{C_l^\lambda(1)}{h_l^\lambda}\int_{-1}^{1}(1-\eta^2)^{\lambda-1/2}C_l^\lambda(\eta)e^{i\pi k\eta}d\eta\right| \leq C_l^\lambda(1)\Gamma(\lambda)(l+\lambda)\left(\frac{2}{\pi|k|}\right)^\lambda$$
$$= \frac{\Gamma(\lambda)(l+\lambda)\Gamma(l+2\lambda)}{l!\Gamma(2\lambda)}\left(\frac{2}{\pi|k|}\right)^\lambda \tag{3.25}$$

where the second step is obtained for substituting for $C_l^\lambda(1)$. Summing over all k we obtain

$$\sum_{|k|\leq N}\frac{1}{d_k^2}\left|\frac{C_l^\lambda(1)}{h_l^\lambda}\int_{-1}^{1}(1-\eta^2)^{\lambda-1/2}C_l^\lambda(\eta)e^{i\pi k\eta}d\eta\right| \leq$$
$$\delta_{0l}\frac{1}{d_0^2} + \frac{\Gamma(l+2\lambda)\Gamma(\lambda)(l+\lambda)}{l!\Gamma(2\lambda)}\sum_{0<|k|\leq N}\frac{1}{d_k^2}\left(\frac{2}{\pi|k|}\right)^\lambda \tag{3.26}$$

Define $H(\omega_k, N, \lambda) := \sum_{0<|k|\leq N}\frac{1}{d_k^2}\left(\frac{1}{|k|}\right)^\lambda$. This term is plotted in Figure 3.11 as a function of N for different values of λ. A direct comparison with the Figure 3.7 (standard Fourier reconstruction) reveals the reduced impact on the error as a function of N. Inequality (3.26) therefore becomes

$$\sum_{|k|\leq N}\left|\frac{C_l^\lambda(1)}{h_l^\lambda}\int_{-1}^{1}(1-\eta^2)^{\lambda-1/2}C_l^\lambda(\eta)e^{ik\pi\eta}d\eta\right|$$
$$\leq \frac{\delta_{0l}}{d_0^2} + \frac{\Gamma(l+2\lambda)\Gamma(\lambda)(l+\lambda)}{l!\Gamma(2\lambda)}\left(\frac{2}{\pi}\right)^\lambda H(\omega_k, N, \lambda) \tag{3.27}$$

Substituting in (3.23), we obtain

$$\|P_m S_N g - P_m S_N \tilde{g}\|_\infty \leq C\sum_{l=0}^{m}\left(\frac{\delta_{0l}}{d_0^2} + \frac{\Gamma(l+2\lambda)\Gamma(\lambda)(l+\lambda)}{l!\Gamma(2\lambda)}\left(\frac{2}{\pi}\right)^\lambda H(\omega_k, N, \lambda)\right)$$
$$= C\left(\frac{1}{d_0^2} + \frac{\Gamma(\lambda)}{\Gamma(2\lambda)}\left(\frac{2}{\pi}\right)^\lambda H(\omega_k, N, \lambda)\sum_{l=1}^{m}\frac{\Gamma(l+2\lambda)(l+\lambda)}{l!}\right)$$
$$= C\left(\frac{1}{d_0^2} + H(\omega_k, N, \lambda)\rho(m, \lambda)\right), \quad \rho(m,\lambda) = \frac{\Gamma(\lambda)}{\Gamma(2\lambda)}\left(\frac{2}{\pi}\right)^\lambda\sum_{l=1}^{m}\frac{\Gamma(l+2\lambda)(l+\lambda)}{l!}$$
$$\lesssim C\, H(\omega_k, N, \lambda)\, \rho(m, \lambda) \tag{3.28}$$

where the final step is obtained by assuming that $\frac{1}{d_0^2} \lesssim H(\omega_k, N, \lambda)\, \rho(m, \lambda)$. This is true for most problems since the low frequencies contain a significant portion of the signal energy and are therefore well sampled; i.e., $\frac{1}{d_0^2}$ is usually small.

A cursory inspection will reveal that this bound is very conservative[5]. In particular, $\rho(m, \lambda)$ grows rapidly with m, λ. However, our primary objective here is to investigate the dependence of the reconstruction error on sampling density. While the error does increase with increase in N, a comparison with standard Fourier reconstruction error (3.15) reveals that this increase is significantly damped by the term $H(\omega_k, N, \lambda)$. Although $H(\omega_k, N, \lambda)$ is an increasing function in N, Figure 3.11 shows that the rate of increase for large N is small.

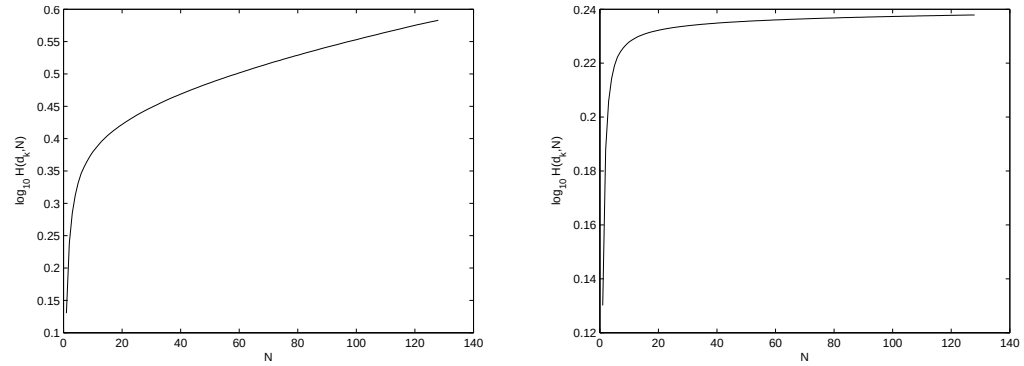

(a) $\lambda = 2$

(b) $\lambda = 3$

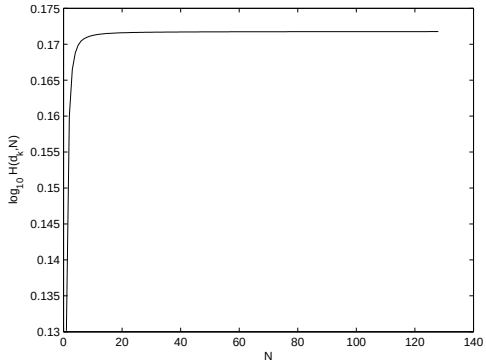

(c) $\lambda = 4$

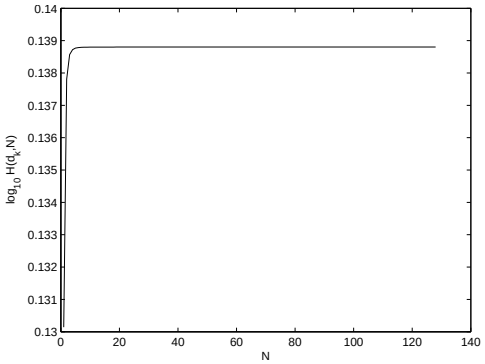

(d) $\lambda = 6$

Fig. 3.11: Plots of $H(d_k, N, \lambda)$ as a function of N for log sampling

To illustrate the effectiveness of spectral re-projection, consider the plots in Figure 3.12, where

[5]The bound in (3.25) is too conservative; the presence of the Bessel function and the imaginary term is bound to result in cancellations.

test function $f_4(x)$ given by (3.29) is reconstructed from its log spectral samples.

$$f_4(x) = \begin{cases} -1 & -2.5 \leq x < -\frac{\pi}{4} \\ e^{-x} & 0 \leq x < \frac{\pi}{4} \\ 1 + \frac{\cos(5x)}{2} & 1.25 \leq x < 2.75 \\ 0 & \text{else} \end{cases} \tag{3.29}$$

Convolutional gridding was used to obtain the regridded coefficients. For reference, second-order exponentially filtered reconstructions are plotted. Figures 3.12(a) and (b) plot the filtered Fourier and spectral re-projection (using Gegenbauer polynomials) reconstructions respectively while Figure 3.12(c) plots the physical-space log reconstruction errors. Equivalent error performance is observed for the Gegenbauer reconstruction with no Gibbs or filtering artifacts. Additionally, the Gegenbauer reconstruction was computed using 85 coefficients, as opposed to the 256 coefficients required for the filtered Fourier reconstruction. The vastly improved performance of the Gegenbauer reconstruction can be explained by the decay rate of the expansion coefficients. Figure 3.13 plots the magnitude of the regridded Fourier coefficients alongside the Gegenbauer expansion coefficients. The Gegenbauer expansion is computed using a five term partial sum, and the several orders of magnitude reduction in the value of the coefficients indicates a significantly accelerated decay rate over the standard Fourier case.

The performance of spectral re-projection is independent of the regridding method used. For example, similar results can be obtained when using the URS algorithm to obtain equispaced coefficients. Figure 3.14(a) and (b) plot the 2-norm and maximum norm errors respectively as a function of N for the reconstruction of test function $f_4(x)$ (3.29). Log spectral samples were used with equispaced coefficients recovered using the URS algorithm. We note that the error curve flattens out after a certain value of N, indicating that the high-mode coefficients do not contribute to the reconstruction. The first to flatten out and indeed the plot with the least error is the Gegenbauer curve, indicating that there are strong advantages to using spectral re-projection methods for reconstruction from sampling schemes similar to log sampling.

It is to be mentioned that no effort was made to optimize the values of m and λ. These were chosen proportional to the length of the reconstruction interval with m, λ taking a minimum value of

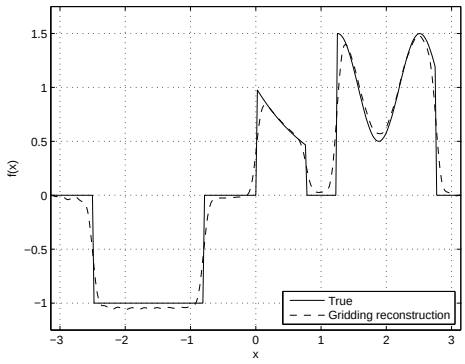

(a) Second-order exponentially filtered Fourier reconstruction, 256 coefficients

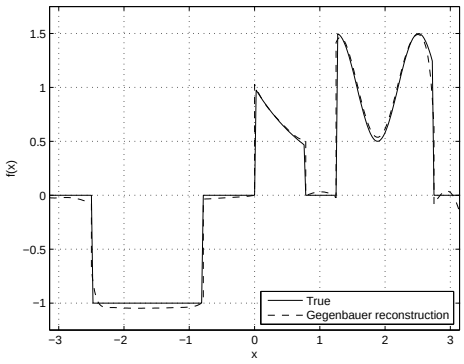

(b) Gegenbauer reconstruction, 85 coefficients

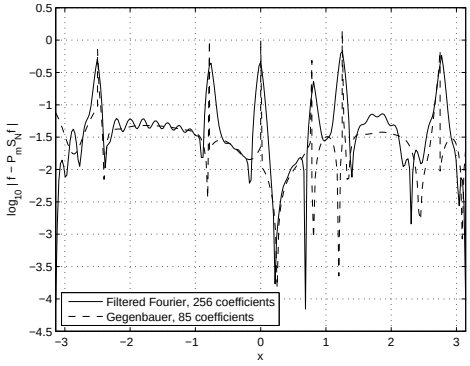

(c) Physical space log reconstruction errors

Fig. 3.12: Comparison of filtered Fourier and spectral re-projection reconstructions, log sampling scheme

two and capped to a maximum of six and four respectively. It was noted in the course of simulations that the reconstruction is more sensitive to parameter selection than re-projection with the harmonic Fourier coefficients.

3.7 Incorporating Edge Information

The non-harmonic Fourier reconstruction problem is just one example of a challenging, ill-posed inverse problem. Methods such as uniform re-sampling and convolutional gridding attempt to solve this problem in a least-squares framework. This is successful, as we have seen in Section 3.5, for cases where the sampling modes do not deviate significantly from the equispaced samples (e.g., jittered sampling with small jitter). In other cases, however, we see significant artifacts and loss of resolution. The spectral re-projection reconstructions of Section 3.6, on the other hand, use edge

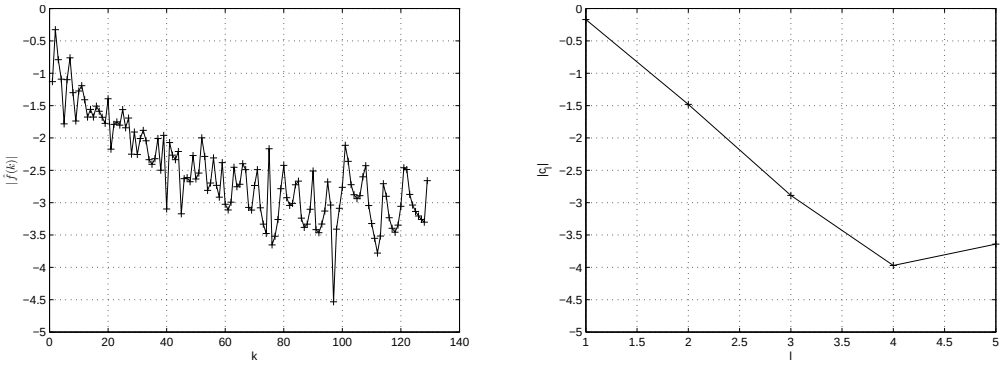

(a) Regridded Fourier coefficients (b) Gegenbauer expansion coefficients

Fig. 3.13: Comparison of decay rates of Fourier and Gegenbauer expansion coefficients

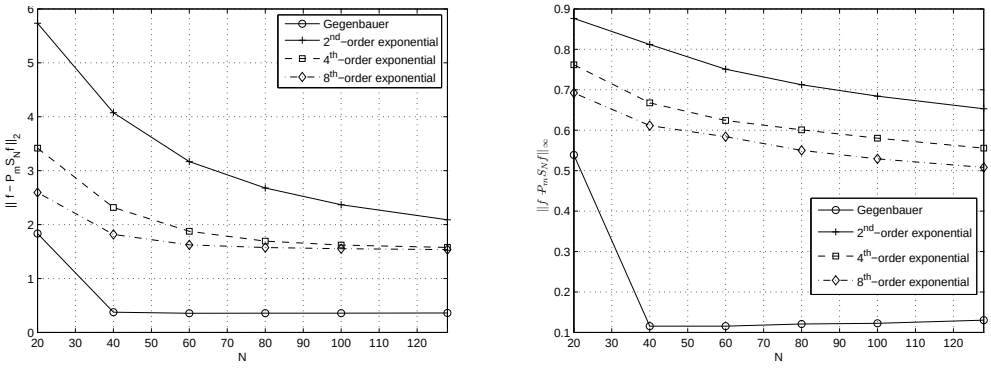

(a) 2-norm error (b) Maximum norm error

Fig. 3.14: Reconstruction error as a function of N (Test function $f_4(x)$, log sampling)

detection schemes to enforce the location of jump discontinuities in the reconstruction. This leads to improved reconstruction quality and resolution. We now investigate the use of not only the jump locations, but also jump values in the reconstruction.

From (2.14), we have

$$\hat{f}(k) = \frac{1}{2\pi}\frac{[f](\eta)}{ik}e^{-ik\eta} + \mathcal{O}\left(\frac{1}{|k|^2}\right), \quad k \neq 0 \tag{3.30}$$

Given the jump locations, $\eta_k, k \in \mathcal{K}$ and the corresponding jump valsues, $[f](\eta_k), k \in \mathcal{K}$, we may approximate the equispaced Fourier modes of the function using the above expression. We note that the approximation quality improves as k increases. This is particularly useful in the case of sam-

pling schemes such as log sampling, because the high mode recovered coefficients show significant error when employing traditional reconstruction schemes. In the preliminary results presented below, we use jump information obtained using the concentration method. The results below use only jump information to synthesis accurate high mode coefficients. However, we may also use jump information from higher-order derivatives to improve the accuracy of the reconstruction. Information about jumps in each of the derivatives of the function will yield upto an order of magnitude improvement in the reconstruction accuracy. Note that methods similar to the concentration edge detection scheme have to be used to obtain information about the jumps in derivatives of the function.

Preliminary numerical results using this procedure are shown in Figures 3.15–3.16. We start with a simple example and $41(N = 20)$ harmonic Fourier coefficients of test function $f_1(x)$. Using the concentration edge detection method, the trigonometric concentration factor and the matched filter detector of Section 2.5, we compute the jump locations and values. The jump detection is plotted in Figure 3.15 (a). Using this edge information and (3.30), we synthesize $216(N = 128)$ high frequency coefficients. The reconstruction using these synthesized coefficients is plotted in Figure 3.15 (b). Note the significantly improved reconstruction quality. Physical space log reconstruction errors and filtered reconstructions are also plotted for reference.

This procedure is particularly useful in the case of non-harmonic Fourier reconstruction. We provide representative results below of the reconstruction of test functions $f_4(x)$, (3.29), and $f_5(x)$, (3.31), from their log spectral samples using edge information. We acquire the first $61(N_c = 30)$ low frequency coefficients out of a $257(N = 128)$ point log spectral sampling series, and recover 71 equispaced coefficients using the uniform re-sampling method. Using these coefficients, we apply the concentration edge detection procedure to identify jump locations and values. This jump information is used to synthesize 452 (to provide a total of 513 modes) additional high-frequency coefficients. Reconstruction plots using these coefficients for the two test functions are provided in Figure 3.16 (a) and (b) respectively. Both plots have been processed using fourth order exponential filters. Note the significantly enhanced accuracy when using edge information. We may optionally choose to perform spectral re-projection using the synthesized coefficients. An illustrative result using Gegenbauer polynomials with parameter choices $m = \lambda = 4$ is shown in Figure 3.16 (c) with

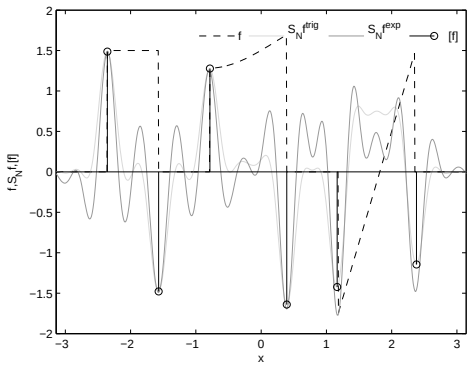

(a) Edge Detection, $N = 20$

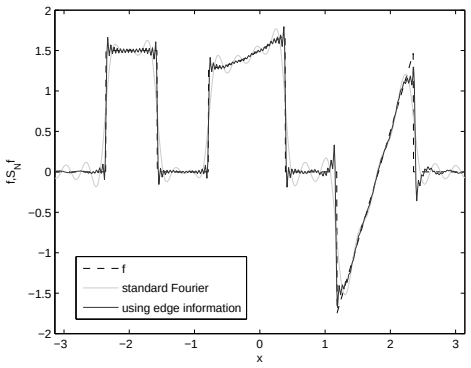

(b) Function reconstruction

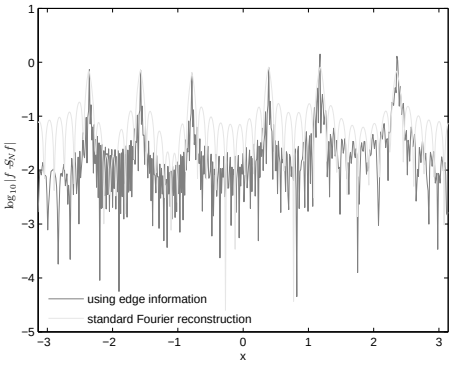

(c) Physical space log error

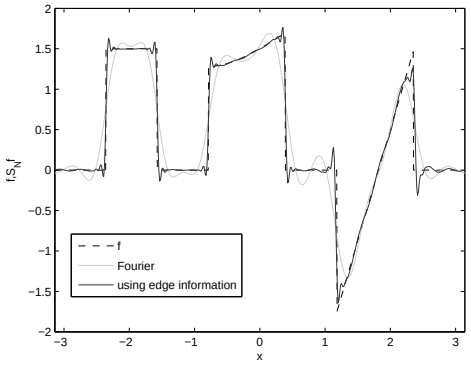

(d) Filtered reconstructions (8^{th}-order exponential)

Fig. 3.15: Reconstruction using edge information

an associated error plot in Figure 3.16 (d).

$$f_5(x) = \begin{cases} \sin(x) & -\pi \leq x < -\frac{\pi}{2} \\ -\cos\left(\frac{3x}{2}\right) & -\frac{\pi}{2} < x < \frac{\pi}{4} \\ \pi - x & \frac{\pi}{4} < x \leq \pi \end{cases} \tag{3.31}$$

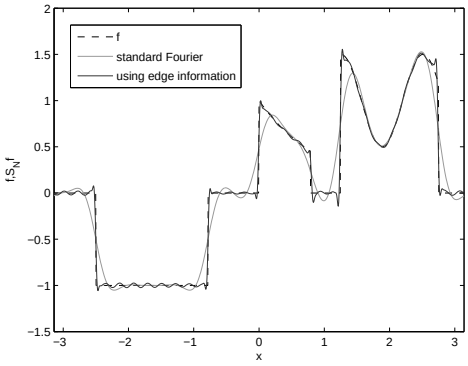

(a) Reconstruction of $f_4(x)$

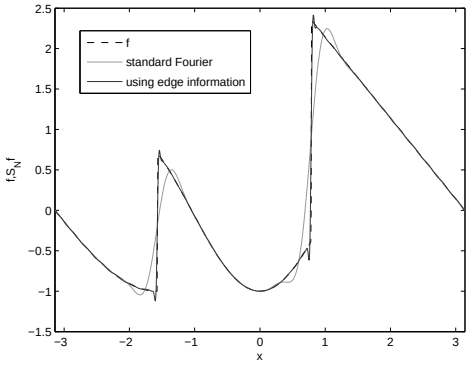

(b) Reconstruction of $f_5(x)$

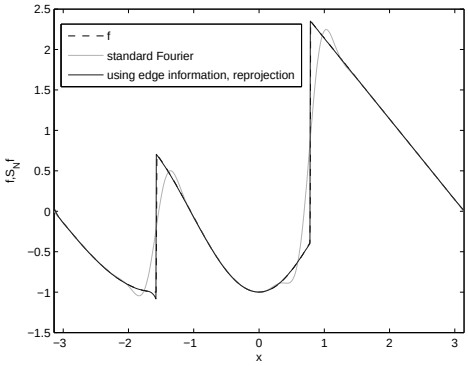

(c) Reconstruction of $f_5(x)$, with re-projection

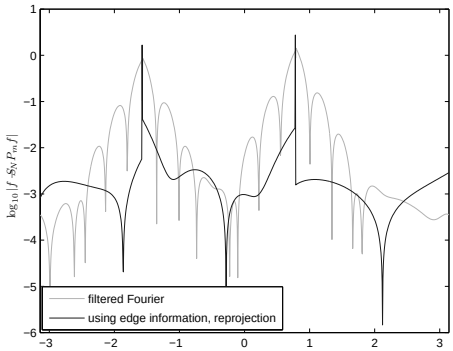

(d) Log error in the reconstruction

Fig. 3.16: Reconstruction from non-harmonic Fourier data using edge information

CHAPTER 4

POINT-SPREAD FUNCTION ESTIMATION IN DE-BLURRING PROBLEMS

Piecewise-smooth functions are distinct in that there is an intricate interplay between their spectral expansions and the presence of local features such as jump discontinuities. The use of such local information in the accurate reconstruction of functions has been discussed in Chapter 3. In this chapter, we describe another example of this interplay between local jump features and global expansions, and exploit this relationship in the estimation of point spread functions (psfs) in de-blurring problems.

The acquisition of blurred data is often unavoidable in several signal processing tasks, since real world measurements are typically distorted by underlying physical phenomena, instrumentation processes and other artifacts. For example, imaging systems have a finite resolution and consequently capture point sources as blobs or blurs. Similar distortions occur when an object is in motion and the process of image acquisition is slow. A large class of such distortions can be explained using the convolutional blurring model. Let f denote the undistorted signal and h denote the blur or psf. If $\mathbf{n}$ denotes stochastic noise, the convolutional blurring model (Figure 4.1) states that the distorted signal can be written in its most general form as

$$\mathbf{g} = f * h + \mathbf{n} \tag{4.1}$$

The recovery of the undistorted signal f or an approximation to f is, of course, of significant

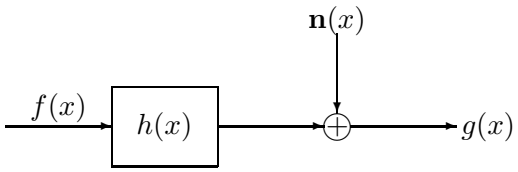

Fig. 4.1: Convolutional blurring model

importance. The methods to accomplish this are both numerous and diverse, with the best results obtained when an accurate estimate of the psf is available. This chapter discusses the estimation of psfs from one-dimensional piecewise-smooth functions subject to convolutional blurring. The principal tool employed is edge detection and we assume, as in the previous chapters, that we start with a finite number of Fourier spectral measurements.

The rest of this chapter is organized as follows: Section 4.1 summarizes the principle behind this estimation scheme. Application of the concentration edge detector on the blurred Fourier data is shown to yield scaled and shifted replicates of the psf at each of the jump locations. Some comments on the effect of noise and choice of the concentration factor on the psf estimate are made in Section 4.2. Finally, examples of the method applied to Gaussian and out-of-focus blurs are discussed in Section 4.3.

4.1 PRINCIPLE – PSF ESTIMATION USING CONCENTRATION EDGE DETECTION

We assume that we are given a finite number of equispaced[1] Fourier coefficients of a piecewise-smooth function subject to convolutional blurring. Further, we will assume (for simplicity of analysis) that corrupting noise is additive, white complex Gaussian. Moreover, for the accurate estimation of psfs, we require that jumps in the underlying function be well separated, i.e., distance between successive jumps $\gg \frac{\log N}{N}$. The psfs are estimated to within a scale factor in amplitude using this formulation.

This PSF estimation scheme exploits the linearity of the convolutional blurring process and that of the concentration edge detection method. Let us start with the convolutional blurring expression in (4.1). By applying a linear edge detector T, such as the convolutional edge detector of the concentration edge detection method (Chapter 2), we obtain

$$\begin{aligned}
\mathbf{S}_{\mathbf{N}}^{\sigma}[\mathbf{g}] &= T\left(f * h + \mathbf{n}\right) \\
&= \left(f * h + \mathbf{n}\right) * C_N^{\sigma} \\
&= f * h * C_N^{\sigma} + \mathbf{n} * C_N^{\sigma} \\
&= \left(f * C_N^{\sigma}\right) * h + \mathbf{n} * C_N^{\sigma} \\
&= S_N^{\sigma}[f] * h + \tilde{\mathbf{n}}, \quad \tilde{\mathbf{n}} = \mathbf{n} * C_N^{\sigma} \\
&\approx [f] * h + \tilde{\mathbf{n}}
\end{aligned} \tag{4.2}$$

Therefore, the application of the concentration (and in general, a linear) edge detector on the blurred

[1] If non-harmonic measurements are collected, equispaced coefficients may be obtained by methods such as gridding or re-sampling (Chapter 3).

data allows us to observe shifted and scaled replicates of the psf. The output takes the form

$$T[\hat{g}] = \sum_j \alpha_j h(x - \eta_j) + \tilde{\mathbf{n}}(x) \tag{4.3}$$

where α_j denote the jump heights and η_j denote the jump locations. The noise component $\tilde{\mathbf{n}}$ usually has specific characteristics depending on the initial noise distribution and the form of the edge detector. If the jump discontinuities are sufficiently separated, we may devise a suitable method to estimate the parameters of the PSF. The principle is illustrated in Figures 4.2 and 4.3. In either case, the first plot illustrates the true function, $f_1(x)$, (4.4), and the blurred observation. Starting with $2N+1$ Fourier coefficients of this blurred observation, the result of concentration jump approximation (using he trigonometric concentration factor) is plotted in the second plot. For comparison, the true blur is also plotted. Both the jump approximation and true blur have been normalized for ease of viewing. We see in both cases that the psf replicates manifest themselves at the jump locations and are scaled by the jump values.

$$f_1(x) = \begin{cases} \frac{3}{2} & -\frac{3\pi}{4} \leq x < -\frac{\pi}{2} \\ \frac{7}{4} - \frac{x}{2} + \sin(x - \frac{1}{4}) & -\frac{\pi}{4} \leq x < \frac{\pi}{8} \\ \frac{11}{4}x - 5 & \frac{3\pi}{8} \leq x < -\frac{3\pi}{4} \\ 0 & \text{else} \end{cases} \tag{4.4}$$

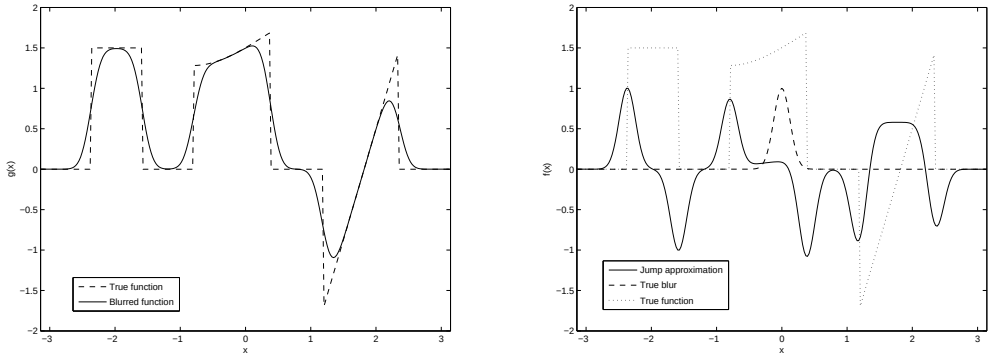

(a) True function and blurred observation (b) After edge detection

Fig. 4.2: Estimation of psfs by applying edge detectors – Gaussian blur, $N = 128$, trigonometric concentration factor

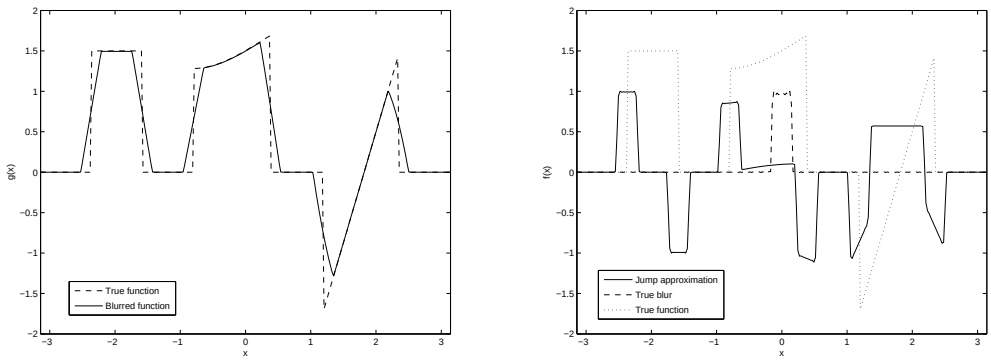

(a) True function and blurred observation (b) After edge detection

Fig. 4.3: Estimation of psfs by applying edge detectors – Out-of-focus blur, $N = 128$, trigonometric concentration factor

4.2 Effect of Noise and the Choice of Concentration Factors

We will assume that the Fourier coefficients $\hat{\mathbf{g}}(k)$ are corrupted by zero mean, additive white complex Gaussian noise of variance ρ^2. As discussed in Section 2.5, the concentration method is linear, and the physical-space noise component $\tilde{\mathbf{n}}$ remains Gaussian with zero mean. However, the noise component acquires a covariance structure due to the use of the concentration factors. Let $\tilde{\mathbf{n}}(x_a)$ denote the noise component at location x_a and $\tilde{\mathbf{n}}(x_b)$ denote the noise component at location x_b. From Lemma 2.5.1, and when using a single concentration factor σ, we have

$$\begin{aligned} C_n(x_a, x_b) &= \mathrm{E}\,[(S_M^\sigma[\tilde{n}](x_a) - \mathrm{E}\,[\,S_M^\sigma[\tilde{n}](x_a)\,])\,(S_M^\sigma[\tilde{n}](x_a) - \mathrm{E}\,[\,S_M^\sigma[\tilde{n}](x_a)\,])^*] \\ &= \rho^2 \sum_{l=-M}^{M} \sigma^2\left(\frac{|l|}{M}\right) e^{il(x_a - x_b)} \end{aligned} \tag{4.5}$$

For optimal results, this covariance structure has to be incorporated in any subsequent PSF parameter estimation method.

Simulation results also reveal that it is best to use low-order edge detectors for psf estimation. Not only do they reduce the impact of high-frequency noise, their jump waveforms $W_0^{\sigma,N}(x)$ are more agreeable with subsequent parameter estimation routines. Substituting (2.20) in (4.2), we have

$$\begin{aligned} S_N^\sigma[g](x) &= (S_N^\sigma[f] * h)(x) + \tilde{\mathbf{n}} \\ &\approx ([f] * W_0^{\sigma,N} * h)(x) + \tilde{\mathbf{n}} \end{aligned} \tag{4.6}$$

Clearly, we require that $(W_0^{\sigma,N} * h)(x)$ be a close approximation to $h(x)$. It has been observed that this is indeed the case for low-order edge detectors, while high-order edge detectors do not satisfy this criterion. Figures 4.4 and 4.5 illustrate this phenomenon. Figure 4.4(a) plots the jump response of the trigonometric concentration factor along with a Gaussian blur. Figure 4.4(b) plots the result of convolving this response with the blur, and is seen to closely approximate the true blur. In contrast, the plots in Figure 4.5 reveal that the presence of strong sidelobes in the jump response of the exponential (high-order) concentration factor result in the convolution output bearing no resemblance to the actual blur.

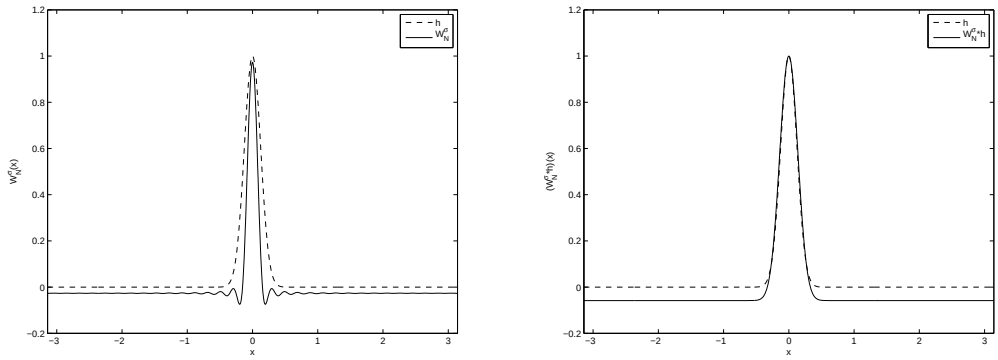

(a) Characteristic response $W_0^{\sigma,N}(x)$ – Trigonometric factor

(b) Plot of $(W_0^{\sigma,N} * h)(x)$

Fig. 4.4: Use of low-order edge detectors in psf estimation, $N = 128$

High-order edge detectors may be used only when iterative deconvolution schemes are used to extract and/or denoise the psf replicates. There is also the option of using the concentration factor design procedure outlined in Section 2.4 to design factors which specifically minimize the error $\left\| W_0^{\sigma,N} * h - h \right\|$ for template blurs.

4.3 Numerical Results

This section provides simulation results of Gaussian and out-of-focus blur estimation.

4.3.1 Gaussian Blur

The estimation procedure can be summarized as follows:

1. Low-pass filter the noisy Fourier coefficients.

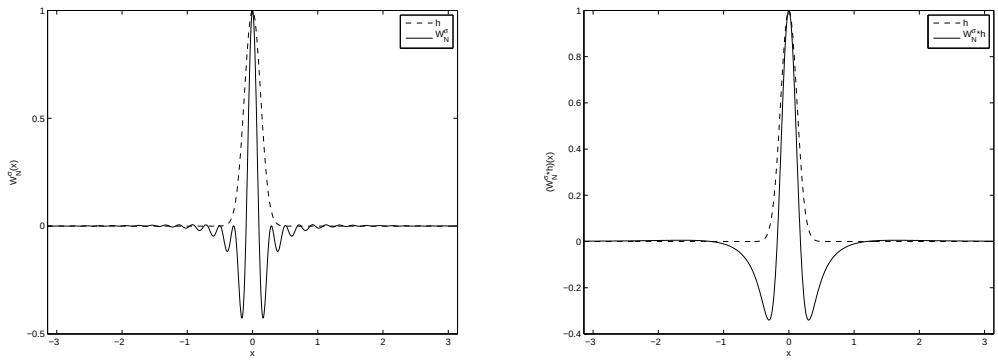

(a) Characteristic response $W_0^{\sigma,N}(x)$ – Exponential factor

(b) Plot of $(W_0^{\sigma,N} * h)(x)$

Fig. 4.5: Use of high-order edge detectors in psf estimation, $N = 128$

2. Apply the concentration edge detector.
3. Identify edge vicinities with psf replicates.
4. Identify psf parameters.

Consider the estimation of the Gaussian psf from the test function $f_1(x)$ in Figure 4.6 (a). This figure plots the true function as well as the blurred, noisy observation. The noise is assumed to be additive white complex Gaussian of variance 0.25 and acting in Fourier space. Since edge detection enhances the noise component in the signal, we first perform low-pass filtering. In this example, we use a Fourier space Gaussian filter. The result of jump approximation on these coefficients is plotted in Figure 4.6(b) [2]. The primary artifacts are spurious responses in smooth regions; this however, is unavoidable when using low-order factors. The next step is to isolate regions where the psf occurs. Several methods may be used, including enhancement of scales or minmod, [10, 12], followed by thresholding. The example below uses enhancement of scales; i.e.,

$$S_N^{\text{enh}}[g](x) = \begin{cases} S_N^{\sigma}[g](x) & |S_N^{\sigma}[g](x)|^p > \gamma \\ 0 & \text{else} \end{cases} \tag{4.7}$$

Here, p is usually of the order $2-4$, while γ is an empirically chosen threshold. The edge regions obtained by this procedure are plotted in Figure 4.7 (a). Note that some spurious regions are identified

[2]The jump response has been normalized for easy viewing.

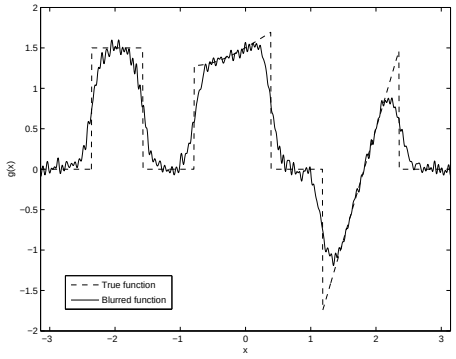

(a) Blurred noisy function

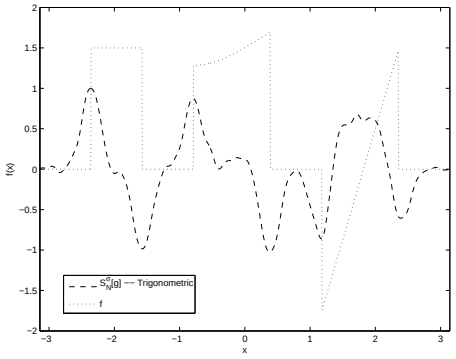

(b) Jump approximation – trigonometric factor

Fig. 4.6: Gaussian psf estimation, $N = 128$

and some regions (closely spaced jumps or small jumps) may be missed; however, the multiplicity of psf replicates allows us to overcome these errors. We now proceed to estimate the variance of

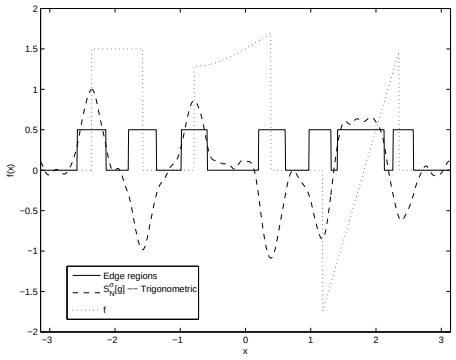

(a) Identifying edge regions

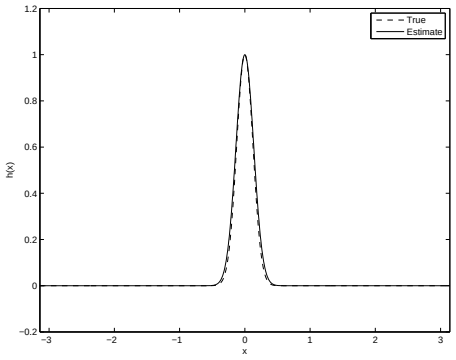

(b) PSF estimate

Fig. 4.7: Gaussian parameter estimation, $N = 128$

the Gaussian in each of these regions. Assuming the blur to be of the form $\exp\left(-\frac{(dx)^2}{2}\right)$, we may linearize the data fit problem as follows

$$\log(|\tilde{S}^{\sigma}_{M}[g](x)|) = -\frac{d^2}{2}x^2 \tag{4.8}$$

Here $\tilde{S}^{\sigma}_{N}[g](x)$ denotes the jump function normalized by its maximum value in each region. Computing the mean value of d leads to a table of variance estimates for each region, as given in Table 4.1. The mean value from the table is used to plot the psf estimate in Figure 4.7 (b). The estimate

can be seen to agree quite well with the true psf. The 2-norm of the error was computed to be 0.44. We note, however, that better parameter estimation schemes can be devised such as a leave-one-out cross validation scheme to reduce the impact of the spurious responses in the jump approximation.

Table 4.1: Variance estimates from different regions (Mean Value is 7.361; Actual value is 8.660)

Region	1	2	3	4	5	6	7
Value	7.5356	7.1962	7.2665	6.9605	8.1978	4.2334	9.1826

4.3.2 Out-of-focus Blur

The challenge with piecewise-smooth blurs is that use of conventional low-pass filtering smears the psf replicates. While this may be tolerable for low noise levels, a more robust procedure would be to utilize edge-preserving filtering schemes such as total-variation (TV) denoising. Consider the estimation of the out-of-focus blur from the blurred and noisy function in Figure 4.8 (a). The concentration jump response computed using the trigonometric factor is plotted in Figure 4.8 (b).

$$f_2(x) = \begin{cases} -1 & -2.5 \leq x < -\frac{\pi}{4} \\ e^{-x} & 0 \leq x < \frac{\pi}{4} \\ 1 + \frac{\cos(5x)}{2} & 1.25 \leq x < 2.75 \\ 0 & \text{else} \end{cases} \tag{4.9}$$

We now compute the solution of the following iterative program

$$\min_{p} \quad \| S_N^{\sigma}[g] - Wp \|_2^2 + \lambda \|p\|_{\text{TV}} \tag{4.10}$$

where W denotes a Toeplitz matrix whose rows contain shifted replicates of the jump response $W_0^{\sigma,N}(x)$. We may also combine the solutions from using different factors using the minmod operator. Such a result is shown in Figure 4.9 (a). This plot is the consequence of using the minmod operator on the TV-denoising solutions of the trigonometric and exponential factors. The resulting psf estimate, computed by taking the mean of the widths of each of the psf replicates is plotted in Figure 4.9 (b).

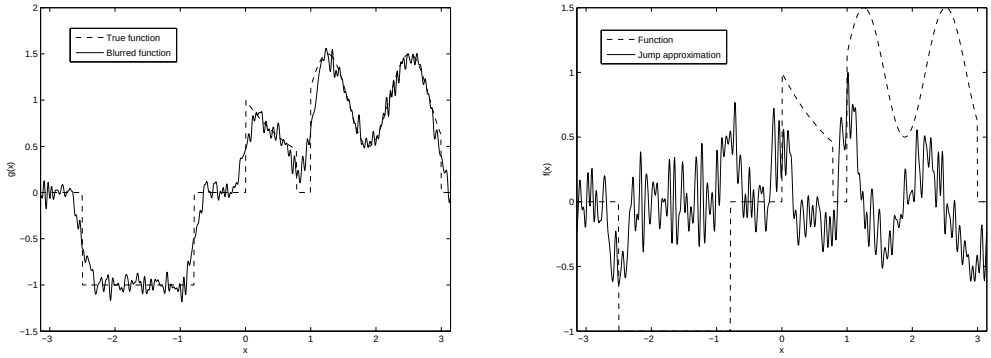

(a) Blurred noisy function (Test function(b) Jump approximation – trigonometric factor $f_2(x)$, (4.9))

Fig. 4.8: Out-of-focus psf estimation, $N = 128$

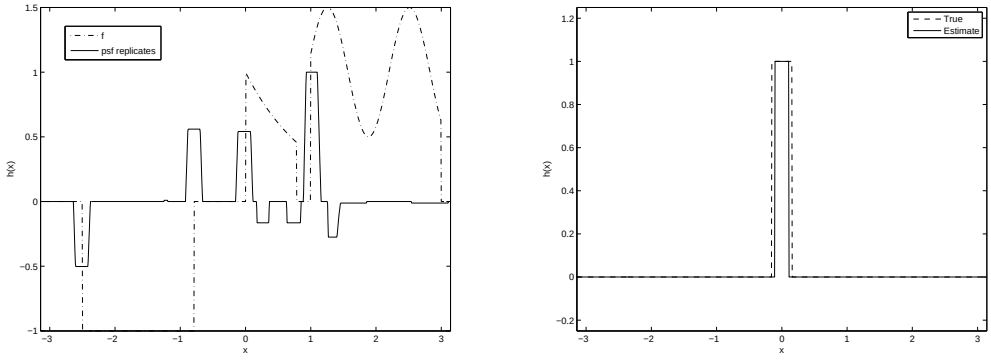

(a) After TV denoising (b) PSF estimate

Fig. 4.9: Out-of-focus parameter estimation, $N = 128$

CHAPTER 5

SUMMARY AND FUTURE DIRECTIONS

In this dissertation, we have introduced theory, algorithms and computational tools for the processing of piecewise-analytic data from Fourier measurements. In particular, the previous chapters have addressed three problems,

- The detection of jump discontinuities from spectral data.
- The reconstruction of piecewise-analytic functions from non-harmonic Fourier measurements.
- The estimation of point-spread functions (psfs) from blurred Fourier data.

The processing of piecewise-analytic functions from Fourier data is challenging and deserves special attention, since local features cannot be well approximated from global measurements. We have exploited the relationship between jump discontinuities and Fourier coefficients to arrive at efficient and accurate jump detection, function reconstruction and psf estimation schemes. Numerical results were primarily presented using one-dimensional test functions and image phantoms, although applications for these results exist in other domains such as the solution of partial differential equations. Some of the numerical simulations were motivated by problems in magnetic resonance imaging, where it is required to reconstruct images from Fourier measurements.

Fundamental to all these results is the accurate extraction of jump information from Fourier measurements. This problem was addressed in Chapter 2, where the concentration edge detection method was used to compute jump information. Although the concentration method is a well developed topic in literature, this dissertation introduced several new ideas and tools for the accurate and localized detection of jumps using this framework. In particular, the notion of a *jump response* was formally defined and used to relate the concentration jump approximation to jumps in the function and its higher-order derivatives. Moreover, a design framework for the computation of concentration or "filter" factors was developed. This framework allows for the design of concentration factors applicable to a wide variety of problem settings, including those involving missing bands of spectral data. Analytical and empirical results were also provided to relate some of the standard concentration factors with particular problem formulations of this framework. Extensions and improvements, with some original contributions were also proposed to an existing method of statistical edge detector design. Finally, use of the concentration method for the detection of jumps from non-harmonic Fourier data was investigated, and a variational formulation proposed for the

accurate approximation of jump information under this problem setting.

Chapter 3 addressed the reconstruction of functions from non-harmonic Fourier measurements. The problems posed by non-harmonic acquisition were identified by studying the properties of the kernel described by these non-harmonic modes. A brief summary of two prevalent reconstruction methods – convolutional gridding and uniform re-sampling – was provided, along with error analysis for gridding reconstructions. While an analysis of computational cost and selection of gridding parameters have previously been addressed in literature, the study of non-uniform sampling density and its effect on reconstruction error is an original contribution of this dissertation. Based on this study, two new schemes were proposed for the mitigation of errors due to non-harmonic acquisition:

- Spectral re-projection methods, where we use knowledge about the location of jump discontinuities to reconstruct in the smooth intervals of the function. Analysis of the reconstruction error for re-projection methods was provided, along with a comparison with results from gridding. This analysis, supported by simulation results revealed improved accuracy in the reconstruction, as well as reduced input data requirements.
- An indirect reconstruction method incorporating edge information, where we use both jump values and locations to synthesize "new" high-frequency coefficients.

Finally, the presence of jumps in a function was exploited to construct a scheme for the estimation of psfs from blurred Fourier data. A discussion of this method, along with numerical results showing the estimation of Gaussian and out-of-focus blurs was presented in Chapter 4.

5.1 Future Directions

Among the topics discussed in this dissertation, some are particularly amenable for future investigation. For example, an extension of the concentration method to the approximation of jumps in derivatives and higher-order derivatives is of great interest. A framework for the design of concentration factors similar to that in Section 2.4, but for the identification of jumps in derivatives, will find great utility. The multi-dimensional edge detection method of Section 2.6 essentially computes edge maps along individual dimensions and fuses them to a composite map. A truly multi-dimensional edge detection scheme for Fourier data will is of great importance in several fields.

While new methods have been proposed for the reconstruction of functions from non-harmonic Fourier data, there are indications that information about edges may be utilized to improve the reconstruction accuracy in traditional reconstruction schemes. For example, new gridding window functions may be defined using local edge information to improve reconstruction accuracy and/or reduce computational cost. Further, there is no reason to limit ourselves to the use of jump information. The use of jump information in the higher-order derivatives of the function are bound to yield greater reconstruction accuracy.

Similar areas of investigation exist in the psf estimation problem. A multidimensional extension of the procedure, especially for the case of non-separable blurs will find great application. More robust parameter estimation schemes, incorporating the statistical characteristics of noise are bound to yield improvements in the quality of the psf estimate.

A prominent theme in the topics discussed in this dissertation is the interplay between local features and global expansions. This is a fascinating topic which holds plenty of promise, with applications spanning several domains. It is conceivable, for example, that methods such as reprojection and those incorporating edge information may be used to significantly improve current image coding and compression schemes. The possibilities are plentiful, and it is hoped that the future holds news of exciting discoveries and developments.

REFERENCES

[1] D. Gottlieb and S. A. Orszag, *Numerical Analysis of Spectral Methods: Theory and Applications*. Society for Industrial and Applied Mathematics, 1977.

[2] A. Gelb and E. Tadmor, "Detection of edges in spectral data," *Appl. Comput. Harmonic Anal.*, vol. 7, pp. 101–135, 1999.

[3] D. M. Cates, "Edge detection using Fourier data with applications," Dept. Math. Stat., Ph.D. dissertation, Arizona State Univ., Tempe, Arizona, 2007.

[4] L. A. Shepp and B. F. Logan, "The Fourier reconstruction of a head section," *IEEE Trans. Nucl. Sci.*, vol. 21, no. 1, pp. 21–43, 1974.

[5] J. D. O'Sullivan, "Fast sinc function gridding algorithm for Fourier inversion in computer tomography," *IEEE Trans. Med. Imag.*, vol. 4, no. 4, 1985.

[6] D. Rosenfeld, "An optimal and efficient new gridding algorithm using singular value decomposition," *Magnetic Resonance Med.*, vol. 40, no. 1, pp. 14–23, 1998.

[7] D. Gottlieb and C. W. Shu, "On the Gibbs phenomenon and its resolution," *SIAM Rev.*, pp. 644–668, 1997.

[8] J. Hesthaven, S. Gottlieb, and D. Gottlieb, *Spectral Methods for Time-Dependent Problems*. Cambridge University Press, 2007.

[9] J. Canny, "A computational approach to edge detection," *IEEE Trans. Pattern Anal. Mach. Intell.*, vol. 8, pp. 679–698, 1986.

[10] A. Gelb and E. Tadmor, "Detection of edges in spectral data II – nonlinear enhancement," *SIAM J. Num. Anal.*, vol. 38, no. 4, pp. 1389–1408, Sep.-Oct. 2000.

[11] S. Engelberg and E. Tadmor, "Recovery of edges from spectral data with noise – a new perspective," *SIAM J. Num. Anal.*, vol. 46, no. 5, pp. 2620–2635, 2008.

[12] A. Gelb and E. Tadmor, "Adaptive edge detectors for piecewise smooth data based on the minmod limiter," *J. Sci. Comp.*, vol. 28, no. 2, pp. 279–306, 2006.

[13] A. Gelb and D. M. Cates, "Detection of edges in spectral data III – refinement of the concentration method," *J. Sci. Comp.*, vol. 36, no. 1, pp. 1–43, 2008.

[14] R. Archibald and A. Gelb, "Reducing the effects of noise in image reconstruction," *J. Sci. Comp.*, vol. 17, no. 1, pp. 167–180, 2002.

[15] A. Viswanathan, D. Cochran, A. Gelb, and D. Cates, "Detection of signal discontinuities from noisy Fourier data," in *Proc. 42nd Asilomar Conf. Sig. Sys. Comp.*, 2008, pp. 1705–1708.

[16] E. J. Candes, J. Romberg, and T. Tao, "Robust uncertainty principles: exact signal reconstruction from highly incomplete frequency information," *IEEE Trans. Inf. Theory*, vol. 52, no. 2, pp. 489–509, 2006.

[17] ——, "Stable signal recovery from incomplete and inaccurate measurements," *Commun. Pure Appl. Math.*, vol. 59, pp. 1207–1223, 2005.

[18] E. Tadmor and J. Zou, "Novel edge detection methods for incomplete and noisy spectral data," *J. Fourier Anal. Appl.*, vol. 14, no. 5, pp. 744–763, 2008.

[19] K. S. Eckhoff, "Accurate and efficient reconstruction of discontinuous functions from truncated series expansions," *Math. Comp.*, vol. 61, no. 204, pp. 745–763, 1993.

[20] S. Boyd and L. Vandenberghe, *Convex Optimization*. Cambridge University Press, 2004.

[21] (2008, Dec.) CVX: Matlab software for disciplined convex programming (web page and software). M. Grant and S. Boyd. [Online]. Available: http://stanford.edu/~boyd/cvx

[22] M. Grant and S. Boyd, "Graph implementations for nonsmooth convex programs," in *Recent Advances in Learning and Control (a tribute to M. Vidyasagar)*, ser. Lecture Notes in Control and Information Sciences, V. Blondel, S. Boyd, and H. Kimura, Eds. Springer, Dec. 2008, pp. 95–110.

[23] S. M. Kay, *Fundamentals of Statistical Signal Processing – Detection Theory*. Prentice Hall Signal Processing Series, 1993.

[24] ——, *Fundamentals of Statistical Signal Processing – Estimation Theory*. Prentice Hall Signal Processing Series, 1993.

[25] R. C. Gonzalez and R. E. Woods, *Digital Image Processing*, 3rd ed. Addison-Wesley Publishing, 1992.

[26] M. Kadec, "The exact value of the Paley-Wiener constant," *Sov. Math., Dokl.*, vol. 5, pp. 559–561, 1964.

[27] J. A. Fessler and B. P. Sutton, "Nonuniform fast Fourier transforms using min-max interpolation," *IEEE Trans. Sig. Proc.*, vol. 51, no. 2, pp. 560–574, 2003.

[28] G. Steidl, "A note on fast Fourier transforms for nonequispaced grids," *Adv. Comp. Math.*, vol. 9, no. 3, pp. 337–352, 1998.

[29] N. Levinson, *Gap and Density Theorems*. American Mathematical Society, 1940.

[30] R. R. M. Young, *An Introduction to Nonharmonic Fourier Analysis*. Academic Press, New York, 2001.

[31] J. Benedetto and P. J. S. G. Ferreira, *Modern Sampling Theory: Mathematics and Applications*. Birkhauser, 2001.

[32] T. Knopp, S. Kunis, and D. Potts, "Fast iterative reconstruction for MRI from nonuniform k-space data," *revised Preprint A-05-10, Universitat zu Lubeck*, 2005.

[33] M. Lustig, "Sparse MRI," Dept. Elect. Eng., Ph.D. dissertation, Stanford Univ., 2008.

[34] J. G. Pipe and P. Menon, "Sampling density compensation in MRI: rationale and an iterative numerical solution," *Magnetic Resonance Med.*, vol. 41, no. 1, pp. 179–186, 1999.

[35] McConnell Brain Imaging Center, "BrainWeb: simulated brain database," http://www.bic.mni.mcgill.ca/brainweb/.

[36] C. A. Cocosco, V. Kollokian, R. K. S. Kwan, and A. C. Evans, "Brainweb: Online interface to a 3D MRI simulated brain database," *NeuroImage*, vol. 5, no. 4, p. 425, 1997.

[37] R. K. S. Kwan, A. C. Evans, and G. B. Pike, "MRI simulation-based evaluation of image-processing andclassification methods," *IEEE Trans. Med. Imag.*, vol. 18, no. 11, pp. 1085–1097, 1999.

[38] K. S. K. Remi, A. C. Evans, and G. B. Pike, "An extensible MRI simulator for post-processing evaluation," in *Proc. 4th Int. Conf. Visualization Biomed. Comp.* Springer, 1996, pp. 135–140.

[39] D. L. Collins, A. P. Zijdenbos, V. Kollokian, J. G. Sled, N. J. Kabani, C. J. Holmes, and A. C. Evans, "Design and construction of a realistic digital brain phantom," *IEEE Trans. Med. Imag.*, vol. 17, no. 3, pp. 463–468, 1998.

[40] K. E. Atkinson, *An Introduction to Numerical Analysis*. John Wiley & Sons, 1978.

[41] D. Rosenfeld, "New approach to gridding using regularization and estimation theory," *Magnetic Resonance Med.*, vol. 48, no. 1, pp. 193–202, 2002.

[42] P. C. Hansen, *Rank-deficient and Discrete Ill-posed Problems: Numerical Aspects of Linear Inversion*. Society for Industrial and Applied Mathematics, 1998.

[43] R. Archibald and A. Gelb, "A method to reduce the Gibbs ringing artifact in MRI scans while keeping tissue boundary integrity," *IEEE Trans. Med. Imag.*, vol. 21, pp. 305–319, 2002.

[44] H. Bateman and A. Erdelyi, *Higher Transcendental Functions*. McGraw-Hill, New York, 1953.